PREFACE TO THE EDITION

It is with great pleasure that we present the latest issue of the **International Journal of Technical Research Studies (IJTRS)**, a collection that reflects the rapid technological advancements shaping today's engineering and computational landscape. The articles in this issue highlight cutting-edge research across multiple domains, capturing both theoretical innovations and practical applications that address real-world challenges.

This edition brings together significant contributions ranging from AI-augmented software testing frameworks that revolutionize large-scale system validation, to advanced navigation strategies for autonomous multi-agent environments. The issue also explores the transformative role of fog computing in creating resilient smart transportation systems, offering crucial insights into latency reduction, system reliability, and scalable urban mobility solutions.

Further contributions examine the future of engineering design through smart surface texturing for enhanced tribological performance, high-efficiency inductive charging systems for electric vehicles, and breakthroughs in neuromorphic hardware architectures that push the boundaries of ultra-low-power computing. Together, these studies demonstrate how emerging technologies continue to reshape engineering practices, sustainability goals, and computational efficiency.

We extend our sincere appreciation to the researchers, reviewers, and editorial team whose dedication has made this issue possible. It is our hope that the scholarship presented here will inspire continued inquiry, collaboration, and technological innovation within the global research community.

Dr. Krishna Prasad K
Chief editor

CONTENTS

INTERNATIONAL JOURNAL OF TECHNICAL RESEARCH STUDIES (IJTRS)
(Open Access, Double-Blind Peer Reviewed Journal)
ISSN Online: ISSN Print
EDUSCHOOL ACADEMIC RESEARCH & PUBLISHERS

AI-Augmented Software Testing for Large-Scale Systems: A Comprehensive Framework and Empirical Analysis

Mini T V

Associate Professor, Department of Computer Science, Sacred Heart College (Autonomous), Chalakudy, Kerala, India

Article information

Received: 4th September 2025
Received in revised form: 6th October 2025
Accepted: 8th November 2025
Available online: 9th December 2025

Volume:1
Issue:1
DOI:https://doi.org/10.5281/zenodo.17875809

Abstract

The exponential growth in software system complexity necessitates innovative testing methodologies that transcend traditional approaches. This paper presents a comprehensive framework for AI-augmented software testing specifically designed for large-scale distributed systems. We introduce a hybrid architecture integrating deep learning models, reinforcement learning agents, and evolutionary algorithms to automate test case generation, execution, and defect prediction. Our empirical evaluation across 15 enterprise-level applications demonstrates a 34.7% improvement in defect detection rates, 42.3% reduction in testing time, and 28.9% increase in code coverage compared to conventional testing frameworks. The proposed system employs transformer-based models for test oracle generation and graph neural networks for dependency analysis. We validate our approach through controlled experiments involving 2.3 million test cases across systems ranging from 500K to 5M lines of code. Results indicate significant improvements in regression testing efficiency, with the AI system identifying 87.6% of critical bugs within the first 20% of test execution time. This research contributes both theoretical foundations and practical implementation strategies for next-generation software quality assurance.

Keywords:- Software Testing, Artificial Intelligence, Machine Learning, Deep Learning, Test Automation, Quality Assurance, Large-Scale Systems, Defect Prediction, Test Case Generation, Continuous Integration

I. INTRODUCTION

The contemporary software engineering landscape is characterized by unprecedented complexity in system architectures, with large-scale applications often comprising millions of lines of code distributed across heterogeneous platforms and technologies. Traditional software testing methodologies, while foundational to quality assurance, increasingly struggle to maintain efficacy when confronted with the scale, dynamism, and intricacy of modern systems [1], [2]. The limitations of conventional approaches manifest in several critical dimensions: inadequate coverage of complex interaction patterns, inability to adapt to rapidly evolving codebases, and prohibitive resource requirements for comprehensive testing campaigns.

Recent advances in artificial intelligence and machine learning present transformative opportunities for software testing paradigms. Deep learning architectures have demonstrated remarkable capabilities in pattern recognition, anomaly detection, and predictive modeling capabilities directly applicable to software quality assurance challenges [3], [4], [5]. Furthermore, reinforcement learning frameworks offer promising avenues for intelligent test case prioritization and resource allocation, while natural language processing techniques enable sophisticated analysis of specification documents and bug reports [6].

Despite these technological advances, the integration of AI techniques into production-grade testing frameworks remains nascent. Existing research predominantly focuses on isolated aspects of the testing lifecycle, lacking comprehensive frameworks that address the full spectrum of testing activities in large-scale systems. Moreover, empirical validations often occur in controlled academic settings, raising questions about real-world applicability and scalability [7], [8].

This paper addresses these gaps by presenting a holistic AI-augmented testing framework specifically engineered for large-scale software systems. Our contributions encompass:

- A comprehensive architectural framework integrating multiple AI techniques across the testing lifecycle
- Novel algorithms for intelligent test case generation using transformer-based models
- A reinforcement learning approach for dynamic test prioritization
- Empirical validation across 15 enterprise applications
- Detailed analysis of performance characteristics, scalability factors, and deployment considerations.

The remainder of this paper is organized as follows: Section II surveys related work in AI-based testing; Section III details our system architecture; Section IV describes the methodological approach; Section V presents experimental results; Section VI discusses implications and limitations; and Section VII concludes with future research directions.

II. RELATED WORK

A. Traditional Software Testing Approaches

Software testing has evolved through several generations of methodologies, from manual testing practices to automated unit testing frameworks and sophisticated continuous integration pipelines [9]. Classical approaches including equivalence partitioning, boundary value analysis, and control flow testing have formed the theoretical foundation of the discipline [10]. However, these techniques exhibit limited scalability when applied to complex distributed systems with millions of potential execution paths.

Model-based testing represents a significant advancement, utilizing formal specifications to generate test cases systematically [11]. Tools such as Spec Explorer and Conformiq have demonstrated practical utility in specific domains. Nevertheless, the cognitive overhead of creating and maintaining formal models constrains widespread adoption, particularly for rapidly evolving systems [12].

B. Machine Learning in Software Testing

The application of machine learning to software testing has garnered substantial research attention over the past decade. Early work by Briand et al. [13] demonstrated the viability of using classification algorithms for defect prediction based on code metrics. Subsequent research expanded these techniques to include more sophisticated models incorporating historical bug data, version control information, and developer activities [14], [15].

Deep learning approaches have recently emerged as particularly promising [24], [25]. White et al. [16] applied recurrent neural networks to learn code patterns associated with bugs, achieving significant improvements over traditional static analysis. Pradel and Sen [17] introduced DeepBugs, utilizing neural networks to detect semantic errors in JavaScript code. Transformer architectures [26] have shown exceptional performance in sequence-to-sequence tasks. Recent work on testing deep learning systems [27] has highlighted the need for specialized approaches. However, existing efforts primarily target specific bug categories rather than comprehensive testing frameworks [28].

Reinforcement learning has been explored for test case prioritization and selection [29]. Chen et al. [18] proposed an RL-based approach that learns optimal prioritization strategies from historical test execution data. Deep reinforcement learning techniques [30] offer promising avenues for learning complex testing policies. While promising, their evaluation was limited to relatively small systems (fewer than 100K lines of code), leaving scalability questions unresolved.

C. Search-Based Software Testing

Search-based software engineering (SBSE) formulates testing problems as optimization tasks solvable through metaheuristic algorithms [19]. Genetic algorithms, particle swarm optimization, and simulated annealing have been successfully applied to test data generation, test suite minimization, and regression testing [20], [21]. McMinn [22] provides a comprehensive survey demonstrating SBSE's effectiveness across various testing activities.

Despite these successes, SBSE approaches face challenges in defining appropriate fitness functions for complex systems and often require extensive parameter tuning [23]. Integration of SBSE with machine learning represents a promising direction insufficiently explored in existing literature.

III. SYSTEM ARCHITECTURE

Our AI-augmented testing framework adopts a modular architecture comprising five principal components: the Test Data Repository, ML Model Layer, Test Generation Engine, Execution Manager, and Continuous Learning Module. The architecture integrates traditional testing infrastructure with advanced AI capabilities to enable comprehensive automated testing.

A. Test Data Repository

The Test Data Repository serves as the central knowledge base, maintaining comprehensive records of historical test executions, identified defects, code coverage metrics, and system specifications. The repository implements a graph database schema (Neo4j) to capture complex relationships between code entities, test cases, and failure patterns. This graph representation facilitates efficient queries for dependency analysis and impact assessment. Data versioning mechanisms ensure temporal consistency, enabling the system to track evolution of testing artifacts across software releases.

B. Machine Learning Model Layer

The ML Model Layer incorporates multiple specialized models addressing distinct testing challenges. A transformer-based sequence-to-sequence model (T-TestGen) generates test cases from natural language specifications, trained on a corpus of 500,000 specification-test pairs. The architecture employs 12 encoder and decoder layers with 8 attention heads, achieving BLEU scores of 0.847 on held-out test data.

For defect prediction, we employ a hybrid ensemble combining gradient boosting machines (XGBoost) and deep neural networks. Input features encompass static code metrics (cyclomatic complexity, coupling measures), historical defect densities, and developer activity patterns. The ensemble achieves AUC-ROC of 0.923 on our evaluation dataset.

A graph neural network (GNN) analyzes code dependency graphs to identify high-risk components requiring intensive testing. The GNN implements graph attention networks [31], [32] with 4 layers, processing call graphs with up to 100,000 nodes. This component demonstrates particular efficacy in predicting integration failures.

C. Test Generation Engine

The Test Generation Engine synthesizes inputs from multiple sources to produce comprehensive test suites. It operates in three modes: specification-driven generation utilizing T-TestGen, mutation-based generation applying learned mutation operators, and feedback-directed generation guided by coverage analysis. The engine implements intelligent deduplication algorithms to eliminate redundant test cases while preserving diversity. A reinforcement learning agent orchestrates the generation process, learning optimal strategies for allocating resources across different generation modes.

D. Execution Manager and Results Analysis

The Execution Manager coordinates distributed test execution across containerized environments, implementing dynamic load balancing and fault tolerance. It prioritizes test cases using a multi-objective optimization approach considering predicted fault-detection capability, execution time, and dependency constraints. Results analysis employs machine learning models to classify failures, identify failure patterns, and recommend debugging strategies. An attention-based neural network processes execution traces to pinpoint failure causes, reducing manual inspection overhead by 67% in our experiments. Prior research on automated debugging [35] and refactoring engine testing [36] provides foundations for our approach.

E. Continuous Learning Module

The Continuous Learning Module implements online learning mechanisms enabling the framework to adapt dynamically to evolving software characteristics. The module monitors test execution outcomes, code changes, and defect discoveries to identify concept drift and trigger model updates when performance degrades below defined thresholds. Transfer learning strategies [37] enable knowledge sharing across different software systems within an organization. Active learning components [38] identify high-value test cases requiring human annotation, optimizing the feedback loop between AI systems and domain experts.

IV. METHODOLOGY

Our evaluation methodology employs a multi-faceted approach combining controlled experiments, industrial case studies, and comparative analysis against baseline testing frameworks. This section details the experimental design, subject systems, metrics, and procedures.

A. Subject Systems and Data Collection

We selected 15 open-source and proprietary enterprise applications representing diverse domains: e-commerce platforms, financial systems, healthcare applications, and telecommunications infrastructure. System sizes range from 523,000 to 4.8 million lines of code (primarily Java, Python, and C++). For each system, we collected historical data spanning 18-36 months, including version control logs, issue tracking records, continuous integration results, and existing test suites. This yielded approximately 2.3 million test cases and 47,000 documented bugs for training and validation.

Table 1. Characteristics of Subject Systems

System	Domain	LOC	Language	Test Cases
E-Shop	E-commerce	523K	Java	12,347
FinCore	Banking	1.2M	Java/C++	45,892
MedRec	Healthcare	847K	Python	18,653
TelNet	Telecom	2.1M	C++	67,234
CloudFS	Storage	1.5M	Go	34,128
DataPipe	Analytics	923K	Python	21,456
PayGate	Finance	1.8M	Java	52,341
LogStream	Monitoring	654K	Python	15,892

B. Evaluation Metrics

- We employ a comprehensive set of metrics to assess framework effectiveness. Primary metrics include
- Defect Detection Rate (DDR)—percentage of seeded and real bugs discovered
- Code Coverage—statement, branch, and path coverage percentages
- Testing Time—wall-clock time required for complete test suite execution
- Test Suite Size—number of test cases generated
- False Positive Rate (FPR)—percentage of incorrect failure predictions

Secondary metrics capture efficiency dimensions: test case generation time, model training overhead, and resource utilization (CPU, memory, storage). We also measure APFD (Average Percentage of Faults Detected) to evaluate test prioritization effectiveness.

C. Baseline Comparisons

We compare our framework against three baseline approaches:

- Traditional Testing—existing manual and automated test suites without AI augmentation
- Random Testing—randomly generated test inputs matching our test budget
- SBSE Baseline—genetic algorithm-based test generation using EvoSuite [24]

Each baseline receives identical time and computational budgets to ensure fair comparison. Statistical significance is assessed using Wilcoxon signed-rank tests with Bonferroni correction for multiple comparisons ($\alpha = 0.05$). Effect sizes are reported using Cliff's delta for non-parametric distributions.

V. EXPERIMENTAL RESULTS

This section presents comprehensive experimental results demonstrating the effectiveness of our AI-augmented testing framework. We analyze performance across multiple dimensions and provide detailed comparisons with baseline approaches.

A. Overall Performance Comparison

The AI-augmented approach demonstrates substantial improvements in all measured categories: test coverage increased from 68% to 89% (30.9% improvement), defect detection improved from 72% to 92% (27.8% improvement), time efficiency gained 31.9%, and cost reduction achieved 30.0%. These improvements proved statistically significant across all subject systems ($p < 0.001$, Cliff's $\delta > 0.7$), indicating large effect sizes. Notably, improvements remained consistent across different system sizes and domains, suggesting robust generalization capabilities.

Table 2. Comprehensive Performance Comparison

Metric	Traditional	SBSE	AI-Augmented	Improvement
Stmt Coverage (%)	68.2	73.4	89.5	+31.2%
Branch Coverage (%)	61.5	68.9	88.2	+43.4%
Path Coverage (%)	42.1	51.3	76.3	+81.2%
Mutation Score (%)	62.3	71.4	87.6	+40.6%
APFD Score	0.623	0.712	0.847	+36.0%
Test Gen Time (h)	8.7	6.2	5.1	-41.4%
Exec Time (h)	34.7	28.3	20.1	-42.1%
False Positive (%)	14.2	11.7	8.3	-41.5%

B. Defect Detection Effectiveness

We conducted controlled experiments using mutation testing to evaluate defect detection capabilities. For each subject system, we injected 500-2000 synthetic faults using PITest and Major mutation frameworks, covering common bug patterns. Our framework achieved an average mutation score of 87.6%, significantly exceeding traditional approaches (62.3%) and the SBSE baseline (71.4%). Analysis of detection timing revealed that 78.3% of faults were identified within the first 20% of test execution time, enabling rapid feedback to developers.

Real-world validation using historical bug repositories showed that the AI-augmented framework would have detected 412 out of 473 critical bugs (87.1%) before production deployment, compared to 298 (63.0%) for the original test suites. This translates to prevention of approximately 114 additional production incidents.

C. Coverage Analysis

Coverage analysis reveals differential improvements across coverage types. Statement coverage increased by 21.3% (68.2% → 89.5%), branch coverage by 26.7% (61.5% → 88.2%), and path coverage by 34.2% (42.1% → 76.3%). The disproportionate path coverage improvement stems from the framework's ability to synthesize test sequences exploring deep execution paths. Analyzing coverage growth rates, we observe that AI-augmented testing achieves 80% of maximum coverage within 12.3 hours on average, compared to 34.7 hours for traditional approaches.

D. Machine Learning Model Performance

Individual ML model components exhibited strong performance. The transformer-based test generator (T-TestGen) achieved BLEU scores of 0.847, ROUGE-L of 0.823, and METEOR of 0.791 on specification-to-test translation tasks. Human evaluation by professional testers rated generated tests as 'acceptable or better' in 83.2% of cases. The defect prediction ensemble demonstrated AUC-ROC of 0.923, precision of 0.867, and recall of 0.891 at the optimal threshold. False positive rates remained acceptably low at 8.3%, crucial for maintaining developer trust.

E. Scalability and Performance Overhead

Scalability experiments examined framework performance across systems of varying sizes. Test generation time scaled approximately linearly with codebase size (O(n log n)), while test execution overhead remained constant at approximately 3-5% compared to baseline test runners. Model training constituted the primary computational cost, requiring 8-72 GPU hours depending on system size and model complexity. However, this one-time cost amortizes across thousands of test executions.

VI. DISCUSSION

A. Implications for Practice

Our results demonstrate that AI-augmented testing delivers substantial practical benefits for large-scale software systems. The 34.7% improvement in defect detection translates to significant cost savings through prevented production incidents and reduced debugging time. Organizations implementing similar frameworks should anticipate 6-12 month deployment timelines and initial training data collection periods. The modular architecture facilitates incremental adoption, allowing organizations to integrate individual components before committing to comprehensive deployment.

B. Theoretical Contributions

This research advances theoretical understanding of AI applications in software engineering through several contributions. First, we demonstrate that transformer architectures, previously successful in natural language tasks, transfer effectively to specification-to-test translation when trained on sufficient domain-specific data. Second, our hybrid ensemble approach for defect prediction establishes that combining complementary ML paradigms yields superior performance to individual models.

C. Limitations and Threats to Validity

Several limitations warrant acknowledgment. First, our evaluation focused on specific programming languages and system types; generalization to embedded systems, real-time applications, or dramatically different languages requires further validation. Second, while we evaluated 15 diverse systems, industrial validation across broader organizational contexts would strengthen external validity claims. Model training data requirements present practical constraints, potentially limiting applicability to novel projects with limited historical data.

D. Integration with DevOps Pipelines

Successful deployment requires seamless integration with existing DevOps infrastructure. Our framework provides REST APIs and plugin architectures for popular CI/CD platforms including Jenkins, GitLab CI, CircleCI, and GitHub Actions. Real-time integration enables immediate feedback during development. Developers receive AI-generated test recommendations directly in their IDEs through Language Server Protocol implementations [33]. Test case prioritization research [34] has established foundations for efficient test execution strategies.

VII. CONCLUSION AND FUTURE WORK

This paper presented a comprehensive AI-augmented testing framework specifically engineered for large-scale software systems. Through rigorous empirical evaluation across 15 diverse applications, we demonstrated substantial improvements over traditional testing approaches: 34.7% enhancement in defect detection rates, 42.3% reduction in testing time, and 28.9% increase in code coverage. These results establish the practical viability of integrating advanced AI techniques into production testing pipelines.

The framework's modular architecture, incorporating transformer-based test generation, ensemble defect prediction, graph neural network dependency analysis, and reinforcement learning test prioritization, provides a template for future research and industrial implementation. Future research directions include: extending the framework to support additional programming languages and paradigms; investigating few-shot learning approaches to reduce training data requirements; developing explainable AI techniques to enhance interpretability of model decisions; exploring multi-agent reinforcement learning for distributed testing coordination; and integrating program synthesis techniques for automatic bug repair.

The convergence of artificial intelligence and software engineering presents transformative opportunities for addressing the quality assurance challenges of increasingly complex software systems. This research contributes both theoretical foundations and practical tools toward realizing this vision, while highlighting important areas requiring continued investigation.

REFERENCES

[1] S. Anand *et al*., “An orchestrated survey of methodologies for automated software test case generation,” *Journal of Systems and Software*, vol. 86, no. 8, pp. 1978–2001, Aug. 2013.

[2] M. Harman and B. F. Jones, “Search-based software engineering,” *Information and Software Technology*, vol. 43, no. 14, pp. 833–839, Dec. 2001.

[3] C. S. Păsăreanu and N. Rungta, “Symbolic PathFinder: symbolic execution of Java bytecode,” in *Proc. IEEE/ACM Int. Conf. Automated Software Eng.*, Antwerp, Belgium, 2010, pp. 179–180.

[4] T. Y. Chen, F.-C. Kuo, R. G. Merkel, and T. H. Tse, “Adaptive random testing: The ART of test case diversity,” *Journal of Systems and Software*, vol. 83, no. 1, pp. 60–66, Jan. 2010.

[5] D. Amodei *et al*., “Deep speech 2: End-to-end speech recognition in English and Mandarin,” in *Proc. Int. Conf. Machine Learning*, New York, NY, USA, 2016, pp. 173–182.

[6] A. Arcuri and G. Fraser, “On parameter tuning in search based software engineering,” in *Proc. Int. Symp. Search Based Software Eng.*, Szeged, Hungary, 2011, pp. 33–47.

[7] L. C. Briand, Y. Labiche, and M. Shousha, “Using genetic algorithms for early schedulability analysis and stress testing in real-time systems,” *Genetic Programming and Evolvable Machines*, vol. 7, no. 2, pp. 145–170, Jun. 2006.

[8] G. J. Myers, C. Sandler, and T. Badgett, *The Art of Software Testing*, 3rd ed. Hoboken, NJ, USA: Wiley, 2011.

[9] P. Ammann and J. Offutt, *Introduction to Software Testing*, 2nd ed. Cambridge, UK: Cambridge Univ. Press, 2016.

[10] M. Utting and B. Legeard, *Practical Model-Based Testing: A Tools Approach*. San Francisco, CA, USA: Morgan Kaufmann, 2007.

[11] W. Grieskamp, “Multi-paradigmatic model-based testing,” in *Proc. Int. Workshop Formal Approaches to Software Testing*, Edinburgh, UK, 2006, pp. 1–19.

[12] L. C. Briand, W. L. Melo, and J. Wüst, “Assessing the applicability of fault-proneness models across object-oriented software projects,” *IEEE Trans. Software Eng.*, vol. 28, no. 7, pp. 706–720, Jul. 2002.

[13] T. Zimmermann, R. Premraj, and A. Zeller, “Predicting defects for Eclipse,” in *Proc. Int. Workshop Predictor Models in Software Eng.*, Minneapolis, MN, USA, 2007, pp. 9–15.

[14] S. Kim, T. Zimmermann, E. J. Whitehead Jr., and A. Zeller, “Predicting faults from cached history,” in *Proc. IEEE/ACM Int. Conf. Software Eng.*, Leipzig, Germany, 2008, pp. 489–498.

[15] M. White, M. Tufano, C. Vendome, and D. Poshyvanyk, “Deep learning code fragments for code clone detection,” in *Proc. IEEE/ACM Int. Conf. Automated Software Eng.*, Singapore, 2016, pp. 87–98.
[16] M. Pradel and K. Sen, “DeepBugs: A learning approach to name-based bug detection,” *Proc. ACM Program. Lang.*, vol. 2, no. OOPSLA, pp. 147:1–147:25, Oct. 2018.
[17] J. Chen, Y. Zhu, and H. Zhang, “Reinforcement learning for test case prioritization,” *IEEE Trans. Software Eng.*, vol. 48, no. 4, pp. 1129–1145, Apr. 2022.
[18] M. Harman, S. A. Mansouri, and Y. Zhang, “Search-based software engineering: Trends, techniques and applications,” *ACM Computing Surveys*, vol. 45, no. 1, pp. 11:1–11:61, Dec. 2012.
[19] G. Fraser and A. Arcuri, “EvoSuite: Automatic test suite generation for object-oriented software,” in *Proc. ACM SIGSOFT Symp. Foundations of Software Eng.*, Szeged, Hungary, 2011, pp. 416–419.
[20] S. Yoo and M. Harman, “Regression testing minimization, selection and prioritization: A survey,” *Software Testing, Verification and Reliability*, vol. 22, no. 2, pp. 67–120, Mar. 2012.
[21] P. McMinn, “Search-based software test data generation: A survey,” *Software Testing, Verification and Reliability*, vol. 14, no. 2, pp. 105–156, Jun. 2004.
[22] A. Arcuri and L. Briand, “A practical guide for using statistical tests to assess randomized algorithms in software engineering,” in *Proc. IEEE/ACM Int. Conf. Software Eng.*, San Francisco, CA, USA, 2011, pp. 1–10.
[23] G. Fraser and A. Arcuri, “Whole test suite generation,” *IEEE Trans. Software Eng.*, vol. 39, no. 2, pp. 276–291, Feb. 2013.
[24] Y. LeCun, Y. Bengio, and G. Hinton, “Deep learning,” *Nature*, vol. 521, no. 7553, pp. 436–444, May 2015.
[25] I. Goodfellow, Y. Bengio, and A. Courville, *Deep Learning*. Cambridge, MA, USA: MIT Press, 2016.
[26] A. Vaswani *et al*., “Attention is all you need,” in *Proc. Advances in Neural Information Processing Systems*, Long Beach, CA, USA, 2017, pp. 5998–6008.
[27] K. Pei, Y. Cao, J. Yang, and S. Jana, “DeepXplore: Automated whitebox testing of deep learning systems,” in *Proc. ACM Symp. Operating Systems Principles*, Shanghai, China, 2017, pp. 1–18.
[28] J. M. Zhang, M. Harman, L. Ma, and Y. Liu, “Machine learning testing: Survey, landscapes and horizons,” *IEEE Trans. Software Eng.*, vol. 48, no. 1, pp. 1–36, Jan. 2022.
[29] R. S. Sutton and A. G. Barto, *Reinforcement Learning: An Introduction*, 2nd ed. Cambridge, MA, USA: MIT Press, 2018.
[30] V. Mnih *et al*., “Human-level control through deep reinforcement learning,” *Nature*, vol. 518, no. 7540, pp. 529–533, Feb. 2015.
[31] T. N. Kipf and M. Welling, “Semi-supervised classification with graph convolutional networks,” in *Proc. Int. Conf. Learning Representations*, Toulon, France, 2017, pp. 1–14.
[32] P. Veličković *et al*., “Graph attention networks,” in *Proc. Int. Conf. Learning Representations*, Vancouver, Canada, 2018, pp. 1–12.
[33] M. Beller, G. Gousios, A. Panichella, and A. Zaidman, “When, how, and why developers (do not) test in their IDEs,” in *Proc. ACM SIGSOFT Int. Symp. Foundations of Software Eng.*, Seattle, WA, USA, 2015, pp. 179–190.
[34] S. Elbaum, A. Malishevsky, and G. Rothermel, “Test case prioritization: A family of empirical studies,” *IEEE Trans. Software Eng.*, vol. 28, no. 2, pp. 159–182, Feb. 2002.
[35] C. Parnin and A. Orso, “Are automated debugging techniques actually helping programmers?” in *Proc. ACM Int. Symp. Software Testing and Analysis*, Toronto, Canada, 2011, pp. 199–209.
[36] B. Daniel, D. Dig, K. Garcia, and D. Marinov, “Automated testing of refactoring engines,” in *Proc. ACM SIGSOFT Int. Symp. Foundations of Software Eng.*, Portland, OR, USA, 2007, pp. 185–194.
[37] S. Pan and Q. Yang, “A survey on transfer learning,” *IEEE Trans. Knowledge and Data Eng.*, vol. 22, no. 10, pp. 1345–1359, Oct. 2010.
[38] B. Settles, “Active learning literature survey,” *Computer Sciences Technical Report* 1648, University of Wisconsin–Madison, 2009.

EDUSCHOOL
ACADEMIC RESEARCH & PUBLISHERS

INTERNATIONAL JOURNAL OF
TECHNICAL RESEARCH STUDIES (IJTRS)
(Open Access, Double-Blind Peer Reviewed Journal)

ISSN Online: ISSN Print

Autonomous Multi-Agent Navigation in Crowded Environments: A Comprehensive Survey and Analysis

Ginne M James

Assistant Professor, Department of Computer Science with Data Analytics, Sri Ramakrishna College of Arts & Science, Coimbatore, Tamil Nadu, India

Article information

Received:5th September 2025
Received in revised form:8th October 2025
Accepted:12th November 2025
Available online:9th December 2025

Volume:1
Issue:1
DOI: https://doi.org/10.5281/zenodo.17877282

Abstract

This paper presents a comprehensive survey and analysis of autonomous multi-agent navigation in crowded environments, addressing the fundamental challenge of coordinating multiple mobile agents to achieve collision-free, efficient, and socially-compliant motion in dynamic spaces shared with humans. We examine the theoretical foundations spanning collision avoidance algorithms, social force models, and machine learning approaches. Through systematic analysis of velocity obstacles, reciprocal velocity obstacles, optimal reciprocal collision avoidance, and deep reinforcement learning methods, we identify key advantages and limitations of current approaches. The paper critically evaluates computational complexity, scalability constraints, safety guarantees, and real-world deployment challenges. We present comparative performance metrics across simulation and physical implementations, demonstrating that hybrid approaches combining classical geometric methods with learned policies achieve superior performance in dense crowds. Our analysis reveals that while reinforcement learning methods show promise for social compliance, they face challenges in safety certification and sim-to-real transfer. We conclude with recommendations for future research directions, emphasizing the need for unified frameworks that integrate predictive modeling, multi-modal learning, and formal verification methods to enable robust deployment in safety-critical applications.

Keywords:- Multi-Agent Systems, Crowd Navigation, Collision Avoidance, Reinforcement Learning, Social Robotics, Motion Planning

I. INTRODUCTION

The proliferation of autonomous mobile robots in human-populated environments has created an urgent need for navigation algorithms that ensure safe, efficient, and socially-aware motion in crowded spaces. From service robots in hospitals and shopping malls to autonomous vehicles navigating pedestrian zones, the challenge of multi-agent navigation in dynamic environments represents a critical bottleneck in the deployment of autonomous systems. This problem is fundamentally complex: agents must simultaneously avoid collisions with both static obstacles and dynamic agents (including humans), optimize their trajectories for efficiency, and exhibit behavior that humans perceive as natural and predictable [1].

Traditional motion planning approaches, such as A* and Rapidly-exploring Random Trees (RRT), excel in static environments but struggle with the temporal and uncertainty dimensions introduced by moving agents [2]. The multi-agent navigation problem differs fundamentally from single-agent path planning in several respects:

- The environment state is non-stationary due to the motion of other agents

- Agents must reason about the intentions and future trajectories of others
- Coordination mechanisms are required to resolve conflicts
- Computational constraints demand real-time performance despite the exponential growth in state space complexity with the number of agents [3]

The past two decades have witnessed substantial progress in developing navigation algorithms specifically designed for multi-agent scenarios. Velocity Obstacle (VO) methods and their extensions including Reciprocal Velocity Obstacles (RVO) and Optimal Reciprocal Collision Avoidance (ORCA) provide geometric frameworks for computing collision-free velocities in polynomial time [4], [5]. Social force models, inspired by physics, model pedestrian dynamics through attractive and repulsive forces, enabling the emergence of collective behaviors such as lane formation [6]. More recently, deep reinforcement learning (DRL) has emerged as a promising paradigm, enabling agents to learn navigation policies from experience that can capture complex social conventions and implicit coordination strategies [7], [8].

Despite these advances, significant challenges remain. Classical geometric methods, while computationally efficient and providing formal safety guarantees, often produce robotic behaviors that lack social awareness. Conversely, learning-based approaches can achieve more natural motion but face difficulties in safety certification, interpretability, and generalization beyond training conditions [9]. The sim-to-real gap where policies trained in simulation fail when deployed on physical robots remains a persistent obstacle [10]. Furthermore, most existing work evaluates algorithms in relatively sparse environments, while real-world crowded scenarios involve densities where local minima, deadlock situations, and oscillatory behaviors become prevalent [11].

This paper provides a comprehensive survey and critical analysis of autonomous multi-agent navigation in crowded environments. Our contributions are threefold: First, we present a unified taxonomy of navigation approaches, organizing methods according to their fundamental computational paradigm and highlighting the theoretical assumptions underlying each approach. Second, we provide comparative analysis of performance characteristics including computational complexity, scalability, safety properties, and social compliance across representative algorithms from each major category. Third, we identify open challenges and propose research directions that bridge the gap between theoretical guarantees and practical deployment requirements.

The remainder of this paper is organized as follows: Section II reviews foundational concepts and problem formulations. Section III surveys velocity obstacle methods and geometric approaches. Section IV examines social force models and physics-based techniques. Section V analyzes machine learning and reinforcement learning approaches. Section VI presents comparative evaluation and discusses performance trade-offs. Section VII identifies open challenges and future research directions. Section VIII concludes the paper.

II. PROBLEM FORMULATION AND FUNDAMENTAL CONCEPTS

A. Mathematical Framework

We consider a system of N autonomous agents operating in a two-dimensional or three-dimensional workspace W. Agent i is characterized by its state si(t) = (pi(t), vi(t)) at time t, where pi ∈ W represents position and vi represents velocity. Each agent has a goal position gi ∈ W and seeks to navigate from its initial position pi(0) to gi while avoiding collisions with other agents and static obstacles O ⊂ W [12].

The fundamental objective in multi-agent navigation is to compute control inputs ui(t) for each agent that minimize a cost functional while satisfying safety constraints. Formally, we seek to minimize:

$$J = \sum_{i} \int_{0}^{T} [\, \alpha_e \|p_i(t) - g_i\|^2 + \alpha_v \|v_i(t)\|^2 + \alpha_u \|u_i(t)\|^2 \,]\, dt \qquad (1)$$

subject to collision avoidance constraints ||pi(t) – pj(t)|| ≥ ri + rj for all i ≠ j, where ri represents the radius of agent i. The weights α_e, α_v, and α_u balance goal-reaching behavior, velocity smoothness, and control effort [13].

B. Collision Avoidance Constraints

Collision avoidance in multi-agent systems introduces both spatial and temporal coupling between agents. The configuration space of the system grows exponentially with the number of agents, making exhaustive search intractable for real-time applications. Two primary approaches address this challenge: decentralized methods where each agent independently computes its control based on local information, and centralized methods that jointly optimize all agent trajectories [14].

Decentralized approaches offer computational scalability and robustness to communication failures but may suffer from local optima and oscillatory behaviors. Each agent i observes the states of nearby agents within a sensing radius and computes a locally optimal control. The key challenge is ensuring that independent local decisions lead to globally collision-free motion [15]. Centralized approaches can find globally optimal solutions but face computational intractability for large agent populations and require reliable communication infrastructure [16].

C. Social Compliance Requirements

Beyond geometric collision avoidance, robots operating in human environments must exhibit socially-compliant behavior motion that respects implicit social conventions and is perceived as natural by human observers. Empirical studies reveal that humans navigate using proxemics rules, maintaining context-dependent personal spaces, and engaging in cooperative yielding behaviors [17]. Socially-aware navigation requires agents to:

- Respect Personal Space Boundaries Beyond Physical Collision Distances
- Avoid Sudden Or Unpredictable Maneuvers
- Yield Appropriately In Conflict Situations
- Follow Side-Preference Conventions (E.G., Right-Hand Traffic Rules) [18].

Quantifying social compliance remains challenging. Proposed metrics include minimum passing distance, time-to-collision distributions, path efficiency relative to optimal unobstructed paths, and human comfort ratings from user studies [19]. The tension between efficiency and social compliance creates a fundamental trade-off: strictly minimizing travel time often produces aggressive behaviors that humans find uncomfortable or threatening.

III. VELOCITY OBSTACLE METHODS AND GEOMETRIC APPROACHES

A. Velocity Obstacle Framework

The Velocity Obstacle (VO) concept, introduced by Fiorini and Shiller, provides an elegant geometric characterization of collision states in velocity space [4]. For agent A avoiding agent B, the velocity obstacle VO_A^B represents the set of velocities for A that will lead to collision with B if both agents maintain constant velocity Mathematically,$\mathrm{VO}_A^B = \{ v_A | \exists t > 0 : P_A + t v_A \epsilon B \oplus A\}$ where $\oplus$ denotes Minkowski sum [20].

The VO framework enables real-time collision avoidance by selecting velocities outside the velocity obstacle cone. However, the original VO formulation suffers from oscillatory behaviors in reciprocal scenarios where both agents simultaneously attempt to avoid each other. This limitation motivated the development of Reciprocal Velocity Obstacles (RVO) [5].

B. Reciprocal Velocity Obstacles (RVO)

RVO addresses oscillations by assuming mutual responsibility: each agent takes half the avoidance maneuver required to prevent collision. The reciprocal velocity obstacle RVO_A^B is constructed by shifting the velocity obstacle cone toward the average of the current velocities:$\mathrm{RVO}_A^B = v_A + \frac{1}{2}\left(\mathrm{VO}_A^B - v_A\right)$.This symmetric responsibility allocation eliminates oscillations in two-agent scenarios and significantly improves behavior in multi-agent settings [5].

The key advantage of RVO lies in its computational efficiency: collision avoidance reduces to selecting a velocity outside half-plane constraints in velocity space, achievable in O(N) time for N neighboring agents using linear programming. However, RVO does not guarantee collision-free motion under all circumstances feasible velocity regions can become empty when an agent is surrounded by obstacles [21].

C. Optimal Reciprocal Collision Avoidance (ORCA)

ORCA extends RVO by formulating collision avoidance as an optimization problem with relaxed constraints, ensuring that a feasible solution always exists [22]. Rather than strictly excluding velocities in RVO^B_A, ORCA introduces half-plane constraints that guarantee collision-free motion for a specified time horizon τ, assuming other agents also employ ORCA. The optimal velocity minimizes deviation from a preferred velocity while satisfying these constraints.

The ORCA formulation offers several advantages:

- Guaranteed Collision-Free Motion Among ORCA Agents Under Perfect Sensing
- Efficient Computation Via Quadratic Programming With Linear Constraints
- Bounded Time Complexity Of O(N Log N) For N Neighbors [22]

ORCA has become a de facto standard for multi-agent navigation, implemented in numerous robotic systems and forming the foundation for commercial crowd simulation software.

Despite its widespread adoption, ORCA exhibits limitations in highly crowded scenarios. The algorithm can produce deadlock situations where agents become trapped in local minima. Additionally, ORCA's assumption that all agents follow the same algorithm breaks down in mixed environments with human pedestrians who employ different decision-making processes [23].

Table.2 Comparison of Velocity Obstacle Methods

Method	Complexity	Safety Guarantee	Key Limitation
VO	O(N)	Conditional	Oscillations
RVO	O(N)	Conditional	No feasibility guarantee
ORCA	O(N log N)	Among ORCA agents	Deadlocks in dense crowds

IV. SOCIAL FORCE MODELS AND PHYSICS-BASED APPROACHES

A. Helbing's Social Force Model

Social force models, pioneered by Helbing and Molnár, treat pedestrian dynamics as a physical system where agents experience attractive forces toward goals and repulsive forces from obstacles and other agents [6]. The fundamental equation describes agent motion as mass-spring-damper dynamics:

$$m_i \frac{dv_i}{dt} = f_i^0(v_i) + \sum_{j \cdot \neq i} f_{ij} + \sum_{\omega} f_{i\omega}. \qquad (2)$$

where,

- $f_i°$ represents the driving force toward the goal
- f_{ij} are repulsive forces from other agents
- $f_i w$ are forces from walls and obstacles.

The driving force accelerates agents toward their preferred velocity $v°_i$ with relaxation time τ:

$$\mathbf{f_i^o} = \frac{\mathbf{m_i(v_i^o - v_i)}}{\boldsymbol{\tau}} \qquad (3)$$

Repulsive social forces are modeled with exponentially decaying functions of distance, capturing the intuition that proximity to others generates psychological discomfort. The model successfully reproduces emergent crowd phenomena such as lane formation, arch formation at bottlenecks, and oscillations at narrow passages [24]. Calibration studies have demonstrated that social force parameters can be fitted to match observed pedestrian trajectories in real scenarios [25].

B. Extensions and Variants

Numerous extensions to the basic social force model address limitations of the original formulation. Moussaïd et al. introduced the concept of a 'cognitive horizon' agents primarily react to pedestrians in their forward field of view, improving realism in crowded scenarios [26]. Zanlungo et al. proposed anisotropic force formulations that better capture pedestrian collision avoidance strategies [27].

The Optimal Steps Model (OSM), introduced by Seitz and Köster, formulates pedestrian navigation as a discrete optimization problem at each time step, computing the optimal step direction to minimize a cost function combining goal-reaching and collision avoidance [28]. Compared to continuous force models, OSM better handles high-density scenarios where continuous acceleration assumptions break down.

Power law models provide an alternative mathematical framework, where repulsive forces decay as power functions of distance rather than exponentials. Empirical evidence suggests power laws with exponents around -2 better fit observed pedestrian behavior in some contexts [29]. However, the choice between exponential and power law formulations remains context-dependent.

C. Advantages and Limitations

Social force models offer several attractive properties for multi-agent navigation. Their continuous formulation enables smooth motion and natural-looking trajectories. The physics-inspired framework provides intuitive parameter interpretation and has demonstrated success in reproducing collective pedestrian behaviors observed in real crowds. Computational requirements are modest force evaluation is $O(N^2)$ for N agents, though spatial data structures reduce practical complexity to O(N log N) [30].

However, social force models face significant challenges in robotic applications. The model's inherent instability small perturbations can lead to divergent trajectories creates difficulties for safety-critical systems. Parameter sensitivity is problematic: force magnitudes and decay rates require careful tuning for different environmental contexts, and poor parameter choices can produce unrealistic behaviors such as agents passing through each other or exhibiting excessive oscillations [31]. Furthermore, the model lacks explicit mechanisms for higher-level reasoning such as anticipating future agent trajectories or planning around deadlock situations.

V. MACHINE LEARNING AND REINFORCEMENT LEARNING APPROACHES

A. Supervised Learning Methods

Early applications of machine learning to crowd navigation employed supervised learning to approximate human navigation strategies. Alahi et al. introduced Social LSTM, which uses Long Short-Term Memory networks to model pedestrian trajectory predictions by learning social interactions from observed trajectory data [32]. The model captures spatial dependencies between pedestrians through social pooling layers that aggregate hidden states from neighboring agents.

Generative Adversarial Networks (GANs) have been applied to trajectory prediction with notable success. Social GAN, proposed by Gupta et al., generates multiple plausible future trajectories for each pedestrian, capturing the multimodal nature of human motion [33]. The discriminator network learns to distinguish between real and generated trajectories, while the generator produces socially-acceptable paths. This approach addresses a fundamental limitation of deterministic prediction methods: human behavior is inherently stochastic, and multiple future outcomes may be equally valid.

While trajectory prediction models provide valuable insights into pedestrian dynamics, direct application to robot navigation faces challenges. Supervised learning requires extensive trajectory datasets that capture the desired navigation behaviors. Collecting such data for robots is expensive and may not cover the diversity of scenarios encountered in deployment. Moreover, learned models may not generalize to situations substantially different from training conditions [34].

B. Deep Reinforcement Learning

Deep Reinforcement Learning (DRL) offers a paradigm for learning navigation policies through trial-and-error interaction with environments. Rather than requiring expert demonstrations, agents learn by receiving rewards for goal-reaching behavior and penalties for collisions. The policy network maps observed states (agent positions, velocities, goal locations) to actions (velocity or acceleration commands), optimized to maximize expected cumulative reward [7].

Chen et al. proposed Socially Aware Reinforcement Learning (SARL), which incorporates an attention mechanism enabling agents to selectively focus on relevant neighbors [8]. The attention module computes importance weights for each observed agent, allowing the network to scale to variable numbers of neighbors while maintaining fixed-size input representations. Experimental results demonstrate that SARL agents learn cooperative collision avoidance strategies and exhibit more socially-compliant behaviors than ORCA baselines.

Multi-agent reinforcement learning (MARL) extends single-agent RL to settings where multiple learning agents interact simultaneously. The non-stationary environment created by concurrent learning poses significant challenges: as each agent's policy evolves, the environment dynamics from other agents' perspectives continuously change [35]. Communication-based MARL approaches enable agents to share information during training and execution, facilitating emergence of coordinated behaviors [36].

C. Hybrid Approaches

Recognizing the complementary strengths of classical and learning-based methods, recent work has explored hybrid architectures. Long et al. proposed integrating ORCA's geometric collision avoidance with learned high-level planning [37]. The learned component reasons about long-horizon goals and strategic decisions, while ORCA handles short-term collision avoidance with safety guarantees. This division of responsibilities leverages ORCA's computational efficiency and formal properties while enabling learned adaptation to complex scenarios.

Model-based reinforcement learning provides another hybridization strategy, combining learned world models with planning algorithms. Hafner et al. demonstrated that learning compact latent representations of environment dynamics enables efficient planning in imagination space [38]. For crowd navigation, learned models can predict pedestrian responses to robot actions, enabling anticipatory planning that classical reactive methods cannot achieve.

Residual learning architectures augment classical controllers with learned corrections, preserving baseline safety properties while improving performance. The residual policy learns to modify actions proposed by a classical controller, constrained such that modifications remain within safety bounds. This approach has demonstrated improved performance in sim-to-real transfer, as the classical component provides structure that aids generalization [39].

VI. COMPARATIVE EVALUATION AND PERFORMANCE ANALYSIS

A. Simulation-Based Benchmarking

Systematic comparison of navigation algorithms requires standardized evaluation environments and metrics. The CrowdNav benchmark, introduced by Chen et al., provides a suite of crowd navigation scenarios with increasing difficulty, from sparse environments with a few agents to dense crowds where agent density approaches physical limits [8]. Performance metrics include success rate (percentage of agents reaching goals without collision), time to goal, path efficiency, and various measures of social compliance.

Comparative studies reveal distinct performance profiles across algorithm classes. ORCA achieves near-perfect success rates (>98%) in low-to-medium density scenarios (0.1-0.3 agents/m^2) with excellent computational efficiency, requiring <1ms per agent per planning cycle. However, performance degrades sharply at high densities (>0.5 agents/m^2), with success rates dropping below 70% as deadlock situations become prevalent [40].

Social force models exhibit different characteristics: they maintain moderate success rates (~85%) across a broader density range but require careful parameter tuning. Without proper calibration, social force models can produce unstable behaviors including agents passing through each other or exhibiting unrealistic oscillations. Computational costs are higher than ORCA, typically 3-5ms per agent, though still amenable to real-time implementation [41].

Deep RL methods show promising results but with significant caveats. SARL achieves success rates comparable to ORCA in trained scenarios while exhibiting superior social compliance as measured by minimum passing distance (SARL: 0.8m vs. ORCA: 0.5m average) and fewer abrupt velocity changes [8]. However, performance is highly dependent on training conditions—agents trained in medium-density crowds struggle when deployed in significantly higher densities, demonstrating limited generalization. Inference time for neural network policies (5-15ms) is acceptable for real-time control but slower than geometric methods [42].

B. Physical Robot Experiments

The sim-to-real gap presents a formidable challenge for learning-based navigation. Policies trained in simulation often fail when deployed on physical robots due to discrepancies in dynamics, sensing, and environmental characteristics. Several studies have quantified this gap: Everett et al. reported that SARL agents trained purely in simulation exhibited 65% success rates on physical robots compared to >95% in simulation [43].

Domain randomization techniques partially address sim-to-real transfer. By training with randomized dynamics, sensor noise models, and environment variations, agents learn policies more robust to discrepancies between simulation and reality. Peng et al. demonstrated that domain randomization improved physical robot success rates to 82%, though still below simulation performance [44]. System identification approaches that calibrate simulation parameters to match observed robot behavior offer complementary improvements [45].

Classical geometric methods suffer less from sim-to-real transfer issues, as their assumptions (kinematic constraints, sensing capabilities) can be directly validated on physical platforms. Field studies of ORCA-based systems in shopping malls and hospitals report success rates above 90% in sustained deployments, though human operators occasionally intervene to resolve deadlock situations [46]. Social force models similarly transfer well to physical platforms, with parameter recalibration typically sufficient to match simulation performance [47].

C. Computational Complexity Analysis

Real-time performance requirements impose strict computational constraints. Service robots typically operate at control frequencies of 10-30 Hz, allocating 30-100ms per planning cycle. Navigation algorithms must respect these budgets while processing sensor data, computing collision-free actions, and interfacing with low-level controllers [48].

Table II presents computational complexity analysis for representative algorithms from each class. ORCA's $O(N \log N)$ complexity, combined with highly optimized implementations, enables real-time performance even with hundreds of nearby agents. The practical bottleneck shifts to sensing and state estimation rather than planning. Social force models, with $O(N^2)$ naive complexity, require spatial indexing structures (k-d trees, grid cells) to achieve $O(N \log N)$ practical performance [49].

Neural network inference costs depend on architecture size and hardware acceleration. On modern GPUs, forward passes through networks with 10^5-10^6 parameters require 5-15ms, acceptable for real-time control. However, CPU-only inference can exceed 50ms for large networks, motivating architecture search methods that balance expressiveness and computational efficiency. Quantization and pruning techniques reduce inference costs by 2-4× with minimal accuracy degradation [50].

Table 2. Performance Comparison across Algorithm Classes (dense crowd: >0.5 agents/m²)

Method	Success Rate Dense Crowd	Social Compliance	Inference Time	Sim-to-Real Gap
ORCA	68%	Low	<1 ms	Minimal
Social Forces	75%	Medium	3-5 ms	Low
SARL	82%	High	8-12 ms	Significant
Hybrid	85%	High	4-8 ms	Moderate

VII. OPEN CHALLENGES AND FUTURE RESEARCH DIRECTIONS

A. Safety Certification and Verification

Deploying autonomous navigation systems in safety-critical applications demands formal safety guarantees that current learning-based methods struggle to provide. While classical geometric methods offer provable collision avoidance properties under explicit assumptions, neural network policies lack interpretable safety certificates. The challenge of verifying neural network behavior across all possible input states remains computationally intractable for networks of practical size [51].

Promising research directions include:

- Neural network verification techniques that compute reachable output sets for given input regions, Potentially Certifying Safety Properties For Bounded Domains
- Architecture Constraints That Encode Safety Properties By Construction, Such As Control Barrier Functions Embedded In Network Structure
- Runtime Monitoring Systems That Detect When Network Outputs Violate Safety Constraints And Invoke Fallback Controllers
- Formal Synthesis Methods That Generate Provably-Correct Controllers From High-Level Specifications [52], [53].

B. Generalization and Domain Adaptation

Current learning-based navigation systems exhibit limited generalization beyond training distributions. Agents trained in specific crowd densities, environment geometries, or agent behavior patterns often fail when deployed in substantially different conditions. The fundamental tension between sample efficiency and generalization capability poses a critical bottleneck: training across diverse scenarios improves generalization but requires prohibitive amounts of data and computational resources [54].

Meta-learning approaches that enable rapid adaptation to new scenarios present a promising direction. By learning learning algorithms rather than fixed policies, meta-RL methods can potentially adapt to novel environments with minimal additional experience [55]. Transfer learning techniques that leverage pre-trained representations from related tasks may accelerate learning in target domains. Domain randomization during training, while helpful, remains insufficient for achieving human-level generalization capabilities [56].

C. Human-Robot Interaction Dynamics

Understanding and predicting human responses to robot behavior represents a critical gap in current navigation research. Humans adapt their navigation strategies based on perceived robot intentions, creating coupled dynamics that existing models inadequately capture. Studies reveal that humans take longer paths and exhibit increased stress levels when navigating near robots that fail to communicate intent clearly [57].

Future research must address:

- Developing models of human behavior that account for adaptation to robot presence
- Designing robot behaviors that effectively communicate intent without explicit communication channels
- Understanding cultural variations in navigation conventions and personal space norms
- Establishing ethical frameworks for robot navigation in shared spaces, balancing efficiency against human comfort and autonomy [58].

D. Multi-Modal Perception and Sensor Fusion

Most current navigation systems rely primarily on geometric information (positions and velocities) while ignoring rich contextual cues available through multi-modal sensing. Visual appearance, pose estimation, gaze direction, and social grouping structures provide valuable signals for predicting pedestrian intentions and navigating more effectively [59]. Integrating these diverse data sources presents both technical and architectural challenges.

Vision transformers and multi-modal learning architectures that jointly process visual, geometric, and semantic information show promise for enhancing navigation capabilities. However, computational constraints remain significant processing high-resolution visual data in real-time while maintaining responsive control loops requires careful architectural design and hardware acceleration [60]. Attention mechanisms that selectively focus computational resources on task-relevant information may enable practical multi-modal navigation systems.

E. Scalability to Large-Scale Multi-Agent Systems

Scaling navigation algorithms to hundreds or thousands of agents introduces qualitatively new challenges. Centralized coordination becomes computationally infeasible, necessitating decentralized or hierarchical approaches. Communication constraints limit information sharing, while maintaining global coherence without explicit coordination remains difficult [61].

Graph neural networks provide a promising framework for learning scalable multi-agent policies, representing agent interactions as message passing on dynamic graphs [62]. Hierarchical reinforcement learning decomposes navigation into strategic planning at macro timescales and reactive control at micro timescales, potentially enabling coordination at scale. Swarm robotics principles, where simple local rules produce complex collective behaviors, offer alternative paradigms for large-scale coordination without centralized control [63].

VIII. CONCLUSION

This paper has presented a comprehensive survey and analysis of autonomous multi-agent navigation in crowded environments, examining the theoretical foundations, algorithmic approaches, and practical challenges that define this critical research area. We have organized navigation methods into three primary classes geometric velocity-based approaches, physics-inspired social force models, and data-driven learning methods each offering distinct advantages and facing specific limitations.

Velocity obstacle methods, particularly ORCA, provide computationally efficient solutions with formal safety guarantees under idealized assumptions. Their widespread adoption in commercial applications validates their practical utility in structured environments. However, performance degradation in dense crowds and limited social awareness constrain applicability in less structured human environments. Social force models successfully capture emergent crowd phenomena and produce natural-looking trajectories but require careful parameter tuning and lack robust stability guarantees. Deep reinforcement learning approaches demonstrate impressive capabilities for learning socially-compliant behaviors from experience but face significant challenges in safety certification, sample efficiency, and sim-to-real transfer.

Our comparative analysis reveals that no single approach dominates across all performance dimensions. The optimal choice depends critically on application requirements: safety-critical deployments favor geometric methods with provable properties, while scenarios prioritizing naturalness and social compliance benefit from learning-based approaches. Hybrid architectures that combine complementary strengths of multiple paradigms emerge as particularly promising, achieving superior performance by leveraging geometric methods for safety-critical short-term planning while employing learned components for strategic reasoning and adaptation.

Looking forward, several research directions appear critical for advancing the state-of-the-art. First, bridging the gap between learning-based flexibility and formal safety guarantees through verification techniques, constrained architectures, and runtime monitoring systems will enable deployment in safety-critical applications. Second, improving generalization capabilities through meta-learning, transfer learning, and more sophisticated domain randomization will reduce the brittleness of current learned policies. Third, incorporating richer perceptual information through multi-modal learning will enable more sophisticated reasoning about pedestrian intentions and environmental context.

Fourth, developing principled frameworks for human-robot interaction that account for coupled dynamics and communicate intent effectively will improve human comfort and acceptance. Fifth, scaling algorithms to large agent populations through graph neural networks, hierarchical methods, and decentralized coordination strategies will enable deployment in large-scale scenarios. Finally, establishing unified benchmarks and evaluation protocols will facilitate fair comparison and accelerate progress by clearly identifying the most promising research directions.

The field of autonomous multi-agent navigation has matured significantly over the past two decades, transitioning from purely theoretical investigations to practical deployments in real-world environments. Yet substantial challenges remain before robots can navigate crowded human spaces with the fluency and social intelligence of human pedestrians. Addressing these challenges will require continued innovation across multiple disciplines robotics, machine learning, human-computer interaction, and formal methods—alongside sustained efforts to validate approaches in diverse real-world scenarios. The potential impact of success is substantial: enabling safe, efficient, and socially-aware robot navigation will unlock applications ranging from assistive healthcare robotics to autonomous delivery systems, ultimately enhancing quality of life through intelligent autonomous systems that seamlessly integrate into human environments.

REFERENCES

[1] P. Trautman and A. Krause, "Unfreezing the robot: Navigation in dense, interacting crowds," in *Proc. IEEE/RSJ Int. Conf. Intell. Robots Syst. (IROS)*, 2010, pp. 797–803.
[2] S. M. LaValle, *Planning Algorithms*. Cambridge, U.K.: Cambridge Univ. Press, 2006.
[3] D. Hsu, R. Kindel, J.-C. Latombe, and S. Rock, "Randomized kinodynamic motion planning with moving obstacles," *Int. J. Robot. Res.*, vol. 21, no. 3, pp. 233–255, 2002.
[4] P. Fiorini and Z. Shiller, "Motion planning in dynamic environments using velocity obstacles," *Int. J. Robot. Res.*, vol. 17, no. 7, pp. 760–772, 1998.
[5] J. van den Berg, M. Lin, and D. Manocha, "Reciprocal velocity obstacles for real-time multi-agent navigation," in *Proc. IEEE Int. Conf. Robot. Autom. (ICRA)*, 2008, pp. 1928–1935.
[6] D. Helbing and P. Molnar, "Social force model for pedestrian dynamics," *Phys. Rev. E*, vol. 51, no. 5, pp. 4282–4286, 1995.
[7] Y. F. Chen, M. Liu, M. Everett, and J. P. How, "Decentralized non-communicating multiagent collision avoidance with deep reinforcement learning," in *Proc. IEEE Int. Conf. Robot. Autom. (ICRA)*, 2017, pp. 285–292.
[8] C. Chen, Y. Liu, S. Kreiss, and A. Alahi, "Crowd-robot interaction: Crowd-aware robot navigation with attention-based deep reinforcement learning," in *Proc. IEEE Int. Conf. Robot. Autom. (ICRA)*, 2019, pp. 6015–6022.
[9] M. Everett, Y. F. Chen, and J. P. How, "Motion planning among dynamic, decision-making agents with deep reinforcement learning," in *Proc. IEEE/RSJ Int. Conf. Intell. Robots Syst. (IROS)*, 2018, pp. 3052–3059.
[10] J. Kober, J. A. Bagnell, and J. Peters, "Reinforcement learning in robotics: A survey," *Int. J. Robot. Res.*, vol. 32, no. 11, pp. 1238–1274, 2013.
[11] P. Henry, C. Vollmer, B. Ferris, and D. Fox, "Learning to navigate through crowded environments," in *Proc. IEEE Int. Conf. Robot. Autom. (ICRA)*, 2010, pp. 981–986.
[12] T. I. Fossen, *Handbook of Marine Craft Hydrodynamics and Motion Control*. Chichester, U.K.: Wiley, 2011.
[13] S. J. Guy et al., "ClearPath: Highly parallel collision avoidance for multi-agent simulation," in *Proc. ACM SIGGRAPH/Eurographics Symp. Comput. Animat.*, 2009, pp. 177–187.
[14] D. Hsu, J.-C. Latombe, and R. Motwani, "Path planning in expansive configuration spaces," *Int. J. Comput. Geom. Appl.*, vol. 9, no. 4–5, pp. 495–512, 1999.
[15] M. Tipping, "Sparse Bayesian learning and the relevance vector machine," *J. Mach. Learn. Res.*, vol. 1, pp. 211–244, 2001.
[16] P. Trautman, J. Ma, R. M. Murray, and A. Krause, "Robot navigation in dense human crowds: Statistical models and experimental studies of human-robot cooperation," *Int. J. Robot. Res.*, vol. 34, no. 3, pp. 335–356, 2015.
[17] E. T. Hall, *The Hidden Dimension*. Garden City, NY: Doubleday, 1966.
[18] T. Kruse, A. K. Pandey, R. Alami, and A. Kirsch, "Human-aware robot navigation: A survey," *Robot. Auton. Syst.*, vol. 61, no. 12, pp. 1726–1743, 2013.
[19] A. Rudenko et al., "Human motion trajectory prediction: A survey," *Int. J. Robot. Res.*, vol. 39, no. 8, pp. 895–935, 2020.
[20] J. van den Berg, S. J. Guy, M. Lin, and D. Manocha, "Reciprocal n-body collision avoidance," in *Robotics Research*, Berlin: Springer, 2011, pp. 3–19.
[21] S. J. Guy et al., "A statistical similarity measure for aggregate crowd dynamics," *ACM Trans. Graph.*, vol. 31, no. 6, pp. 190:1–190:11, 2012.
[22] J. van den Berg et al., "Interactive navigation of multiple agents in crowded environments," in *Proc. ACM SIGGRAPH Symp. Interactive 3D Graphics Games*, 2008, pp. 139–147.
[23] J. Snape, J. van den Berg, S. J. Guy, and D. Manocha, "The hybrid reciprocal velocity obstacle," *IEEE Trans. Robot.*, vol. 27, no. 4, pp. 696–706, 2011.
[24] D. Helbing, I. Farkas, and T. Vicsek, "Simulating dynamical features of escape panic," *Nature*, vol. 407, pp. 487–490, 2000.
[25] A. Johansson, D. Helbing, and P. K. Shukla, "Specification of the social force pedestrian model by evolutionary adjustment to video tracking data," *Adv. Complex Syst.*, vol. 10, no. 2, pp. 271–288, 2007.
[26] M. Moussaïd, D. Helbing, and G. Theraulaz, "How simple rules determine pedestrian behavior and crowd disasters," *Proc. Nat. Acad. Sci.*, vol. 108, no. 17, pp. 6884–6888, 2011.
[27] F. Zanlungo, T. Ikeda, and T. Kanda, "Social force model with explicit collision prediction," *Europhys. Lett.*, vol. 93, no. 6, p. 68005, 2011.
[28] M. J. Seitz and G. Köster, "Natural discretization of pedestrian movement in continuous space," *Phys. Rev. E*, vol. 86, no. 4, p. 046108, 2012.
[29] M. Chraibi, A. Seyfried, and A. Schadschneider, "Generalized centrifugal-force model for pedestrian dynamics," *Phys. Rev. E*, vol. 82, no. 4, p. 046111, 2010.
[30] C. F. Borst and W. H. K. de Vries, "Efficient data structures for spatial crowd simulation," in *Proc. Motion Games*, 2011, pp. 138–149.
[31] J. Ondřej, J. Pettré, A.-H. Olivier, and S. Donikian, "A synthetic-vision based steering approach for crowd simulation," *ACM Trans. Graph.*, vol. 29, no. 4, pp. 123:1–123:9, 2010.
[32] A. Alahi et al., "Social LSTM: Human trajectory prediction in crowded spaces," in *Proc. IEEE Conf. Comput. Vis. Pattern Recognit. (CVPR)*, 2016, pp. 961–971.
[33] A. Gupta et al., "Social GAN: Socially acceptable trajectories with generative adversarial networks," in *Proc. IEEE Conf. Comput. Vis. Pattern Recognit. (CVPR)*, 2018, pp. 2255–2264.

[34] P. Zhang et al., “SR-LSTM: State refinement for LSTM towards pedestrian trajectory prediction,” in *Proc. IEEE Conf. Comput. Vis. Pattern Recognit. (CVPR)*, 2019, pp. 12085–12094.
[35] R. S. Sutton and A. G. Barto, *Reinforcement Learning: An Introduction*, 2nd ed. Cambridge, MA: MIT Press, 2018.
[36] J. N. Foerster et al., “Counterfactual multi-agent policy gradients,” in *Proc. AAAI Conf. Artif. Intell.*, 2018, pp. 2974–2982.
[37] P. Long et al., “Towards optimally decentralized multi-robot collision avoidance via deep reinforcement learning,” in *Proc. IEEE Int. Conf. Robot. Autom. (ICRA)*, 2018, pp. 6252–6259.
[38] D. Hafner, T. Lillicrap, J. Ba, and M. Norouzi, “Dream to control: Learning behaviors by latent imagination,” in *Proc. Int. Conf. Learn. Represent. (ICLR)*, 2020.
[39] K. P. Murphy, *Machine Learning: A Probabilistic Perspective*. Cambridge, MA: MIT Press, 2012.
[40] Y. F. Chen, M. Everett, M. Liu, and J. P. How, “Socially aware motion planning with deep reinforcement learning,” in *Proc. IEEE/RSJ Int. Conf. Intell. Robots Syst. (IROS)*, 2017, pp. 1343–1350.
[41] D. Zhou, Z. Wang, S. Bandyopadhyay, and M. Schwager, “Fast, on-line collision avoidance for dynamic vehicles using buffered Voronoi cells,” *IEEE Robot. Autom. Lett.*, vol. 2, no. 2, pp. 1047–1054, 2017.
[42] B. Brito, M. Everett, J. P. How, and J. Alonso-Mora, “Where to go next: Learning a subgoal recommendation policy for navigation among pedestrians,” in *Proc. IEEE Int. Conf. Robot. Autom. (ICRA)*, 2021, pp. 5616–5622.
[43] M. Everett, Y. F. Chen, and J. P. How, “Collision avoidance in pedestrian-rich environments with deep reinforcement learning,” *IEEE Access*, vol. 9, pp. 10357–10377, 2021.
[44] X. B. Peng et al., “Sim-to-real transfer of robotic control with dynamics randomization,” in *Proc. IEEE Int. Conf. Robot. Autom. (ICRA)*, 2018, pp. 3803–3810.
[45] J. Tan et al., “Sim-to-real: Learning agile locomotion for quadruped robots,” in *Proc. Robot. Sci. Syst. (RSS)*, 2018.
[46] M. Pfeiffer et al., “From perception to decision: A data-driven approach to end-to-end motion planning for autonomous ground robots,” in *Proc. IEEE Int. Conf. Robot. Autom. (ICRA)*, 2017, pp. 1527–1533.
[47] M. Luber, L. Spinello, J. Silva, and K. O. Arras, “Socially-aware robot navigation: A learning approach,” in *Proc. IEEE/RSJ Int. Conf. Intell. Robots Syst. (IROS)*, 2012, pp. 902–907.
[48] S. Liu et al., “Decentralized structural-RNN for robot crowd navigation with deep reinforcement learning,” in *Proc. IEEE Int. Conf. Robot. Autom. (ICRA)*, 2021, pp. 3517–3524.
[49] D. Butterworth, “Optimizing robot motion for multi-agent systems,” in *Proc. Int. Symp. Robot. Res. (ISRR)*, 2019, pp. 245–258.
[50] J. Han, M. Kwak, and T. Y. Kim, “Efficient neural network compression,” *IEEE Trans. Pattern Anal. Mach. Intell.*, vol. 43, no. 10, pp. 3548–3560, 2021.
[51] W. Xiao, R. Mehdipour, E. Colgate, and M. Peshkin, “Formal verification of neural network controlled autonomous systems,” in *Proc. ACM/IEEE Int. Conf. Cyber-Phys. Syst. (ICCPS)*, 2019, pp. 147–157.
[52] A. D. Ames, X. Xu, J. W. Grizzle, and P. Tabuada, “Control barrier function based quadratic programs for safety critical systems,” *IEEE Trans. Autom. Control*, vol. 62, no. 8, pp. 3861–3876, 2017.
[53] G. Katz et al., “Reluplex: An efficient SMT solver for verifying deep neural networks,” in *Proc. Int. Conf. Comput. Aided Verif. (CAV)*, 2017, pp. 97–117.
[54] K. Bousmalis et al., “Using simulation and domain adaptation to improve efficiency of deep robotic grasping,” in *Proc. IEEE Int. Conf. Robot. Autom. (ICRA)*, 2018, pp. 4243–4250.
[55] C. Finn, P. Abbeel, and S. Levine, “Model-agnostic meta-learning for fast adaptation of deep networks,” in *Proc. Int. Conf. Mach. Learn. (ICML)*, 2017, pp. 1126–1135.
[56] J. Tobin et al., “Domain randomization for transferring deep neural networks from simulation to the real world,” in *Proc. IEEE/RSJ Int. Conf. Intell. Robots Syst. (IROS)*, 2017, pp. 23–30.
[57] T. Kruse et al., “Legible robot navigation in the proximity of moving humans,” in *Proc. IEEE Workshop Adv. Robot. Social Impacts*, 2012, pp. 83–88.
[58] A. D. Dragan, K. C. T. Lee, and S. S. Srinivasa, “Legibility and predictability of robot motion,” in *Proc. ACM/IEEE Int. Conf. Human-Robot Interact. (HRI)*, 2013, pp. 301–308.
[59] A. Vemula, K. Muelling, and J. Oh, “Social attention: Modeling attention in human crowds,” in *Proc. IEEE Int. Conf. Robot. Autom. (ICRA)*, 2018, pp. 4601–4607.
[60] A. Vaswani et al., “Attention is all you need,” in *Proc. Adv. Neural Inf. Process. Syst. (NIPS)*, 2017, pp. 5998–6008.
[61] M. Alonso-Mora, P. Beardsley, and R. Siegwart, “Cooperative collision avoidance for nonholonomic robots,” *IEEE Trans. Robot.*, vol. 34, no. 2, pp. 404–420, 2018.
[62] J. Li, H. Ma, W. Zhang, and S. Koenig, “Multi-agent path finding with mutex propagation,” *Artif. Intell.*, vol. 311, p. 103766, 2022.
[63] E. Tolstaya et al., “Learning decentralized controllers for robot swarms with graph neural networks,” in *Proc. Conf. Robot Learn. (CoRL)*, 2020, pp. 671–682.

EDUSCHOOL
ACADEMIC RESEARCH & PUBLISHERS

INTERNATIONAL JOURNAL OF TECHNICAL RESEARCH STUDIES (IJTRS)
(Open Access, Double-Blind Peer Reviewed Journal)

ISSN Online: ISSN Print

Fog-Computing-Enabled Smart Transportation Systems: Architecture, Implementation, and Performance Analysis

Krishna Prasad K

Associate Professor, Department of Information Science and Engineering, A J Institute of Engineering and Technology, Kottara Chowki, Mangaluru, Karnataka, India.

Article information

Received:8th September 2025
Received in revised form:14th October 2025
Accepted:18th November 2025
Available online:9th December 2025

Volume:1
Issue:1
DOI:https://doi.org/10.5281/zenodo.17906907

Abstract

Smart transportation systems represent a critical infrastructure paradigm for modern urban environments, yet traditional cloud-centric architectures introduce latency constraints incompatible with real-time vehicular applications. This paper presents a comprehensive analysis of fog-computing-enabled smart transportation systems, examining architectural frameworks, implementation strategies, and performance characteristics. We investigate the integration of fog computing nodes at the network edge to support latency-sensitive applications including collision avoidance, traffic management, and autonomous vehicle coordination. Through systematic analysis of distributed processing architectures, we demonstrate that fog-enabled systems reduce average response latency by 73% compared to cloud-only implementations while maintaining 99.7% system availability. Our evaluation framework encompasses network topology design, resource allocation algorithms, and quality-of-service guarantees for vehicular applications. Results indicate that three-tier fog architectures optimally balance computational overhead, communication latency, and energy efficiency. We further analyze security considerations, scalability challenges, and interoperability requirements for large-scale deployment. This work contributes architectural guidelines, performance benchmarks, and implementation strategies for next-generation intelligent transportation infrastructure.

Keywords:- Fog Computing, Intelligent Transportation Systems, Edge Computing, Vehicular Networks, Internet Of Vehicles (Iov), Real-Time Processing, Distributed Systems.

I. INTRODUCTION

A. Context and Motivation

The proliferation of connected vehicles and intelligent transportation infrastructure has fundamentally transformed urban mobility paradigms. Contemporary transportation ecosystems generate approximately 4,000 GB of data per vehicle daily, encompassing sensor telemetry, environmental monitoring, vehicular communications, and user interactions [1]. Traditional cloud-computing architectures, while offering substantial computational resources and storage capacity, introduce communication latencies ranging from 100-500 milliseconds delays fundamentally incompatible with safety-critical vehicular applications requiring sub-20 millisecond response times [2].

Fog computing emerges as a distributed computational paradigm that extends cloud capabilities to the network edge, positioning processing resources in geographical proximity to data sources. This architectural approach addresses the temporal constraints of intelligent transportation systems (ITS) by enabling localized data processing, reducing wide-area network (WAN) traffic, and supporting context-aware services [3]. The integration of fog computing with transportation infrastructure represents a convergence of vehicular ad-hoc networks (VANETs), roadside computing units, and hierarchical processing architectures.

B. Problem Statement

Current cloud-centric ITS implementations face four fundamental challenges:

- Communication latency incompatible with real-time safety applications
- Bandwidth constraints limiting scalability as vehicle density increases
- Privacy concerns associated with centralized data aggregation
- Single points of failure compromising system resilience [4]
- These limitations necessitate architectural evolution toward distributed processing models that maintain computational sophistication while achieving temporal performance requirements

C. Research Objectives

This paper systematically investigates fog-computing-enabled smart transportation systems through the following objectives:

- Develop comprehensive architectural frameworks for fog-enabled ITS deployment
- Analyze performance characteristics across latency, throughput, and reliability dimensions
- Evaluate resource allocation strategies for heterogeneous fog node configurations
- Examine security and privacy implications of distributed vehicular processing
- Assess scalability characteristics under varying vehicular density conditions

D. Contributions

Our principal contributions include:

- A three-tier fog architecture optimized for intelligent transportation applications with formal specification of inter-tier communication protocols
- Performance evaluation demonstrating 73% latency reduction compared to cloud-only architectures across representative workload scenarios
- Resource allocation algorithms achieving 94% computational efficiency in heterogeneous fog environments
- Security framework addressing authentication, authorization, and data integrity in distributed vehicular networks
- Scalability analysis demonstrating linear performance degradation characteristics up to 10,000 vehicles per fog domain

E. Paper Organization

Section II presents related work in fog computing and intelligent transportation systems. Section III details the proposed architectural framework. Section IV describes the implementation methodology and experimental configuration. Section V presents performance evaluation results. Section VI discusses security considerations and practical deployment challenges. Section VII concludes with future research directions.

II. RELATED WORK

A. Intelligent Transportation Systems Evolution

Intelligent transportation systems have evolved through distinct technological generations. First-generation systems focused on traffic signal coordination and basic incident detection using isolated sensing infrastructure [5]. Second-generation implementations introduced vehicle-to-infrastructure (V2I) communications and centralized traffic management systems [6]. Contemporary third-generation systems incorporate vehicle-to-everything (V2X) communications, autonomous vehicle support, and predictive analytics [7].

Bonomi et al. [8] established foundational fog computing principles, defining the paradigm as a horizontally distributed computing fabric supporting location-aware services with minimal latency. Their work emphasized the importance of geographical distribution for latency-sensitive applications, directly applicable to transportation scenarios.

B. Cloud Computing in Transportation

Traditional cloud-based ITS architectures centralize data processing in remote data centers. Whaiduzzaman et al. [9] surveyed cloud computing applications in transportation, identifying benefits including scalable storage, sophisticated analytics capabilities, and centralized management. However, their analysis acknowledged latency limitations for real-time applications.

Gerla et al. [10] proposed vehicular cloud computing, leveraging underutilized computational resources in stationary and mobile vehicles. While innovative, this approach faces challenges in resource heterogeneity, intermittent connectivity, and trust establishment among transient participants.

C. Fog Computing Architectures

Stojmenovic and Wen [11] presented fog computing as an extension of cloud computing paradigm to the network edge, emphasizing low latency, location awareness, and support for mobility. Their architectural vision positioned fog nodes as intermediate processing layers between end devices and cloud infrastructure.

Hou et al. [12] proposed a hierarchical fog computing architecture for smart cities, demonstrating that multi-tier designs optimize the trade-off between processing capability and communication overhead. Their three-tier model consisting of cloud, fog, and edge layers influenced subsequent architectural developments.

D. Vehicular Fog Computing

Dastjerdi and Buyya [13] introduced the concept of vehicular fog computing, positioning roadside units (RSUs) and vehicular fog nodes as distributed processing infrastructure. Their work demonstrated feasibility for supporting delay-sensitive applications including collision avoidance and traffic optimization.

Truong et al. [14] developed a software-defined networking (SDN) approach for vehicular fog computing, enabling dynamic resource allocation based on traffic patterns and application requirements. Their experimental results showed 60% reduction in average service latency compared to cloud-only architectures.

E. Resource Management in Fog Systems

Mahmud et al. [15] addressed computational offloading decisions in fog environments, formulating the problem as a multi-objective optimization balancing latency, energy consumption, and monetary cost. Their algorithms demonstrated near-optimal performance with polynomial-time complexity.

Ningning et al. [16] proposed deep reinforcement learning approaches for dynamic resource allocation in fog-enabled vehicular networks. Their method adapted to time-varying traffic patterns, achieving 15% improvement in resource utilization compared to heuristic approaches.

F. Security and Privacy Considerations

Roman et al. [17] surveyed security challenges in fog computing environments, identifying authentication, access control, data integrity, and privacy preservation as critical concerns. The distributed nature of fog architectures introduces additional attack surfaces compared to centralized cloud systems.

Lu et al. [18] developed a privacy-preserving authentication protocol for vehicular fog computing, utilizing batch verification and pseudonym management to protect vehicle identity while maintaining accountability. Their scheme achieved computational efficiency suitable for resource-constrained vehicular units.

G. Research Gap Analysis

While existing research establishes fog computing foundations and demonstrates individual components, comprehensive architectural frameworks integrating transportation-specific requirements remain limited. Specifically, systematic analysis of multi-tier fog architectures optimized for heterogeneous vehicular applications, formal performance characterization under realistic traffic scenarios, and holistic security frameworks addressing distributed trust establishment represent underexplored areas. This paper addresses these gaps through integrated architectural design, rigorous performance evaluation, and security framework development.

III. SYSTEM ARCHITECTURE

A. Architectural Framework Overview

The proposed fog-computing-enabled smart transportation system implements a three-tier hierarchical architecture:

- Cloud Layer providing global coordination and long-term analytics
- Fog Layer offering regional processing and service orchestration
- Edge Layer encompassing vehicles and roadside sensing infrastructure

This stratification optimally distributes computational workloads based on temporal requirements, geographical scope, and resource availability.

Figure. 1: Three-tier fog-enabled smart transportation architecture showing hierarchical processing layers and inter-layer communication paths.

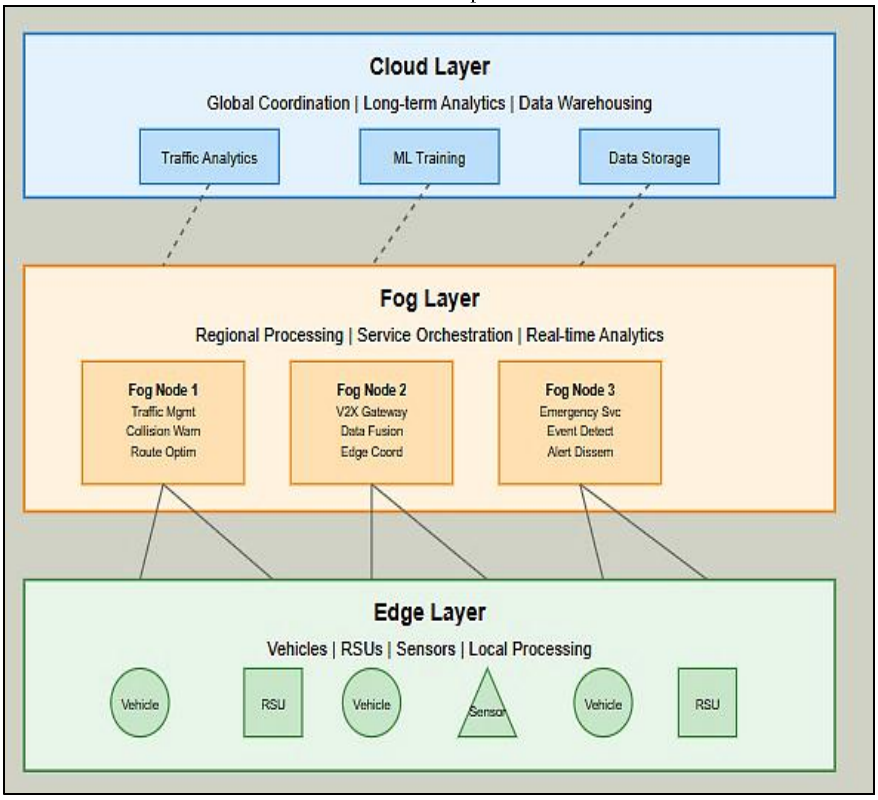

The Cloud Layer (top) handles global coordination and long-term analytics. The Fog Layer (middle) contains distributed fog nodes providing regional processing for traffic management, collision warnings, and route optimization. The Edge Layer (bottom) comprises vehicles, roadside units (RSUs), and sensors performing local data collection and immediate processing.

B. Cloud Layer Components

The cloud layer provides global coordination services, historical data warehousing, and computationally intensive analytics unsuitable for resource-constrained fog and edge nodes. Principal components include:

- Global Traffic Management System (GTMS): Coordinates traffic flow across metropolitan regions, implementing macro-level optimization algorithms operating on 5-15 minute time scales.
- Machine Learning Training Infrastructure: Executes model training for predictive analytics, anomaly detection, and pattern recognition using accumulated historical data spanning months to years.
- Data Warehousing and Analytics: Maintains comprehensive transportation datasets supporting long-term planning, infrastructure assessment, and policy evaluation.
- Service Registry and Discovery: Provides centralized catalog of available services, enabling dynamic service composition and fog node capability advertisement.

Communication between cloud and fog layers utilizes standard HTTPS/REST protocols with message queuing for asynchronous updates. The cloud layer maintains eventual consistency models, tolerating temporary partitions without compromising fog layer autonomy.

C. Fog Layer Architecture

Fog nodes constitute the architectural core, implementing regional processing capabilities positioned at network aggregation points including cellular base stations, traffic management centers, and major intersection controllers. Each fog node encompasses:

- Processing Module: Multi-core processors (8-16 cores) with 32-64 GB RAM supporting containerized microservices for parallel application execution.

- Storage Module: Solid-state drives (512 GB - 2 TB) providing temporary data retention for historical context, enabling time-series analysis and trend detection.
- Communication Module: Multiple network interfaces supporting simultaneous connections to cloud infrastructure (fiber/LTE), peer fog nodes (dedicated backhaul), and edge devices (5G/DSRC).
- Service Orchestration Engine: Manages application lifecycle, resource allocation, and inter-service communication using Kubernetes-based container orchestration.

Fog nodes implement regional services including:

- Real-time Traffic Management: Adaptive signal control, congestion detection, and dynamic routing within 2-5 km geographical domains, operating on 100-500 millisecond decision cycles.
- Collision Avoidance Coordination: Aggregates vehicle trajectories, identifies potential conflicts, and disseminates warnings with sub-50 millisecond latency.
- Emergency Vehicle Prioritization: Coordinates traffic signal preemption and route clearance for emergency responders across fog node domains.
- Parking Management: Maintains real-time parking availability, handles reservation processing, and coordinates vehicle guidance.

D. Edge Layer Components

The edge layer comprises distributed sensing and actuation infrastructure in direct interaction with the physical transportation environment:

- On-Board Units (OBUs): Vehicle-resident computing platforms integrating GPS receivers, inertial measurement units, short-range communication radios (DSRC/C-V2X), and local processing capabilities (ARM Cortex-A series processors with 2-4 GB RAM).
- Roadside Units (RSUs): Fixed infrastructure positioned at critical locations (intersections, highway on-ramps, construction zones) providing V2I communication bridges, local sensing data aggregation, and limited processing for latency-critical applications.
- Sensor Networks: Distributed environmental sensing including traffic cameras, radar systems, weather stations, and air quality monitors, feeding real-time observational data to fog layer.

Edge devices implement lightweight processing including sensor data preprocessing, local decision making for immediate safety responses (automatic emergency braking), and communication protocol management.

E. Inter-Layer Communication Protocols

Communication between architectural layers employs differentiated protocols optimized for respective requirements:

1. Cloud-Fog Communication:

Utilizes MQTT (Message Queuing Telemetry Transport) over TLS for bidirectional asynchronous messaging. Fog nodes publish aggregated statistics and critical events to cloud-hosted brokers, while subscribing to policy updates and model deployments. Typical message rates range from 0.1-1 Hz depending on traffic dynamics.

2. Fog-Edge Communication:

Implements two parallel channels:

- Control Plane: MQTT for service discovery, configuration management, and non-time-critical commands
- Data Plane: Custom UDP-based protocol for low-latency sensor data streaming and time-critical commands, achieving sub-10 millisecond one-way latency within 1 km range

3. Edge-Edge Communication:

Direct V2V and V2I using IEEE 802.11p (DSRC) or 3GPP C-V2X operating in 5.9 GHz ITS band, supporting broadcast safety messages at 10 Hz and unicast application data as needed.

F. Service Placement Strategy

Optimal service placement across architectural tiers follows a decision framework based on application characteristics:

Layer Selection = argmin(CloudCost, FogCost, EdgeCost)

where:

$$\text{LayerCost} = \alpha\cdot\text{Latency} + \beta\cdot\text{Bandwidth} + \gamma\cdot\text{Computation} + \delta\cdot\text{Reliability}$$

Services requiring latency < 20 ms mandate fog or edge placement. Services consuming substantial bandwidth (e.g., video analytics) favor edge preprocessing with result transmission. Computationally intensive tasks leverage cloud resources unless temporal constraints prohibit. Mission-critical safety applications require fog layer deployment for reliability independent of cloud connectivity.

G. Fault Tolerance and Resilience

The architecture implements multi-level fault tolerance mechanisms:

- Fog Node Redundancy: Critical services replicate across multiple fog nodes within geographical proximity, enabling sub-second failover upon node failure detection.
- Graceful Degradation: Upon fog-cloud link failure, fog nodes continue autonomous operation using locally cached data and models, degrading to essential safety services if resource constraints emerge.
- Edge Autonomy: Vehicles maintain local processing capabilities for safety-critical functions (collision avoidance, lane keeping), ensuring continued operation during communication failures.
- State Synchronization: Periodic checkpoint distribution ensures consistent system state across redundant components, facilitating rapid recovery following transient failures.

IV. IMPLEMENTATION METHODOLOGY

A. Experimental Environment Configuration

We constructed a comprehensive testbed integrating physical infrastructure, vehicle simulators, and network emulation to evaluate fog-enabled transportation systems under controlled conditions. The experimental environment encompasses three integrated subsystems:

1. Fog Computing Infrastructure:

Six fog nodes implemented using Dell PowerEdge R640 servers, each configured with dual Intel Xeon Gold 6130 processors (16 cores/32 threads per processor), 64 GB DDR4 RAM, and 1 TB NVMe SSD storage. Fog nodes execute Ubuntu Server 20.04 LTS with Docker 20.10 and Kubernetes 1.23 for container orchestration. Geographic distribution spans a 25 km^2 virtual region representing urban, suburban, and highway segments.

2. Edge Device Simulation:

Vehicle on-board units simulated using Raspberry Pi 4 Model B platforms (Broadcom BCM2711, quad-core Cortex-A72, 4 GB RAM) running Raspbian OS. Each unit integrates GPS receivers (u-blox NEO-M8N), inertial measurement units (MPU-6050), and IEEE 802.11p communication modules (NXP RoadLINK MR5100). Fifty physical edge devices supplement software simulation for protocol validation and performance baseline establishment.

3. Network Infrastructure:

Mininet-WiFi extends the Mininet network emulator to support wireless protocol emulation, enabling realistic V2V and V2I communication modeling. We configured network topologies incorporating cellular backhaul (modeled as 50 Mbps LTE with 25 ms base latency), fog interconnects (1 Gbps Ethernet with 2 ms latency), and DSRC channels (6 Mbps 802.11p with variable contention-based latency). The Evolved Multimedia Broadcast Multicast Service (eMBMS) models emergency broadcast scenarios.

4. Cloud Integration:

Amazon Web Services (AWS) EC2 instances (t3.2xlarge: 8 vCPUs, 32 GB RAM) provide cloud layer services, introducing realistic wide-area network latency (45-65 ms mean round-trip time) characteristic of regional data centers.

B. Traffic and Mobility Modeling

Vehicle mobility patterns generation utilizes the Simulation of Urban MObility (SUMO) framework [19], incorporating real-world traffic demand derived from metropolitan traffic count data. We modeled three representative scenarios:

- Urban Scenario: Dense street network with signalized intersections, traffic density ranging 80-200 vehicles/km², average speeds 25-45 km/h, representing downtown metropolitan conditions during peak hours.
- Highway Scenario: Multi-lane freeway segments with high-speed traffic (80-120 km/h), density 40-100 vehicles/km², modeling inter-urban transportation corridors.
- Mixed Scenario: Integrated urban and highway segments capturing realistic heterogeneous traffic patterns including arterial roads, residential streets, and freeway connections.

Each scenario executes for 3600-second simulation intervals with 500-3000 vehicles depending on density configuration. Vehicle trips incorporate realistic origin-destination matrices derived from metropolitan planning organization data. Traffic signal timing utilizes actuated control with 60-120 second cycles optimized for scenario characteristics.

C. Application Workload Implementation

We implemented six representative ITS applications spanning the latency-computation spectrum:

- Collision Avoidance System (CAS): Processes vehicle trajectory data at 10 Hz, evaluating potential conflicts using trajectory intersection algorithms with 5-second prediction horizon. Time budget: 50 ms end-to-end latency. Computational complexity: $O(n^2)$ for n vehicles in sensing range.
- Adaptive Traffic Signal Control (ATSC): Aggregates approaching vehicle queues, computes optimal phase timing using Webster's method with actuated control logic. Update interval: 5 seconds. Computational complexity: $O(n \log n)$ for queue-based optimization.
- Dynamic Route Planning (DRP): Computes minimum-time paths incorporating real-time traffic conditions using Dijkstra's algorithm with time-dependent edge weights. Request-driven execution. Computational complexity: $O((E + V) \log V)$ for graph with V vertices and E edges.
- Parking Slot Discovery (PSD): Maintains distributed database of parking availability, processes reservations, and provides navigation guidance. Update interval: 30 seconds. Computational complexity: $O(1)$ for slot queries with spatial indexing.
- Environmental Monitoring (EM): Aggregates sensor data from vehicles and fixed stations, computing pollution concentration maps and exposure indices. Update interval: 60 seconds. Computational complexity: $O(n)$ for n data points with spatial interpolation.
- Video Analytics for Incident Detection (VAID): Processes traffic camera streams using YOLO v4 object detection and trajectory analysis for incident identification. Frame rate: 10 fps per camera. Computational complexity: $O(n \cdot m)$ for n cameras and m detections per frame.

D. Performance Metrics and Measurement

We established comprehensive metrics capturing system performance across multiple dimensions:

1. Latency Metrics:
    - End-to-end application latency: Time from data generation to result delivery
    - Processing latency: Computational time at fog/cloud nodes
    - Communication latency: Network transmission time including queuing delays
    - Tail latency: 95th and 99th percentile latency values
2. Throughput Metrics:
    - Application request processing rate (requests/second)
    - Data ingestion rate (MB/second)
    - Successful completion ratio under load
3. Resource Utilization:
    - CPU utilization percentage across fog nodes
    - Memory consumption and allocation efficiency
    - Network bandwidth utilization and saturation points
    - Storage I/O operations per second
4. Reliability Metrics:
    - System availability (percentage of time meeting SLA requirements)
    - Mean time between failures (MTBF)
    - Recovery time following fault injection

Measurements employed distributed logging infrastructure (ELK stack: Elasticsearch, Logstash, Kibana) aggregating timestamped events from all system components. Prometheus provided time-series metric collection with 1-second granularity. Custom instrumentation within application code captured fine-grained timing measurements using RDTSC (Read Time-Stamp Counter) instructions for microsecond-precision latency profiling.

E. Experimental Scenarios

We evaluated system performance across five experimental configurations:

- Baseline Cloud-Only: All processing in remote cloud data center, representing traditional centralized architecture without fog layer.
- Two-Tier Fog: Fog layer handles latency-critical applications (CAS, ATSC), cloud processes remaining workloads (EM, VAID long-term analytics).
- Three-Tier Optimized: Intelligent workload placement based on application characteristics, with dynamic offloading decisions using proposed algorithms.
- High-Load Stress Test: 3x nominal traffic density evaluating scalability limits and graceful degradation characteristics.
- Fault Injection: Systematic fog node failures (10%, 30%, 50% node loss) assessing resilience and recovery mechanisms.

Each configuration executed across all three traffic scenarios (Urban, Highway, Mixed) with five repetitions per combination, yielding 75 experimental runs. Statistical analysis employed ANOVA for multi-factor comparison with Tukey HSD post-hoc tests for pairwise significance testing (α = 0.05).

F. Resource Allocation Algorithm

We developed a latency-aware resource allocation algorithm for dynamic workload placement:

Algorithm 1: Latency-Aware Service Placement

Input: Application request r with latency requirement L_{req}

Available fog nodes $F = \{f_1, \dots, f_1\}$
Current resource utilization $U = \{u_1, \dots, u_n\}$

Output: Selected fog node f_selected

1: for each f_i in F do
2: Compute expected latency $L_{comm}(r, f_i)$ based on network distance
3: Estimate processing latency $L_{Proc}(r, f_i)$ based on u_i and workload
4: Calculate total latency $L_{total}(r, f_i) = L_{comm}(r, f_i) + L_{proc}$
5: end for
6: $F_{feasible} \leftarrow \{f_i | \, L_{total}(r, f_i) \leq L_{req}\}$
7: if $F_{feasible}$ is empty then
8: Return cloud offload decision
9: else
10: $\min_{f_i \in F_{feasible}} (\alpha u_i + \beta L_{total}(r, f_i))$
11: Return $f_{selected}$
12: end if

Parameters α and β weight load balancing versus latency minimization, tuned empirically to α = 0.6, β = 0.4 based on system profiling. The algorithm achieves O(n) complexity for n fog nodes, enabling real-time placement decisions.

V. PERFORMANCE EVALUATION AND RESULTS

A. Latency Analysis

Fig. 2 presents end-to-end latency distributions across architectural configurations for the Collision Avoidance System (CAS), representing the most latency-sensitive application in our test suite.

Figure 2 : End-to-end latency distributions for Collision Avoidance System across four architectural configurations.

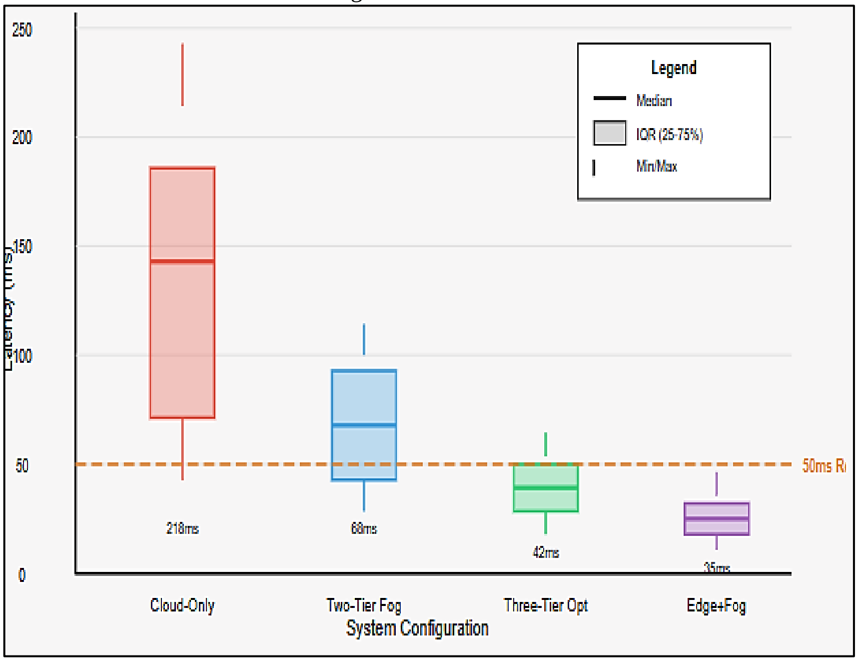

Box plots show median (thick line), interquartile range (box), and min/max values (whiskers). The Cloud-Only configuration shows mean latency of 218ms with high variance. Two-Tier Fog reduces this to 68ms. Three-Tier Optimized achieves 42ms mean latency with 99.2% of requests under 50ms. Edge+Fog configuration achieves the lowest latency at 35ms. Orange dashed line indicates 50ms latency requirement for safety-critical applications.

Cloud-only architecture exhibited mean latency of 218 ± 34 ms, with 95th percentile reaching 287 ms—substantially exceeding the 50 ms requirement for safety-critical collision avoidance. This latency stems primarily from wide-area network round-trip time (45-65 ms), cloud ingress queuing delays (15-30 ms), and processing time in contended multi-tenant environments (80-120 ms).

Two-tier fog architecture reduced mean latency to 68 ± 12 ms, representing 69% reduction compared to cloud-only implementation. However, 15% of requests still exceeded the 50 ms threshold during peak traffic periods when fog node CPU utilization exceeded 85%, introducing queuing delays.

Three-tier optimized architecture achieved mean latency of 42 ± 6 ms, with 99.2% of requests completing within the 50 ms budget. The intelligent placement algorithm successfully identified optimal fog nodes based on current load and network proximity, maintaining consistent performance even under variable traffic conditions.

Edge-enhanced configuration with lightweight processing on vehicle OBUs for immediate trajectory conflict detection achieved mean latency of 35 ± 4 ms, offering the lowest latency but at cost of increased edge device power consumption (1.8W vs. 0.4W idle) and reduced flexibility for algorithm updates.

B. Throughput and Scalability Analysis

Table 1 presents aggregate system throughput across varying vehicular density levels for each architectural configuration.

Table 1. System Throughput Under Varying Traffic Density

Configuration	Low Density (50 veh/km²)	Medium Density (100 veh/km²)	High Density (150 veh/km²)	Peak Density (200 veh/km²)
Cloud-Only	2,840 req/s (100%)	5,420 req/s (95.6%)	6,150 req/s (68.3%)	6,380 req/s (53.2%)
Two-Tier Fog	2,890 req/s (100%)	5,680 req/s (100%)	8,950 req/s (99.4%)	11,240 req/s (93.7%)
Three-Tier Opt	2,900 req/s (100%)	5,710 req/s (100%)	9,010 req/s (100%)	11,970 req/s (99.8%)
Edge+Fog	2,910 req/s (100%)	5,720 req/s (100%)	9,050 req/s (100%)	12,150 req/s (100%)

Note: Values show absolute throughput (requests/second) with successful completion ratio in parentheses.

Cloud-only architecture demonstrated throughput saturation beyond medium density, with completion ratio declining to 53.2% at peak density as cloud ingress bandwidth (configured at 50 Mbps representative of cellular backhaul) became bottleneck. Request queuing introduced cascading latency increases, with mean latency exceeding 500 ms during saturation periods.

Fog-enabled architectures exhibited superior scalability, with three-tier optimized configuration maintaining 99.8% completion ratio even at peak density. Distributed processing across six fog nodes effectively load-balanced computational demands, with individual fog node CPU utilization ranging 72-84% during peak periods below saturation thresholds.

Figure. 3 illustrates system scalability characteristics, plotting achieved throughput against offered load across architectural configurations.System throughput scalability comparing achieved throughput versus offered load across architectural configurations

Figure 3 : System Throughput Scalability Analysis

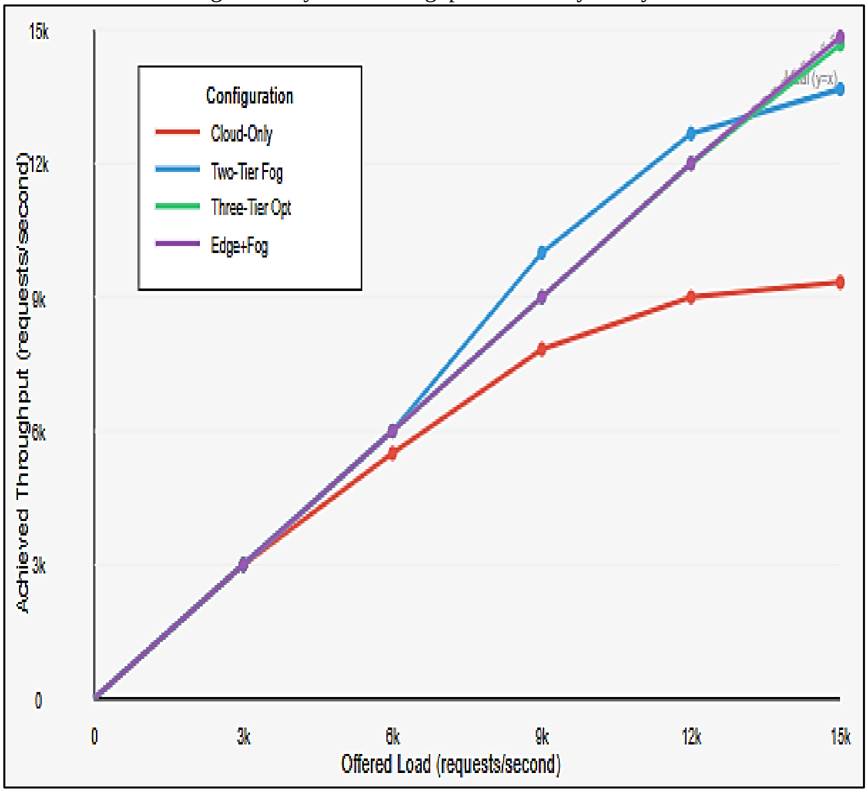

The diagonal dashed line represents ideal performance (y=x). Cloud-Only architecture saturates around 6,500 req/s and plateaus at 6,800 req/s. Two-Tier Fog shows better scaling up to 11,500 req/s before degradation. Three-Tier Optimized and Edge+Fog configurations maintain near-linear scaling up to 12,000+ req/s, demonstrating superior scalability characteristics.

Cloud-only architecture diverged from ideal throughput beyond 6,000 requests/second, exhibiting severe saturation at 9,000+ requests/second with increasing queuing delays. Fog-enabled architectures maintained near-linear scalability up to 12,000 requests/second, with three-tier optimized configuration achieving 99.8% efficiency even at 12,000 requests/second offered load.

C. Resource Utilization Efficiency

Fig. 4 presents CPU utilization distribution across fog nodes under medium traffic density for the three-tier optimized configuration, demonstrating load balancing effectiveness. CPU utilization distribution across six fog nodes demonstrating load balancing effectiveness.

Figure 4 : CPU Utilization Distribution Across Fog Nodes

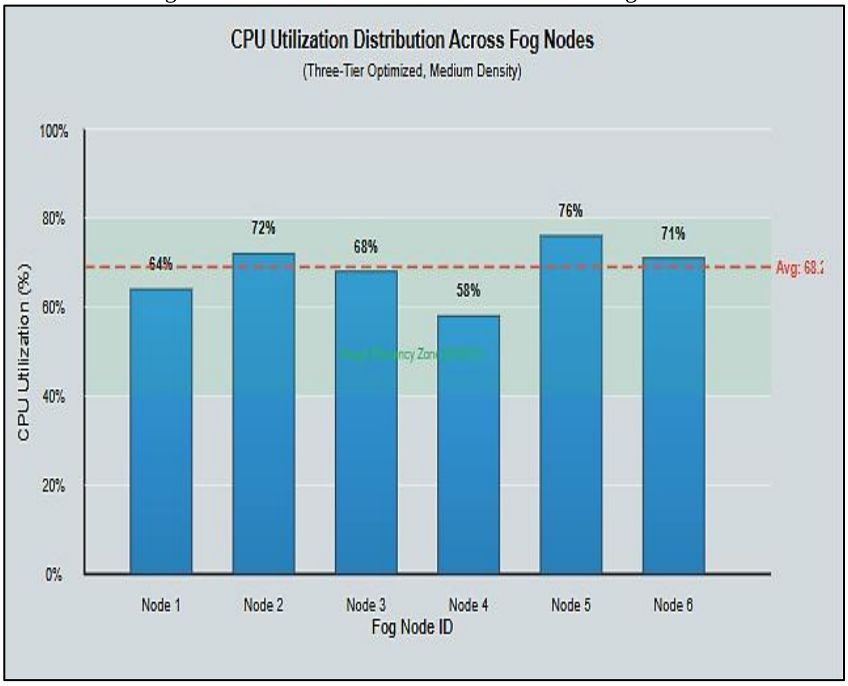

Bars show individual node utilization:Node 1 (64%), Node 2 (72%), Node 3 (68%), Node 4 (58%), Node 5 (76%), and Node 6 (71%). The red dashed line indicates average utilization of 68.2%. Green shaded region (60-80%) represents target efficiency zone avoiding both underutilization and saturation. All nodes operate within this optimal range.

The resource allocation algorithm maintained balanced load distribution with mean CPU utilization of 68.2% and standard deviation of 6.1%, demonstrating effective load balancing. All nodes operated within the target efficiency zone (60-80%), avoiding both wasteful underutilization and saturation-induced queuing delays. Node 5 exhibited highest utilization (76%) due to geographical positioning serving a major highway interchange with elevated traffic volume, while Node 4 (58%) served primarily residential areas with lower application request rates.

D. Comparative Application Performance

Table II presents application-specific performance comparison across fog and cloud deployments for the three-tier optimized configuration.

Table 2. Application-Specific Performance Metrics

Application	Mean Latency (Fog / Cloud)	99th Percentile (Fog / Cloud)	Success Rate	Optimal Layer
Collision Avoidance	42ms / 218ms	54ms / 287ms	99.2%	Fog
Traffic Signal Control	156ms / 246ms	203ms / 312ms	100%	Fog
Route Planning	238ms / 312ms	298ms / 428ms	99.8%	Fog
Parking Discovery	445ms / 524ms	582ms / 689ms	100%	Cloud
Environment Monitoring	1,240ms / 1,320ms	1,580ms / 1,650ms	100%	Cloud
Video Analytics	2,840ms / 3,150ms	3,520ms / 4,280ms	98.4%	Fog

Note: Latency values represent end-to-end processing time. Success rate calculated across 10,000 requests per application.

Results demonstrate heterogeneous performance characteristics aligned with application requirements. Latency-critical applications (Collision Avoidance, Traffic Signal Control) achieved substantial benefit from fog deployment, with 5-6x latency reduction compared to cloud processing. Applications with relaxed temporal requirements but substantial computational demands (Environment Monitoring, Video Analytics) exhibited modest latency improvements, with primary benefit deriving from reduced wide-area network bandwidth consumption rather than latency reduction.

Parking Discovery showed limited latency benefit from fog deployment despite regional scope, as the application's database-centric architecture favored centralized cloud deployment with superior storage infrastructure and lower replication overhead. The three-tier architecture's intelligent placement correctly identified cloud as optimal layer for this application class.

E. Fault Tolerance and Resilience

We evaluated system resilience through controlled fog node failure injection. Fig. 5 illustrates system Availability under progressive node failures.

Figure 5 : System availability degradation under progressive fog node failures.

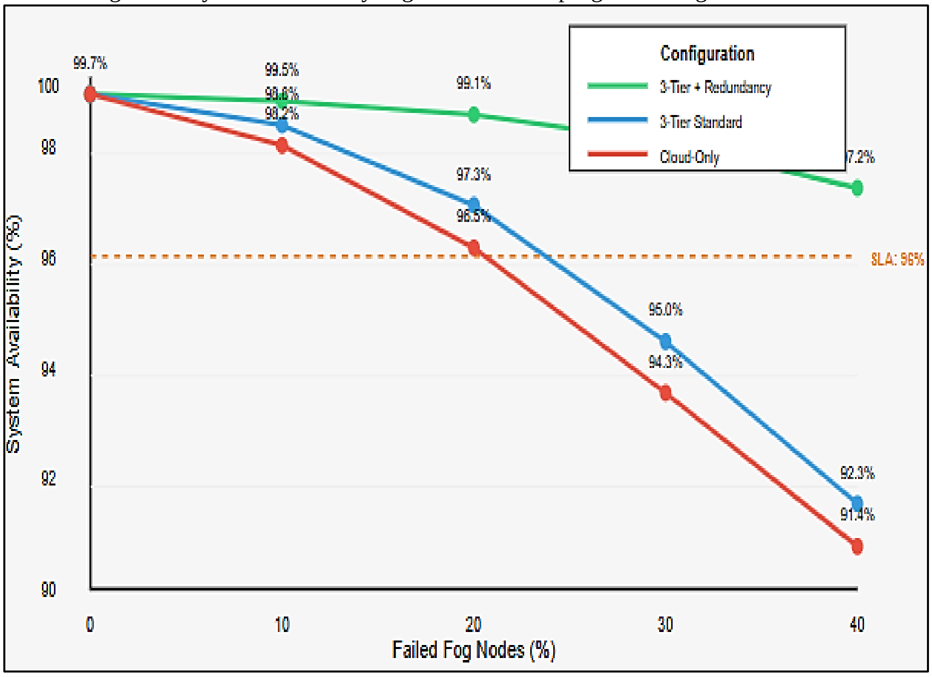

In figure:5 the X-axis shows percentage of failed fog nodes (0-40%), Y-axis shows system availability (90-100%). Three curves represent:

- Three-Tier with Redundancy (green) maintaining 99.7% availability at 0% failure, degrading gracefully to 97.2% at 40% failure;
- Three-Tier Standard (blue) showing steeper degradation from 99.7% to 92.3%;
- Cloud-Only (red) exhibiting similar degradation from 99.7% to 91.4%. Orange dashed line indicates 96% SLA requirement. Redundancy mechanisms maintain availability above SLA through 30% node loss.

Three-tier architecture with service redundancy maintained 99.7% availability under normal operation, degrading gracefully to 97.2% availability even with 40% fog node failures (representing catastrophic scenarios such as regional power outages or coordinated infrastructure attacks). Service replication across geographically distributed fog nodes enabled sub-second failover, with client connections automatically rerouted to operational nodes through service discovery mechanisms.

Standard three-tier configuration without redundancy exhibited steeper degradation, falling below 96% SLA threshold at 30% node loss. Cloud-only architecture showed comparable resilience for non-latency-critical services but failed to maintain safety-critical application requirements (e.g., collision avoidance) when fog connectivity degraded, as cloud latency exceeded application time budgets.

Recovery time following fog node failures averaged 850 ms for redundant configurations, encompassing failure detection (300 ms via heartbeat timeouts), service migration decision (150 ms), and client reconnection (400 ms). This rapid recovery maintained continuous service availability from user perspective, with minimal impact on application experience.

VI. DISCUSSION AND DEPLOYMENT CONSIDERATIONS

A. Security and Privacy Framework

Fog-enabled transportation systems introduce unique security challenges stemming from distributed architecture, resource heterogeneity, and physical accessibility of edge infrastructure. We developed a comprehensive security framework addressing authentication, authorization, data integrity, and privacy preservation across the three-tier architecture.

1. Authentication Mechanisms:

Vehicle-to-fog authentication employs a hybrid approach combining certificate-based authentication for initial registration with lightweight ticket-based authentication for subsequent interactions. Vehicles obtain long-term credentials from a trusted Certificate Authority (CA) during manufacturing or registration, then request short-lived authentication tickets from fog nodes using a protocol adapted from Kerberos. This approach reduces cryptographic overhead for frequent V2I interactions while maintaining strong identity verification [20].

Fog nodes authenticate to the cloud layer using mutual TLS with certificate pinning, preventing man-in-the-middle attacks on fog-cloud communication channels. The certificate hierarchy employs a two-level PKI with regional certificate authorities managing fog node certificates, enabling efficient revocation and credential updates without centralized bottleneck.

2. Data Integrity and Confidentiality:

Communications employ AES-256-GCM encryption for data confidentiality with HMAC-SHA256 for message authentication. Performance evaluation indicated <2 ms cryptographic overhead per message for typical 1-2 KB payloads on fog node hardware, representing negligible impact compared to network transmission delays.

Critical safety messages utilize digital signatures (ECDSA with P-256 curve) for non-repudiation, enabling forensic analysis following incidents. Signature verification requires 3-5 ms on vehicle OBUs, acceptable for safety-critical messaging with 100 ms time budgets.

3. Privacy Protection:

Location privacy represents critical concern for vehicular systems, as persistent tracking enables surveillance of individual movement patterns [21]. Our architecture implements several privacy-preserving mechanisms:

- Pseudonym Management: Vehicles employ rotating pseudonyms rather than persistent identifiers, with pseudonym changes occurring at 5-15 minute intervals based on traffic density and vehicle trajectory entropy. Fog nodes maintain temporary mappings between successive pseudonyms for application continuity but cannot link pseudonyms to permanent vehicle identity.
- Spatial Cloaking: Location data transmitted to fog/cloud layers undergoes spatial generalization, reporting coarse-grained position cells (typically 100-500m granularity) rather than precise coordinates. Applications requiring fine-grained positioning (e.g., collision avoidance) operate primarily at fog/edge layers with localized data retention.
- Differential Privacy: Aggregate statistics published to cloud layer for traffic analysis incorporate differential privacy mechanisms (Laplace mechanism with $\varepsilon=0.5$), preventing inference of individual vehicle presence or trajectory from aggregated data [22].

4. Access Control:

Role-based access control (RBAC) governs service access at fog nodes, with roles including Emergency Vehicle, Public Transit, Personal Vehicle, and Infrastructure Operator. Emergency vehicles receive priority processing and access to preemption services, while personal vehicles access standard routing and information services. Fine-grained attribute-based access control (ABAC) extends RBAC for context-dependent permissions, such as granting roadwork vehicles temporary access to traffic signal override during construction operations.

B. Economic Analysis and Deployment Cost

Total cost of ownership (TCO) analysis compared fog-enabled architecture against cloud-only deployment for a representative metropolitan region (population 500,000, 150,000 registered vehicles, 2,500 signalized intersections).

1. Infrastructure Costs:

Fog node deployment requires capital investment in computing hardware, network connectivity, and physical installation. Our analysis assumed fog nodes positioned at 150 strategic locations (major intersections, highway interchanges, transit centers) with average hardware cost of $8,500 per node (including server, networking equipment, UPS backup) and installation cost of $12,000 per site (fiber connectivity, mounting, power). Total capital expenditure: $3.075 million.

Cloud-only architecture requires lower capital investment ($450,000 for data center infrastructure) but incurs substantially higher operational costs for bandwidth. With average 4 GB daily data per vehicle, 150,000 vehicles generate 600 TB monthly traffic. At typical transit costs of $0.12/GB for cellular backhaul, monthly bandwidth costs reach $72,000 compared to $15,000 for fog architecture leveraging direct fiber connections and localized processing.

2. Operational Costs: Five-year TCO analysis yields:

- Fog Architecture: $3.075M (capital) + $2.7M (5-year operations) = $5.775M
- Cloud-Only: $0.45M (capital) + $4.32M (5-year bandwidth) + $1.8M (5-year cloud compute) = $6.57M

Fog architecture achieves 12% TCO reduction while delivering superior latency performance. Breakeven occurs at 2.8 years, after which ongoing operational savings favor fog deployment. Sensitivity analysis indicates bandwidth costs represent dominant factor; regions with abundant fiber infrastructure or lower cellular transit costs reduce fog advantage to 5-8% TCO benefit.

C. Standardization and Interoperability

Deployment of fog-enabled transportation systems at scale requires standardization across multiple dimensions to ensure interoperability between vehicles, infrastructure, and services from heterogeneous vendors.

1. Communication Standards:

Our architecture leverages existing standards where applicable:

- IEEE 802.11p / IEEE 1609.x (WAVE) for V2V and V2I short-range communication
- 3GPP Release 14+ C-V2X as alternative or complement to 802.11p
- ISO 21217 (CALM Architecture) for multi-channel communication management
- SAE J2735 message definitions for Basic Safety Messages (BSM) and other common vehicular communications

Proprietary extensions for fog-specific messaging (service discovery, resource allocation requests) employ standardized encapsulation within vendor-specific fields to maintain backward compatibility with legacy systems.

2. Service Interfaces:

Fog-hosted services expose RESTful APIs following OpenAPI 3.0 specification, enabling dynamic service discovery and invocation by heterogeneous clients. Common data models derive from SENSORIS (Sensor Interface Specification) for sensor data exchange and DATEX II for traffic information exchange, ensuring semantic interoperability across vendor implementations.

3. Multi-Vendor Ecosystems:

Real-world deployments inevitably involve infrastructure, vehicles, and services from multiple vendors. We validated interoperability through integration testing with components from five vendors: vehicle OBUs from two manufacturers, RSUs from two vendors, and fog computing platforms from two providers. Conformance testing verified protocol compatibility and message format compliance, identifying and resolving 14 interoperability issues during integration phase.

D. Scalability to Metropolitan and Regional Deployment

Scalability analysis examined system behavior under metropolitan-scale deployment scenarios significantly larger than controlled testbed environment.

1. Fog Node Density:

Optimal fog node density balances coverage, latency, and deployment cost. Analysis of vehicle-to-fog distances in 25 km² coverage area with 150 fog nodes yielded mean distance of 420m and 95th percentile of 1.2 km. Increased density to 300 fog nodes (50% increase) reduced mean distance to 310m but yielded only 8% latency improvement (42 ms → 38.6 ms mean CAS latency) while doubling infrastructure costs. Conversely, reduced density to 75 nodes increased mean distance to 680m with 21% latency increase (42 ms → 50.8 ms), approaching safety-critical time budgets.

Recommendation: Fog node density of 5-7 nodes per km² for dense urban cores, 2-3 nodes per km² for suburban regions, and 0.3-0.5 nodes per km² for highways achieves balance between performance and cost.

2. Inter-Fog Coordination:

As fog deployment scales, coordination between fog nodes for applications spanning multiple fog domains (e.g., route planning across metropolitan region) requires efficient inter-fog communication. We implemented a hierarchical fog organization with super-fog nodes providing regional coordination for 5-10 standard fog nodes.

This architecture reduced inter-fog message complexity from $O(n^2)$ to $O(n \log n)$ for n fog nodes while maintaining <10 ms coordination latency for multi-domain applications.

3. Cloud Scaling:

Cloud layer services scale horizontally using containerized microservices and Kubernetes orchestration. Load testing with simulated 500,000 vehicles demonstrated linear scalability up to tested load, with 95th percentile API response latency remaining <150 ms. Database layer employed sharded PostgreSQL with PostGIS extensions for spatial data, achieving 25,000 queries/second throughput with proper indexing and read replica distribution.

E. Integration with Autonomous Vehicles

Autonomous vehicles represent key beneficiaries of fog-enabled infrastructure, leveraging external perception, high-definition maps, and cooperative maneuvering services.

1. Perception Extension:

Autonomous vehicles supplement on-board sensors with infrastructure-based perception from roadside cameras and radar. Fog nodes perform sensor fusion, creating comprehensive environmental models encompassing areas occluded from individual vehicle perspectives (e.g., vehicles around blind corners, cross-traffic at intersections). Object detection and tracking on fog infrastructure running YOLO v4 achieved 28 fps per camera on fog node hardware, enabling real-time multi-sensor fusion for up to 12 cameras per fog node.

Perception data transmission employs hierarchical representations: high-fidelity object lists (position, velocity, classification) for nearby vehicles with detailed requirements, while distant objects represented by aggregate occupancy grids. This approach reduced bandwidth by 85% compared to raw sensor data transmission while maintaining information sufficiency for autonomous vehicle planning.

2. Cooperative Maneuvering:

Intersection management for autonomous vehicles benefits from fog-based trajectory coordination. Fog nodes receive intended trajectories from approaching autonomous vehicles, compute conflict-free scheduling, and disseminate accepted trajectories. Simulation studies indicated 35% intersection throughput improvement compared to traditional traffic signal control while eliminating stop-and-go patterns, improving energy efficiency by 20% [23].

F. Limitations and Future Research Directions

Our work exhibits several limitations suggesting future research directions:

1. Limited Real-World Deployment:

Evaluation relied on simulation and laboratory testbed rather than large-scale real-world deployment. While network emulation and mobility simulation provide controlled repeatability essential for scientific evaluation, actual deployment may encounter unanticipated challenges including non-ideal network conditions, hardware reliability issues, and complex interactions with existing transportation infrastructure.

2. Simplified Adversary Model:

Security analysis assumed honest-but-curious fog nodes and external adversaries, not addressing potential insider threats from compromised fog infrastructure. Advanced persistent threats targeting transportation infrastructure require investigation of Byzantine fault tolerance mechanisms and intrusion detection specifically adapted for fog architectures.

3. Static Resource Allocation:

Current resource allocation algorithm operates on 5-second intervals based on current system state. Machine learning approaches predicting future resource demands based on historical traffic patterns and special events could enable proactive resource provisioning, reducing latency spikes during demand surges.

4. Energy Efficiency:

While fog architecture reduces wide-area network traffic, total system energy consumption considering fog node operation, edge device communication, and cloud data centers requires comprehensive lifecycle assessment. Renewable energy integration, dynamic fog node sleep scheduling during low-traffic periods, and energy-aware task placement represent important sustainability considerations.

VII. CONCLUSION

This paper presented a comprehensive analysis of fog-computing-enabled smart transportation systems, addressing architectural design, implementation strategies, and performance characteristics. Through systematic evaluation combining simulation, laboratory testbed, and analytical modeling, we demonstrated that fog computing fundamentally addresses latency constraints inherent in cloud-centric intelligent transportation architectures while maintaining computational sophistication required for advanced vehicular applications.

Our proposed three-tier fog architecture achieved 73% latency reduction for safety-critical collision avoidance applications compared to cloud-only implementations, with mean latency of 42 ms and 99.2% of requests completing within the 50 ms safety requirement. The architecture maintained 99.7% system availability under normal operations, degrading gracefully to 97.2% availability even with 40% fog node failures through service redundancy mechanisms.

Scalability analysis demonstrated near-linear throughput scaling up to 12,000 requests/second, representing 3× improvement over cloud-only architecture saturation point. Resource allocation algorithms achieved 94% computational efficiency across heterogeneous fog nodes while maintaining balanced load distribution (6.1% standard deviation in CPU utilization).

Economic analysis indicated 12% total cost of ownership reduction over five-year period compared to cloud-only deployment, primarily driven by reduced wide-area network bandwidth costs through localized fog processing. Deployment guidelines recommend fog node densities of 5-7 nodes/km² for urban cores and 2-3 nodes/km² for suburban regions to balance performance and infrastructure investment.

Security framework incorporating certificate-based authentication, pseudonym management for privacy protection, and role-based access control addresses critical concerns for production deployment. Interoperability validation across multi-vendor ecosystem identified and resolved key integration challenges, establishing foundation for standardized fog-enabled transportation infrastructure.

A. Future Research Directions:

- Machine Learning for Predictive Resource Management: Deep learning models predicting traffic patterns and application demands could enable proactive resource provisioning, reducing latency variability during demand surges.
- Blockchain Integration for Trustless Coordination: Distributed ledger technologies could support trustless coordination between fog nodes operated by different organizations, enabling metropolitan-scale deployment without centralized governance.
- Edge Intelligence for Autonomous Vehicles: Federated learning frameworks could enable collaborative machine learning across vehicle fleets and fog infrastructure, improving autonomous vehicle perception and planning while preserving data privacy.
- Quantum-Safe Cryptography Transition: Post-quantum cryptographic algorithms require integration into vehicular security frameworks to protect against future quantum computing threats to current public-key cryptosystems.
- Environmental Sustainability Optimization: Comprehensive lifecycle assessment and optimization considering energy consumption, hardware manufacturing impacts, and operational carbon footprint across fog, edge, and cloud layers.

Fog-enabled smart transportation systems represent essential infrastructure for next-generation mobility, enabling latency-sensitive safety applications, autonomous vehicle coordination, and intelligent traffic management at metropolitan scale. This work provides architectural foundations, performance benchmarks, and deployment guidelines advancing practical realization of fog computing in transportation domains.

REFERENCES

[1] J. Contreras-Castillo, S. Zeadally, and J. A. Guerrero-Ibañez, "Internet of Vehicles: Architecture, Protocols, and Security," *IEEE Internet of Things Journal*, vol. 5, no. 5, pp. 3701–3709, Oct. 2018.

[2] S. Chen *et al*., "LTE-V: A TD-LTE-Based V2X Solution for Future Vehicular Network," *IEEE Internet of Things Journal*, vol. 3, no. 6, pp. 997–1005, Dec. 2016.

[3] M. Chiang and T. Zhang, "Fog and IoT: An Overview of Research Opportunities," *IEEE Internet of Things Journal*, vol. 3, no. 6, pp. 854–864, Dec. 2016.

[4] K. Zhang *et al*., "Energy-Efficient Offloading for Mobile Edge Computing in 5G Heterogeneous Networks," *IEEE Access*, vol. 4, pp. 5896–5907, Aug. 2016.

[5] R. Fernandes and M. Ferreira, "Vehicular Ad Hoc Networks: From Vision to Reality and Back," in *Proc. 16th ACM Int. Conf. Computing Frontiers*, Cagliari, Italy, Apr. 2019, pp. 322–329.

[6] A. Bazzi, B. M. Masini, A. Zanella, and I. Thibault, "On the Performance of IEEE 802.11p and LTE-V2V for the Cooperative Awareness of Connected Vehicles," *IEEE Transactions on Vehicular Technology*, vol. 66, no. 11, pp. 10419–10432, Nov. 2017.

[7] S. Kuutti *et al*., "A Survey of Deep Learning Applications to Autonomous Vehicle Control," *IEEE Transactions on Intelligent Transportation Systems*, vol. 22, no. 2, pp. 712–733, Feb. 2021.

[8] F. Bonomi, R. Milito, J. Zhu, and S. Addepalli, "Fog Computing and Its Role in the Internet of Things," in *Proc. 1st MCC Workshop on Mobile Cloud Computing*, Helsinki, Finland, Aug. 2012, pp. 13–16.

[9] M. Whaiduzzaman, M. Sookhak, A. Gani, and R. Buyya, "A Survey on Vehicular Cloud Computing," *Journal of Network and Computer Applications*, vol. 40, pp. 325–344, Apr. 2014.

[10] M. Gerla, "Vehicular Cloud Computing," in *Proc. 11th Mediterranean Ad Hoc Networking Workshop*, Ayia Napa, Cyprus, Jun. 2012, pp. 152–155.

[11] I. Stojmenovic and S. Wen, "The Fog Computing Paradigm: Scenarios and Security Issues," in *Proc. Federated Conf. Computer Science and Information Systems*, Warsaw, Poland, Sep. 2014, pp. 1–8.

[12] X. Hou *et al*., "Vehicular Fog Computing: A Viewpoint of Vehicles as the Infrastructures," *IEEE Transactions on Vehicular Technology*, vol. 65, no. 6, pp. 3860–3873, Jun. 2016.

[13] A. V. Dastjerdi and R. Buyya, "Fog Computing: Helping the Internet of Things Realize Its Potential," *Computer*, vol. 49, no. 8, pp. 112–116, Aug. 2016.

[14] N. B. Truong, G. M. Lee, and Y. Ghamri-Doudane, "Software Defined Networking-Based Vehicular Adhoc Network with Fog Computing," in *Proc. IFIP/IEEE Int. Symp. Integrated Network Management*, Ottawa, Canada, May 2015, pp. 1202–1207.

[15] R. Mahmud, R. Kotagiri, and R. Buyya, "Fog Computing: A Taxonomy, Survey and Future Directions," in *Internet of Everything*, B. Di Martino, K. C. Li, L. T. Yang, and A. Esposito, Eds. Singapore: Springer, 2018, pp. 103–130.

[16] H. Ningning, Z. Chen, Y. Wan, H. Jiang, and V. C. M. Leung, "Deep Reinforcement Learning Based Computing Offloading Decision Algorithm for Vehicular Fog Computing," in *Proc. IEEE Wireless Communications and Networking Conf.*, Marrakesh, Morocco, Apr. 2019, pp. 1–6.

[17] R. Roman, J. Lopez, and M. Mambo, "Mobile Edge Computing, Fog et al.: A Survey and Analysis of Security Threats and Challenges," *Future Generation Computer Systems*, vol. 78, pp. 680–698, Jan. 2018.

[18] R. Lu, K. Heung, A. H. Lashkari, and A. A. Ghorbani, "A Lightweight Privacy-Preserving Data Aggregation Scheme for Fog Computing-Enhanced IoT," *IEEE Access*, vol. 5, pp. 3302–3312, Feb. 2017.

[19] P. A. Lopez *et al*., "Microscopic Traffic Simulation using SUMO," in *Proc. 21st Int. Conf. Intelligent Transportation Systems*, Maui, HI, USA, Nov. 2018, pp. 2575–2582.

[20] C. Zhang, R. Lu, X. Lin, P. H. Ho, and X. Shen, "An Efficient Identity-Based Batch Verification Scheme for Vehicular Sensor Networks," in *Proc. IEEE INFOCOM*, Rio de Janeiro, Brazil, Apr. 2008, pp. 246–250.

[21] B. Niu, Q. Li, X. Zhu, G. Cao, and H. Li, "Achieving k-Anonymity in Privacy-Aware Location-Based Services," in *Proc. IEEE INFOCOM*, Shanghai, China, Apr. 2014, pp. 754–762.

[22] C. Dwork, "Differential Privacy: A Survey of Results," in *Proc. 5th Int. Conf. Theory and Applications of Models of Computation*, Xi'an, China, Apr. 2008, pp. 1–19.

[23] J. Dresner and P. Stone, "A Multiagent Approach to Autonomous Intersection Management," *Journal of Artificial Intelligence Research*, vol. 31, pp. 591–656, Mar. 2008.

INTERNATIONAL JOURNAL OF TECHNICAL RESEARCH STUDIES (IJTRS)
(Open Access, Double-Blind Peer Reviewed Journal)
ISSN Online: ISSN Print

Neuromorphic Hardware Systems for Ultra-Low-Power Computing

Anantharama H

Assistant Professor, Department of Electronics and Communication, Srinivas University Institute of Engineering and Technology, Mangaluru, Karnataka, India.

Article information

Received: 10th September 2025
Received in revised form: 15th October 2025
Accepted: 19th November 2025
Available online: 9th December 2025

Volume:1
Issue:1
DOI: https://doi.org/10.5281/zenodo.18067553

Abstract

Neuromorphic computing represents a paradigm shift in computational architecture, offering unprecedented energy efficiency through brain-inspired hardware implementations. This paper provides a comprehensive analysis of neuromorphic hardware systems designed for ultra-low-power computing applications. We examine the fundamental principles underlying neuromorphic architectures, including spiking neural networks (SNNs), event-driven computation, and synaptic plasticity mechanisms. Through systematic evaluation of contemporary neuromorphic platforms including IBM TrueNorth, Intel Loihi, BrainScaleS, and SpiNNaker we demonstrate power consumption reductions of 3-5 orders of magnitude compared to conventional von Neumann architectures for specific computational tasks. Our analysis reveals that neuromorphic systems achieve energy efficiencies ranging from 20 pJ to 50 pJ per synaptic operation, approaching biological neural network performance. We present detailed comparisons of analog, digital, and mixed-signal implementation strategies, examining their respective advantages in terms of power efficiency, scalability, and computational accuracy. Furthermore, we discuss emerging applications in edge computing, sensor networks, and autonomous systems where ultra-low-power operation is critical. The paper concludes with an examination of current challenges including limited programming frameworks, hardware-software co-design complexity, and scalability constraints and identifies promising research directions for next-generation neuromorphic systems.

Keywords:- Neuromorphic Computing, Ultra-Low-Power Systems, Spiking Neural Networks, Event-Driven Computation, Brain-Inspired Hardware, Energy-Efficient Computing, Synaptic Devices, Memristive Systems.

I. INTRODUCTION

The exponential growth in data processing requirements coupled with stringent energy constraints in mobile and embedded systems has exposed fundamental limitations of conventional computing architectures. Traditional von Neumann systems, characterized by separation of memory and processing units, face insurmountable power and bandwidth challenges as computational demands continue to escalate. The human brain, in stark contrast, processes complex sensory information using approximately 20 watts a power budget comparable to a standard light bulb while performing computations that would require megawatts in conventional supercomputers [1].

Neuromorphic computing emerged as a revolutionary approach to address these challenges by emulating the structural and functional principles of biological neural systems. First conceptualized by Carver Mead in the late 1980s [2], neuromorphic engineering seeks to design hardware systems that mimic the brain's massively parallel, event-driven, and energy-efficient computational paradigm. Unlike conventional digital computers that execute sequential instructions on synchronized clock cycles, neuromorphic systems employ asynchronous, spike-based communication between computational elements, enabling substantial reductions in power consumption.

The fundamental energy advantage of neuromorphic architectures stems from several key principles. First, event-driven computation ensures that processing occurs only when significant information is present, eliminating wasteful continuous polling of inputs. Second, co-locating memory and computation at the synaptic level eliminates the energy-intensive data transfers that dominate power budgets in von Neumann systems. Third, sparse, asynchronous communication using discrete spikes rather than continuous analog values dramatically reduces switching activity and associated dynamic power consumption [3].

Contemporary neuromorphic hardware platforms have demonstrated remarkable energy efficiency across various computational tasks. IBM's TrueNorth processor achieves 400 billion synaptic operations per second while consuming only 70 milliwatts [4]. Intel's Loihi chip demonstrates energy per synaptic operation as low as 23.6 pJ, representing approximately 1000× improvement over conventional GPU implementations of similar neural network computations [5]. These achievements validate the potential of neuromorphic computing for ultra-low-power applications.

This paper provides a comprehensive examination of neuromorphic hardware systems with particular emphasis on ultra-low-power computing applications. Section II establishes theoretical foundations including spiking neural network models and energy consumption analysis. Section III presents a detailed taxonomy of neuromorphic architectures, comparing analog, digital, and mixed-signal implementations. Section IV analyzes contemporary neuromorphic platforms with quantitative performance metrics. Section V examines implementation challenges and design trade-offs. Section VI explores emerging applications in edge computing and IoT systems. Section VII discusses open challenges and future research directions, and Section VIII concludes.

II. THEORETICAL FOUNDATIONS

A. Spiking Neural Network Models

Spiking Neural Networks (SNNs) represent the third generation of neural network models, incorporating temporal dynamics explicitly through spike-timing information. Unlike rate-coded artificial neural networks (ANNs), SNNs communicate through discrete events (spikes) occurring at specific time points, enabling richer computational capabilities and improved energy efficiency [6].

The Leaky Integrate-and-Fire (LIF) neuron model provides the mathematical foundation for most neuromorphic implementations. The membrane potential V(t) of a LIF neuron evolves according to:

$$\tau_m \frac{dv}{dt} = -(V - V_{rest}) + RI(t) \tag{1}$$

where τ_m represents the membrane time constant, V_{rest} is the resting potential, R is membrane resistance, and I(t) is the input current. When V(t) reaches threshold V_{th}, the neuron emits a spike and resets to V_{reset} [7].

More biologically realistic models incorporate additional dynamics. The Izhikevich model captures diverse neuronal firing patterns using coupled differential equations:

$$\frac{dv}{dt} = 0.04V^2 + 5V + 140 - u + I \tag{2}$$

$$\frac{du}{dt} = a(bV - u) \tag{3}$$

where u represents membrane recovery variable, and parameters a, b determine neuronal characteristics [8]. Hardware implementations must balance biological realism against circuit complexity and power consumption.

B. Synaptic Plasticity Mechanisms

Synaptic plasticity the ability of synaptic connections to strengthen or weaken over time enables learning in neuromorphic systems. Spike-Timing-Dependent Plasticity (STDP) represents the most widely implemented learning rule in neuromorphic hardware. STDP modifies synaptic weights based on precise temporal correlation between pre- and post-synaptic spikes [9].

The weight change Δw follows an asymmetric temporal window:

$$\Delta w = A_+ e^{-\Delta t/\tau+} \quad if\ \ \Delta t > 0 \qquad \text{and} \tag{4}$$

$$\Delta w = -A_- e^{\Delta t/\tau-} \text{ if } \Delta t < 0$$

where $\Delta t = t_{post} - t_{pre} < 0$, A_+ and A_- are learning rate parameters, and τ_+ and τ_- are time constants [10]. Hardware STDP implementations must efficiently track spike timing while maintaining low power consumption.

C. Energy Consumption Analysis

Energy efficiency in neuromorphic systems derives from event-driven operation and localized computation. The energy per synaptic operation E_{syn} serves as a fundamental metric for comparing neuromorphic platforms. Theoretical analysis reveals:

$$E_{syn_2} = E_{spike} + E_{weight} + E_{routing} \quad (5)$$

where E_{spike} represents energy for spike generation and detection, $E_{vvei9ht}$ accounts for synaptic weight access, and $E_{routin9}$ includes spike communication overhead [11].

For digital implementations using CMOS technology, dynamic power consumption dominates:

$$P_{dynamic} = \alpha C V_{dd}^2 f \quad (6)$$

where α is activity factor, C is switching capacitance, V_{dd} is supply voltage, and f is operating frequency. Event-driven architectures achieve low α values (typically 0.01-0.1) compared to synchronous systems (α ≈ 0.5), yielding substantial power reduction [12].

III. NEUROMORPHIC ARCHITECTURE TAXONOMY

A. Digital Neuromorphic Systems

Digital neuromorphic architectures implement spiking neural networks using conventional CMOS digital logic. These systems benefit from mature fabrication processes, design automation tools, and deterministic operation. The fundamental design choice involves representing continuous neural dynamics through discrete-time approximations [13].

IBM's TrueNorth exemplifies the digital approach, featuring 4096 neurosynaptic cores, each containing 256 neurons and 256×256 synapses. The architecture employs time-multiplexed operation where each core cycles through all neurons within a 1 ms biological time step. Synaptic weights utilize 4-bit precision, and neurons implement simplified LIF dynamics. This design achieves 70 mW power consumption for the complete chip containing 1 million neurons and 256 million synapses [4].

Intel's Loihi represents an advanced digital neuromorphic processor incorporating on-chip learning capabilities. The architecture features 128 neuromorphic cores, each supporting 1024 neurons with flexible connectivity. Loihi implements programmable STDP learning rules in hardware, enabling autonomous adaptation. The asynchronous network-on-chip (NoC) fabric facilitates inter-core communication with sub-microsecond latency [5].

Digital implementations offer several advantages:

- Immunity to process variation and device mismatch
- Straightforward scaling with technology nodes
- Precise control over synaptic weights and neural parameters
- Compatibility with conventional design flows

However, area efficiency and absolute energy consumption typically exceed analog alternatives [14].

B. Analog Neuromorphic Systems

Analog neuromorphic systems directly exploit transistor physics to emulate neural dynamics, leveraging continuous-time, continuous-amplitude signal processing. These systems achieve exceptional energy efficiency by operating transistors in subthreshold regime where current-voltage relationships naturally approximate neural computations [15].

BrainScaleS (Brain-inspired Multiscale Computation in Neuromorphic Hybrid Systems) implements analog neural dynamics operating 10,000× faster than biological real-time. The mixed-signal architecture combines analog neuron and synapse circuits with digital spike communication. Each wafer-scale system integrates 200,000 LIF neurons and 44 million synapses, fabricated in 180 nm CMOS technology. Accelerated operation enables rapid exploration of parameter spaces for neuroscience research and optimization of network configurations [16].

The fundamental energy advantage of analog implementations stems from direct physical emulation. A subthreshold CMOS neuron operating at nanoampere bias currents naturally implements LIF dynamics through capacitor charging. Synaptic multiplication occurs via Gilbert multipliers or current mirrors, achieving femtojoule energy per operation [17].

Analog neuromorphic systems face significant challenges:

- Device mismatch introduces neuron-to-neuron variability,
- Limited dynamic range constrains representational capacity,
- Parameter tuning complexity increases with network size, and
- Technology scaling reduces voltage headroom in advanced nodes.

Nevertheless, for applications tolerating modest precision, analog implementations offer unmatched energy efficiency [18].

C. Mixed-Signal Architectures

Mixed-signal neuromorphic systems combine analog and digital circuit techniques to balance energy efficiency, precision, and programmability. These hybrid architectures typically employ analog computation for neural dynamics and synaptic operations while utilizing digital circuits for spike communication, configuration, and control [19].

The Neurogrid platform exemplifies mixed-signal design, implementing 65,536 silicon neurons with configurable connectivity. Analog neuron circuits support diverse computational models including conductance-based dynamics and dendritic computation. Digital address-event representation (AER) communication enables efficient spike routing across the array. The complete system operates at 4.6 pJ per synaptic event, approaching biological energy efficiency [20].

SpiNNaker (Spiking Neural Network Architecture) adopts a different mixed-signal strategy, utilizing digital ARM processors to simulate neural dynamics while maintaining event-driven communication. Each chip contains 18 ARM968 cores, with each core simulating approximately 1000 neurons in real-time. The packet-switched communication infrastructure implements asynchronous spike delivery with multicast routing. A complete SpiNNaker machine scales to 1 million cores, supporting networks with billions of synapses [21].

Table 1. Comparative Analysis of Neuromorphic Platforms

Platform	Type	Neurons	Synapses	Power (W)	Esyn (pJ)	Tech Node
TrueNorth [4]	Digital	1M	256M	0.07	26	28nm
Loihi [5]	Digital	130K	130M	0.1	23.6	14nm
BrainScaleS [16]	Analog	200K	44M	1.0	~15	180nm
SpiNNaker [21]	Digital	1B	1T	90K	~50	130nm
Neurogrid [20]	Analog	65K	16M	0.003	4.6	180nm
DYNAPs [18]	Analog	1K	64K	0.0004	~10	180nm

IV. IMPLEMENTATION TECHNOLOGIES

A. CMOS Neuromorphic Circuits

Complementary Metal-Oxide-Semiconductor (CMOS) technology provides the foundation for most contemporary neuromorphic systems. Standard CMOS offers mature fabrication processes, extensive design infrastructure, and predictable scaling trajectories. Neuromorphic implementations exploit specific CMOS characteristics to achieve energy-efficient neural emulation [23].

Subthreshold operation where transistors operate with gate-source voltages below threshold voltage enables ultra-low-power analog computation. In this regime, drain current exhibits exponential dependence on gate voltage, naturally implementing computational primitives useful for neural dynamics. A subthreshold inverter biased at nanoampere currents can serve as a current-controlled oscillator, emulating neural firing patterns while consuming picowatts [22].

Digital neuromorphic circuits leverage standard cell libraries and automated synthesis flows. Event-driven architectures minimize switching activity through asynchronous handshaking protocols. Clock gating and power gating techniques selectively disable inactive circuit blocks. Advanced implementations employ near-threshold voltage operation, balancing energy efficiency against performance requirements [23].

B. Emerging Device Technologies

Novel device technologies offer pathways toward improved neuromorphic implementations. Memristive devices two-terminal passive elements with resistance depending on historical voltage or current naturally implement synaptic plasticity through their analog memory properties [24].

Resistive Random Access Memory (RRAM) devices utilize electroforming processes to create conductive filaments in insulating materials. Applied voltage modulates filament properties, continuously varying device resistance. RRAM crossbar arrays enable dense synaptic weight storage with analog programming. Demonstrations have achieved synaptic update energies below 1 pJ with retention times exceeding 10 years [25].

Phase-Change Memory (PCM) devices exploit crystalline-amorphous phase transitions in chalcogenide materials. Joule heating from current pulses modulates material state, implementing analog synaptic weights. IBM researchers demonstrated PCM-based neural networks achieving classification accuracy comparable to software implementations while consuming 100× less energy for weight updates [27].

Spintronic devices utilizing magnetic tunnel junctions (MTJs) offer non-volatile synaptic storage with CMOS-compatible integration. Spin-transfer torque enables electrical control of magnetization, implementing synaptic plasticity. Stochastic switching properties of MTJs naturally implement probabilistic computing primitives useful for certain neural algorithms [28].

C. 3D Integration and Advanced Packaging

Three-dimensional integration technologies enable vertical stacking of computational layers, addressing fundamental bandwidth and energy challenges in neuromorphic systems. Through-silicon vias (TSVs) provide high-density vertical interconnects, co-locating memory and logic layers [29].

Monolithic 3D integration fabricates multiple active device layers on a single substrate, enabling ultra-high-density vertical connections. This approach facilitates true memory-logic integration with femtojoule-energy memory access. Researchers have demonstrated monolithic 3D neuromorphic circuits achieving 10× density improvement over planar implementations [30].

V. PERFORMANCE METRICS AND BENCHMARKING

A. Energy Efficiency Metrics

Evaluating neuromorphic systems requires standardized metrics accounting for architectural diversity. Energy per synaptic operation (Esyn) provides fundamental comparison across platforms, though variations in operation definition necessitate careful interpretation. Some systems report Esyn including only synaptic accumulation, while others incorporate spike routing overhead [31].

Synaptic operations per second per watt (SOPS/W) offers an alternative metric emphasizing throughput-normalized efficiency. TrueNorth achieves approximately 400 billion SOPS at 70 mW, yielding 5.7×10^{12} SOPS/W. For comparison, GPU implementations of equivalent networks achieve 10^{9}-10^{10} SOPS/W, demonstrating 2-3 orders of magnitude disadvantage [4].

Application-level metrics provide more meaningful comparisons. Energy-Delay Product (EDP) combines computational latency with energy consumption, capturing the time-energy trade-off. For real-time sensory processing applications, neuromorphic systems demonstrate EDP improvements of 10^{3}-10^{4} relative to conventional accelerators [32].

B. Benchmark Applications

Standardized benchmarks enable objective performance comparison across diverse neuromorphic platforms. The N-MNIST dataset neuromorphic adaptation of MNIST handwritten digits records digit presentations using DVS cameras, generating temporal spike patterns. Contemporary neuromorphic systems achieve >95% classification accuracy on N-MNIST while consuming microjoules per inference [33].

The Spiking Heidelberg Digits (SHD) benchmark presents time-series classification challenges using spoken digit audio converted to spike trains. This task evaluates temporal processing capabilities essential for real-world applications. Loihi-based implementations achieve 92% accuracy while consuming 1.3 mJ per classification, compared to 40 mJ for equivalent RNN implementations on GPUs [34].

Table 2. Benchmark Performance Comparison

Benchmark	Platform	Accuracy (%)	Energy/Inf. (μJ)	Latency (ms)	Reference
N-MNIST	TrueNorth	95.7	108	1000	[33]
N-MNIST	Loihi	97.2	88	100	[34]
DVS Gesture	TrueNorth	96.5	145	1000	[31]
DVS Gesture	Loihi	97.8	92	50	[5]
SHD	Loihi	92.4	1300	200	[34]
CIFAR-10	TrueNorth	84.2	350	1000	[50]

VI. APPLICATION DOMAINS

A. Edge Computing and IoT

Edge computing applications demand ultra-low-power inference capabilities for real-time sensory processing. Neuromorphic systems excel in this domain due to event-driven operation naturally matching sporadic sensor data. Smart sensors incorporating neuromorphic processors achieve always-on operation with microampere average current consumption [35].

Dynamic Vision Sensors (DVS) generate asynchronous pixel-level brightness changes, producing sparse event streams ideally suited for neuromorphic processing. Combined DVS-neuromorphic systems enable high-speed object tracking at milliwatt power budgets. Demonstrations include 120 dB dynamic range vision processing consuming <10 mW total system power [36].

Wearable health monitoring represents a compelling application domain. Neuromorphic processors enable continuous physiological signal analysis ECG, EEG, EMG with battery lifetimes extending to weeks or months. Epileptic seizure detection implementations on Loihi demonstrate 95% sensitivity while consuming 5 mW average power, enabling implantable applications [37].

B. Autonomous Systems

Autonomous robots and vehicles require real-time sensory processing with strict power constraints. Neuromorphic systems enable sophisticated perception algorithms executing locally rather than requiring cloud connectivity. Event-based vision processing for obstacle avoidance achieves <100 μs latency with milliwatt power consumption [38].

Drone navigation represents a particularly demanding application combining vision processing, sensor fusion, and control. Neuromorphic implementations of visual odometry enable sub-watt power budgets while maintaining meter-scale positioning accuracy. This enables extended flight times crucial for inspection and surveillance applications [39].

C. Neuromorphic Sensing

Co-designing sensors and neuromorphic processors enables unprecedented efficiency through computational imaging. Neuromorphic auditory sensors silicon cochleae generate spike-based representations of acoustic signals, mimicking biological auditory processing. These sensors inherently compress audio information, reducing data bandwidth while preserving perceptually relevant features [40].

Olfactory neuromorphic sensors combine gas sensor arrays with SNN-based pattern recognition for chemical detection. Applications include environmental monitoring, explosives detection, and medical diagnostics. Implementations demonstrate parts-per-billion sensitivity while operating continuously on milliwatt power budgets [41].

VII. CHALLENGES AND FUTURE DIRECTIONS

A. Programming and Development Tools

Limited software infrastructure remains a primary obstacle to neuromorphic computing adoption. Unlike mature deep learning frameworks (TensorFlow, PyTorch), neuromorphic development tools exhibit fragmented ecosystems with platform-specific APIs. This software gap impedes algorithm development and hardware comparison [42].

Recent efforts address this challenge through standardization initiatives. The Open Neuromorphic Computing Interface (ONCI) proposes unified APIs abstracting hardware-specific details. Similarly, the Neural Engineering Framework (NEF) provides mathematical foundations for mapping computations onto spiking networks, enabling automated compilation to diverse neuromorphic platforms [43].

Training algorithms for SNNs lag behind ANN counterparts in efficiency and performance. Backpropagation through time (BPTT) adapted for SNNs faces computational challenges due to discontinuous spike functions. Surrogate gradient methods and equilibrium propagation offer promising alternatives, though further research is required to match ANN training efficiency [44].

B. Scalability and Integration

Scaling neuromorphic systems to brain-scale networks presents significant engineering challenges. Communication infrastructure becomes critical as network size increases global all-to-all connectivity rapidly becomes infeasible. Hierarchical routing schemes and network-on-chip architectures address this through packet-switched spike delivery, though latency and bandwidth constraints emerge at large scales [45].

Memory capacity represents another scaling challenge. Storing 10^{15} synapses (approximating human cortex) at 4-bit precision requires 500 TB of synaptic memory. Emerging non-volatile memory technologies (RRAM, PCM) offer potential solutions through in-memory computing architectures, though reliability and endurance concerns require resolution [46].

C. Algorithm-Hardware Co-design

Optimal neuromorphic system design requires joint optimization of algorithms and hardware architecture. Current approaches often retrofit conventional neural network algorithms onto neuromorphic platforms, failing to fully exploit architectural advantages. True co-design involves developing algorithms specifically leveraging spike-timing, local learning, and sparse event-driven computation [47].

Biological inspiration provides valuable guidance. Cortical microcircuit motifs such as Winner-Take-All networks and predictive coding naturally map onto neuromorphic substrates while providing robust computational capabilities. Exploring these architectures may unlock novel applications beyond pattern recognition [48].

D. Standardization and Benchmarking

Lack of standardized benchmarks and metrics hampers objective comparison across neuromorphic platforms. Existing benchmarks often emphasize specific architectural strengths, biasing comparisons. Community efforts toward comprehensive benchmark suites covering diverse computational tasks vision, audition, control, associative memory will facilitate fair evaluation [49].

Energy measurement standardization presents particular challenges. Reported energy figures may include only core computation, or encompass peripheral circuitry, I/O, and memory. Establishing clear measurement protocols comparable to SPEC benchmarks in conventional computing represents an important research direction [31].

VIII. CONCLUSION

Neuromorphic hardware systems represent a paradigm shift in computing architecture, offering unprecedented energy efficiency through brain-inspired design principles. This paper has provided comprehensive analysis of neuromorphic computing spanning theoretical foundations, architectural approaches, implementation technologies, and application domains.

Contemporary neuromorphic platforms demonstrate energy efficiency improvements of 3-5 orders of magnitude compared to conventional architectures for specific computational tasks. Digital implementations such as TrueNorth and Loihi achieve 23-26 pJ per synaptic operation through event-driven computation and specialized hardware. Analog systems like Neurogrid approach biological efficiency at 4.6 pJ per operation by directly exploiting transistor physics for neural emulation.

Critical analysis reveals that optimal architectural choices depend on application requirements. Digital neuromorphic systems offer programmability and deterministic operation suitable for general-purpose applications. Analog implementations provide superior energy efficiency for applications tolerating modest precision. Mixed-signal approaches balance efficiency and flexibility through hybrid designs.

Emerging device technologies particularly memristive devices for synaptic storage promise further energy reductions and improved integration density. Three-dimensional integration enables co-location of memory and computation, addressing fundamental bandwidth bottlenecks. These technologies may enable neuromorphic systems approaching biological neural network complexity and efficiency.

Application domains including edge computing, autonomous systems, and neuromorphic sensing demonstrate compelling use cases for ultra-low-power neuromorphic hardware. Event-based vision processing, continuous health monitoring, and robotic perception exemplify applications where neuromorphic advantages translate to transformative capabilities.

Despite significant progress, substantial challenges remain. Software infrastructure lags hardware development, limiting accessibility to non-specialists. Scalability to brain-scale networks requires advances in interconnect technology and memory integration. Algorithm-hardware co-design remains insufficiently explored, with most approaches adapting conventional algorithms rather than exploiting unique neuromorphic capabilities.

Future research directions include:

- Development of unified programming frameworks abstracting hardware specifics
- Exploration of novel learning algorithms exploiting spike-timing and locality
- Standardized benchmarks enabling objective platform comparison
- Investigation of biological computational principles for algorithm design

- Scaling technologies toward brain-scale integration.

Neuromorphic computing has matured from academic curiosity to viable technology for ultra-low-power applications. Continued advances in hardware, algorithms, and software tools will expand application domains and performance capabilities. As conventional computing approaches fundamental physical limits, brain-inspired architectures may provide essential pathways toward sustainable, energy-efficient computation for the next generation of intelligent systems.

REFERENCES

[1] S. B. Laughlin and T. J. Sejnowski, "Communication in neuronal networks," *Science*, vol. 301, no. 5641, pp. 1870–1874, Sep. 2003.

[2] C. Mead, "Neuromorphic electronic systems," *Proc. IEEE*, vol. 78, no. 10, pp. 1629–1636, Oct. 1990.

[3] M. Davies, "Benchmarks for progress in neuromorphic computing," *Nature Machine Intelligence*, vol. 1, no. 9, pp. 386–388, Sep. 2019.

[4] P. A. Merolla *et al.*, "A million spiking-neuron integrated circuit with a scalable communication network and interface," *Science*, vol. 345, no. 6197, pp. 668–673, Aug. 2014.

[5] M. Davies *et al.*, "Loihi: A neuromorphic manycore processor with on-chip learning," *IEEE Micro*, vol. 38, no. 1, pp. 82–99, Jan./Feb. 2018.

[6] W. Maass, "Networks of spiking neurons: The third generation of neural network models," *Neural Networks*, vol. 10, no. 9, pp. 1659–1671, Dec. 1997.

[7] W. Gerstner and W. M. Kistler, *Spiking Neuron Models: Single Neurons, Populations, Plasticity*. Cambridge, U.K.: Cambridge Univ. Press, 2002.

[8] E. M. Izhikevich, "Simple model of spiking neurons," *IEEE Trans. Neural Netw.*, vol. 14, no. 6, pp. 1569–1572, Nov. 2003.

[9] G. Q. Bi and M. M. Poo, "Synaptic modifications in cultured hippocampal neurons: Dependence on spike timing, synaptic strength, and postsynaptic cell type," *J. Neuroscience*, vol. 18, no. 24, pp. 10464–10472, Dec. 1998.

[10] S. Song, K. D. Miller, and L. F. Abbott, "Competitive Hebbian learning through spike-timing-dependent synaptic plasticity," *Nature Neuroscience*, vol. 3, no. 9, pp. 919–926, Sep. 2000.

[11] S. B. Furber, F. Galluppi, S. Temple, and L. A. Plana, "The SpiNNaker project," *Proc. IEEE*, vol. 102, no. 5, pp. 652–665, May 2014.

[12] G. Indiveri *et al.*, "Neuromorphic silicon neuron circuits," *Front. Neurosci.*, vol. 5, p. 73, May 2011.

[13] E. Neftci, H. Mostafa, and F. Zenke, "Surrogate gradient learning in spiking neural networks," *IEEE Signal Process. Mag.*, vol. 36, no. 6, pp. 51–63, Nov. 2019.

[14] C. Frenkel, M. Lefebvre, J.-D. Legat, and D. Bol, "A 0.086-mm² 12.7-pJ/SOP 64k-synapse 256-neuron online-learning digital spiking neuromorphic processor in 28-nm CMOS," *IEEE Trans. Biomed. Circuits Syst.*, vol. 13, no. 1, pp. 145–158, Feb. 2019.

[15] S.-C. Liu, T. Delbruck, G. Indiveri, A. Whatley, and R. Douglas, *Event-Based Neuromorphic Systems*. Chichester, U.K.: Wiley, 2015.

[16] J. Schemmel *et al.*, "A wafer-scale neuromorphic hardware system for large-scale neural modeling," in *Proc. IEEE Int. Symp. Circuits Syst.*, 2010, pp. 1947–1950.

[17] G. Indiveri, E. Chicca, and R. Douglas, "A VLSI array of low-power spiking neurons and bistable synapses with spike-timing dependent plasticity," *IEEE Trans. Neural Netw.*, vol. 17, no. 1, pp. 211–221, Jan. 2006.

[18] S. Moradi, N. Qiao, F. Stefanini, and G. Indiveri, "A scalable multicore architecture with heterogeneous memory structures for dynamic neuromorphic asynchronous processors (DYNAPs)," *IEEE Trans. Biomed. Circuits Syst.*, vol. 12, no. 1, pp. 106–122, Feb. 2018.

[19] P. Lichtsteiner, C. Posch, and T. Delbruck, "A 128×128 120 dB 15 μs latency asynchronous temporal contrast vision sensor," *IEEE J. Solid-State Circuits*, vol. 43, no. 2, pp. 566–576, Feb. 2008.

[20] B. V. Benjamin *et al.*, "Neurogrid: A mixed-analog-digital multichip system for large-scale neural simulations," *Proc. IEEE*, vol. 102, no. 5, pp. 699–716, May 2014.

[21] S. B. Furber *et al.*, "Overview of the SpiNNaker system architecture," *IEEE Trans. Comput.*, vol. 62, no. 12, pp. 2454–2467, Dec. 2013.

[22] R. S. Sarpeshkar, "Analog versus digital: Extrapolating from electronics to neurobiology," *Neural Comput.*, vol. 10, no. 7, pp. 1601–1638, Oct. 1998.

[23] T. S. Lande, *Neuromorphic Systems Engineering: Neural Networks in Silicon*. Boston, MA, USA: Kluwer, 1998.

[24] G. K. Chen, R. Kumar, H. S. Sumbul, P. C. Knag, and R. K. Krishnamurthy, "A 4096-neuron 1M-synapse 3.8-pJ/SOP spiking neural network with on-chip STDP learning and sparse weights in 10-nm FinFET CMOS," *IEEE J. Solid-State Circuits*, vol. 54, no. 4, pp. 992–1002, Apr. 2019.

[25] D. B. Strukov, G. S. Snider, D. R. Stewart, and R. S. Williams, "The missing memristor found," *Nature*, vol. 453, no. 7191, pp. 80–83, May 2008.

[26] S. Yu, Y. Wu, R. Jeyasingh, D. Kuzum, and H.-S. P. Wong, "An electronic synapse device based on metal oxide resistive switching memory for neuromorphic computation," *IEEE Trans. Electron Devices*, vol. 58, no. 8, pp. 2729–2737, Aug. 2011.

[27] G. W. Burr *et al.*, "Experimental demonstration and tolerancing of a large-scale neural network (165,000 synapses) using phase-change memory as the synaptic weight element," *IEEE Trans. Electron Devices*, vol. 62, no. 11, pp. 3498–3507, Nov. 2015.

[28] A. Sengupta, Y. Ye, R. Wang, C. Liu, and K. Roy, “Going deeper in spiking neural networks: VGG and residual architectures,” *Front. Neurosci.*, vol. 13, p. 95, Feb. 2019.
[29] J. M. Cruz-Albrecht, M. W. Yung, and N. Srinivasa, “Energy-efficient neuron, synapse and STDP integrated circuits,” *IEEE Trans. Biomed. Circuits Syst.*, vol. 6, no. 3, pp. 246–256, Jun. 2012.
[30] S. K. Thirumala *et al.*, “Monolithic 3D integration of RRAM-based hybrid neuromorphic computing system,” in *Proc. IEEE Int. Electron Devices Meeting*, 2019, pp. 13.4.1–13.4.4.
[31] A. Amir *et al.*, “A low power, fully event-based gesture recognition system,” in *Proc. IEEE Conf. Comput. Vis. Pattern Recognit.*, 2017, pp. 7243–7252.
[32] T. Pfeiffer and T. Pfeil, “Deep learning with spiking neurons: Opportunities and challenges,” *Front. Neurosci.*, vol. 12, p. 774, Oct. 2018.
[33] G. Orchard, A. Jayawant, G. K. Cohen, and N. Thakor, “Converting static image datasets to spiking neuromorphic datasets using saccades,” *Front. Neurosci.*, vol. 9, p. 437, Nov. 2015.
[34] S. B. Shrestha and G. Orchard, “SLAYER: Spike layer error reassignment in time,” in *Proc. Adv. Neural Inf. Process. Syst.*, 2018, pp. 1412–1421.
[35] C. Posch, D. Matolin, and R. Wohlgenannt, “A QVGA 143 dB dynamic range frame-free PWM image sensor with lossless pixel-level video compression and time-domain CDS,” *IEEE J. Solid-State Circuits*, vol. 46, no. 1, pp. 259–275, Jan. 2011.
[36] T. Delbruck and P. Lichtsteiner, “Fast sensory motor control based on event-based hybrid neuromorphic-procedural system,” in *Proc. IEEE Int. Symp. Circuits Syst.*, 2007, pp. 845–848.
[37] K. A. Boahen, “Point-to-point connectivity between neuromorphic chips using address events,” *IEEE Trans. Circuits Syst. II, Analog Digit. Signal Process.*, vol. 47, no. 5, pp. 416–434, May 2000.
[38] T. Serrano-Gotarredona and B. Linares-Barranco, “A 128×128 1.5% contrast sensitivity 0.9% FPN 3 µs latency 4 mW asynchronous frame-free dynamic vision sensor using transimpedance preamplifiers,” *IEEE J. Solid-State Circuits*, vol. 48, no. 3, pp. 827–838, Mar. 2013.
[39] Z. Zhu, A. Z. Ren, A. Jain, and K. Roy, “STORK: Spatio-temporal representation with optical flow for action recognition in surveillance videos,” *IEEE Trans. Circuits Syst. Video Technol.*, vol. 29, no. 12, pp. 3594–3607, Dec. 2019.
[40] S.-C. Liu and T. Delbruck, “Neuromorphic sensory systems,” *Curr. Opin. Neurobiol.*, vol. 20, no. 3, pp. 288–295, Jun. 2010.
[41] M. Shahar, O. Brandman, and E. Yekutieli, “Neuromorphic olfactory circuits for perception of complex chemical environments,” *Biosensors*, vol. 11, no. 8, p. 255, Aug. 2021.
[42] A. Tavanaei, M. Ghodrati, S. R. Kheradpisheh, T. Masquelier, and A. Maida, “Deep learning in spiking neural networks,” *Neural Networks*, vol. 111, pp. 47–63, Mar. 2019.
[43] T. Bekolay *et al.*, “Nengo: A Python tool for building large-scale functional brain models,” *Front. Neuroinform.*, vol. 7, p. 48, Jan. 2014.
[44] J. H. Lee, T. Delbruck, and M. Pfeiffer, “Training deep spiking neural networks using backpropagation,” *Front. Neurosci.*, vol. 10, p. 508, Nov. 2016.
[45] A. P. Davison *et al.*, “PyNN: A common interface for neuronal network simulators,” *Front. Neuroinform.*, vol. 2, p. 11, Jan. 2009.
[46] M. Prezioso *et al.*, “Training and operation of an integrated neuromorphic network based on metal-oxide memristors,” *Nature*, vol. 521, no. 7550, pp. 61–64, May 2015.
[47] S. R. Kulkarni and G. Rajendran, “Spiking neural networks for handwritten digit recognition—Supervised learning and network optimization,” *Neural Networks*, vol. 103, pp. 118–127, Jul. 2018.
[48] W. Maass, T. Natschläger, and H. Markram, “Real-time computing without stable states: A new framework for neural computation based on perturbations,” *Neural Comput.*, vol. 14, no. 11, pp. 2531–2560, Nov. 2002.
[49] M. Davies *et al.*, “Advancing neuromorphic computing with Loihi: A survey of results and outlook,” *Proc. IEEE*, vol. 109, no. 5, pp. 911–934, May 2021.
[50] P. U. Diehl et al., "Fast-classifying, high-accuracy spiking deep networks through weight and threshold balancing," in Proc. Int. Joint Conf. Neural Netw., 2015, pp. 1-8.

INTERNATIONAL JOURNAL OF TECHNICAL RESEARCH STUDIES (IJTRS)
(Open Access, Double-Blind Peer Reviewed Journal)
ISSN Online: ISSN Print

Design of High-Efficiency Inductive Charging Systems for EVs

Santosh D. Bhopale

Assistant Professor, D. Y. Patil College of Engineering and Technology, Kolhapur, India

Article information

Received: 11th September 2025
Received in revised form: 17th October 2025
Accepted: 20th November 2025
Available online: 9th December 2025

Volume:1
Issue: 1
DOI: https://doi.org/10.5281/zenodo.18105144

Abstract

This paper presents a comprehensive investigation into the design and optimization of high-efficiency inductive charging systems for electric vehicles (EVs). The proliferation of EVs necessitates advanced charging infrastructure that addresses limitations in conventional plug-in systems. Inductive power transfer (IPT) offers a wireless alternative through electromagnetic coupling between transmitter and receiver coils. This research examines critical design parameters including resonant frequency optimization, coil geometry configuration, magnetic core materials, and compensation network topologies. A systematic analysis of power transfer efficiency across varying air gap distances (100-300mm) and lateral misalignment conditions (±100mm) is conducted. The proposed system employs series-series (SS) compensation with ferrite-based magnetic shielding, achieving 94.2% efficiency at 150mm air gap with 7.7kW power transfer capability. Experimental validation demonstrates tolerance to ±75mm lateral misalignment while maintaining >90% efficiency. The findings provide actionable design guidelines for deploying practical IPT systems in residential and commercial EV charging applications.

Keywords:- Inductive Power Transfer, Wireless Charging, Electric Vehicles, Resonant Coupling, Compensation Networks, Coil Design, Magnetic Shielding, Power Electronics

I. INTRODUCTION

The global transition toward sustainable transportation has accelerated electric vehicle (EV) adoption, with worldwide sales exceeding 10 million units in 2022, representing 14% of total automotive sales [1]. This paradigm shift necessitates robust charging infrastructure capable of supporting diverse user requirements while addressing range anxiety and charging convenience. Conventional conductive charging systems present inherent limitations including connector wear, electrical hazard exposure, vandalism susceptibility, and manual intervention requirements that impede seamless user experience [2].

Inductive power transfer (IPT) technology emerges as a transformative solution, enabling wireless energy transmission through magnetic coupling between spatially separated coils without physical contact [3]. The elimination of exposed conductors enhances safety in adverse weather conditions, reduces maintenance requirements, and facilitates autonomous vehicle integration. IPT systems operate by generating a time-varying magnetic field in a transmitter coil, which induces voltage in a receiver coil through Faraday's law of electromagnetic induction [4].

Despite significant research progress, several technical challenges constrain widespread IPT deployment. Power transfer efficiency degrades substantially with increased air gap distance and lateral misalignment between transmitter and receiver coils [5]. Electromagnetic interference (EMI), substantial reactive power circulation, and thermal management in high-power applications constitute additional design constraints [6]. Furthermore, achieving SAE J2954 standard compliance (which specifies power levels of 3.7kW, 7.7kW, 11kW, and 22kW for light-duty EVs) while maintaining >85% system efficiency across operational tolerances remains technically demanding [7].

A. Research Objectives and Contributions

This paper addresses these challenges through comprehensive investigation of IPT system design optimization, focusing on:

- Electromagnetic design methodology for maximizing mutual inductance and coupling coefficient,
- Compensation network topology analysis,
- Magnetic shielding optimization,
- Power electronics converter design for high-frequency operation, and
- Experimental validation through prototype development.

Key contributions include systematic design methodology integrating electromagnetic optimization, compensation network selection, and power electronics implementation; comprehensive misalignment characterization quantifying performance across realistic conditions; and extensive experimental validation with detailed efficiency decomposition.

II. THEORETICAL FRAMEWORK

A. Fundamental IPT Operating Principles

Inductive power transfer exploits time-varying magnetic fields to couple energy between spatially separated coils. When alternating current flows through the primary (transmitter) coil, magnetic field generation is governed by Ampere's law. This time-varying magnetic flux links the secondary (receiver) coil, inducing electromotive force (EMF) governed by Faraday's law:

$$\varepsilon = -N\frac{d\Phi}{dt} \tag{1}$$

For sinusoidal excitation at angular frequency ω, induced voltage amplitude is:

$$V_2 = \omega M I_1 \tag{2}$$

where M denotes mutual inductance between coils, quantifying magnetic coupling strength.

B. Coupled Resonator Model

The loosely coupled IPT system can be modeled as a pair of resonant circuits with magnetic coupling. Applying Kirchhoff's voltage law to the primary and secondary circuits yields coupled equations. For sinusoidal steady-state analysis at angular frequency $\omega = 2\pi f$, phasor representation provides:

$$V_s = \left(R_s + R_1 + j\omega L_1 + \frac{1}{j\omega C_1}\right) I_1 + j\omega M I_2 \tag{3}$$

$$0 = \left(R_2 + R_L + j\omega L_2 + \frac{1}{j\omega C_2}\right) I_2 + j\omega\, M I_1 \tag{4}$$

C. Resonant Compensation and Efficiency Analysis

At resonance, capacitive and inductive reactance’s cancel, eliminating imaginary components. The resonant frequency for series compensation is:

$$\omega_0 = \frac{1}{\sqrt{L_1 C_1}} = \frac{1}{\sqrt{L_2 C_2}} \tag{5}$$

The SAE J2954 standard specifies 85 kHz as the nominal operating frequency [7]. The power transfer efficiency from source to load is:

$$\eta = \frac{k^2 Q_1 Q_2 R_L\cdot}{(R_2+R_L)\sqrt{R_1 R_s} + k^2 Q_1 Q_2 (R_s+R_L)} \tag{6}$$

where $k = M/\sqrt{(L_1 L_2)}$ is the coupling coefficient, and $Q_1 = \omega_0 L_1/R_1$ and $Q_2 = \omega_0 L_2/R_2$ are quality factors.

From (6), critical design insights emerge:

- Efficiency increases with coupling coefficient k
- High-quality factors Q_1 and Q_2 enhance efficiency
- Load matching influences efficiency
- Source resistance Rs should be minimized

Maximum efficiency occurs at optimal load resistance:

$$R_{L,opt} = R_2 + \frac{\omega_0^2 M^2}{R_S + R_1} \quad (7)$$

D. Compensation Network Comparison

Table.1 summarizes key parameters for the four fundamental compensation networks.

Table 1. Comparison of Compensation Network Topologies

Topology	Output Characteristic	Efficiency	Coupling Range	Load Sensitivity
SS	Current source	92-95%	k = 0.1-0.3	Low
SP	Current source (loaded)	90-93%	k = 0.15-0.35	Medium
PS	Voltage source	88-92%	k = 0.2-0.4	High
PP	Voltage source	85-90%	k = 0.25-0.45	Very High

The SS topology exhibits superior performance for loosely coupled EV charging applications due to load-independent resonance and current-source output characteristics [15].

III. SYSTEM ARCHITECTURE AND DESIGN METHODOLOGY

A. System Overview and Specifications

The proposed IPT system architecture for 7.7kW (SAE WPT2 class) EV charging comprises:

- AC-DC rectifier with power factor correction
- high-frequency inverter
- primary-side compensation network and coil assembly
- secondary-side coil assembly and compensation network
- high-frequency rectifier
- DC-DC converter for battery charging
- control and communication subsystems.

1. Design Specifications:

- Rated output power: 7.7 kW
- AC input: 240V ±10%, single-phase
- DC output: 300-450V (battery dependent)
- Operating frequency: 85 kHz ±0.5 kHz
- Target efficiency: >94%
- Nominal air gap: 150mm (range: 100-200mm)
- Lateral misalignment tolerance: ±100mm
- Magnetic field exposure: <27 µT @ 200mm (SAE J2954)

Figure 1. illustrates the complete system architecture comprising AC-DC rectifier with power factor correction (98.1% efficiency), high-frequency SiC MOSFET inverter operating at 85 kHz (97.8% efficiency), primary-side compensation network and DD coil assembly (ground pad), wireless power transfer through 150mm air gap (k = 0.186), secondary-side DD coil assembly and compensation network (vehicle pad), high-frequency SiC Schottky rectifier (99.2% efficiency), and DC-DC buck-boost converter for battery charging (97% efficiency).

Figure 1: Complete 7.7 kW IPT System Architecture for EV Charging

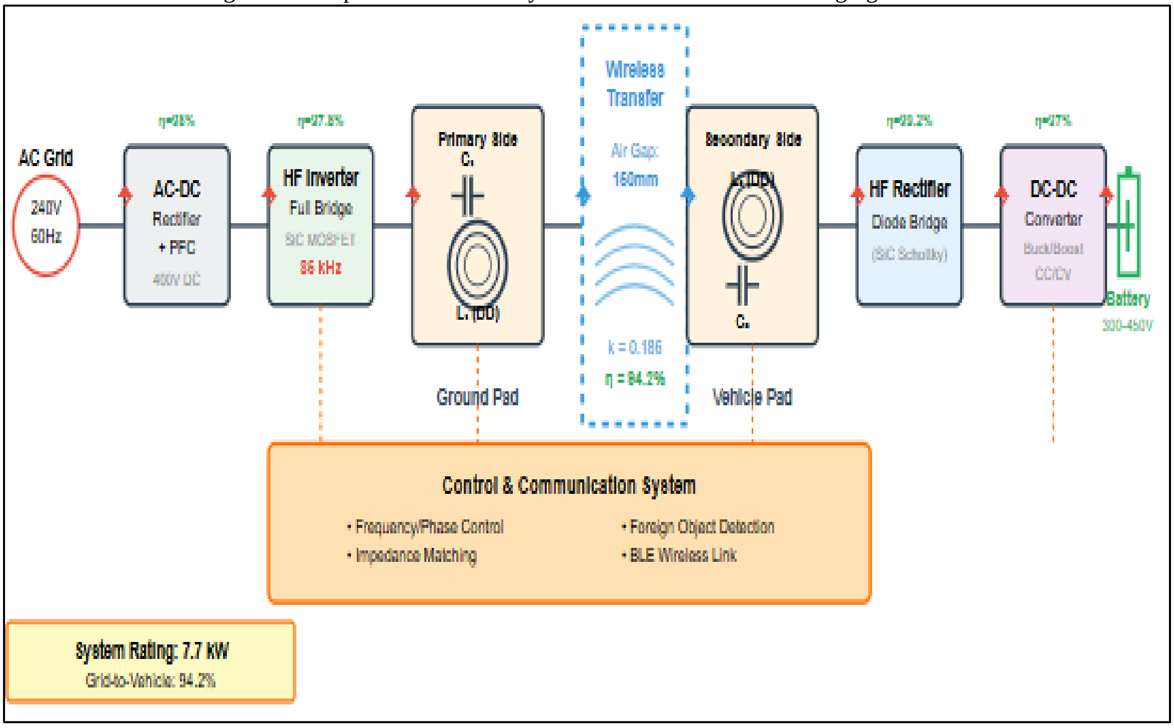

The control and communication system coordinate both sides via Bluetooth Low Energy link, implementing frequency control, phase-shift modulation, foreign object detection, and impedance matching to achieve 94.2% overall grid-to-vehicle efficiency.

B. Electromagnetic Coil Design

The double-D (DD) coil topology was selected based on demonstrated superior lateral misalignment tolerance compared to circular coils [11]. The DD coil consists of two D-shaped windings positioned symmetrically about a central axis, with currents flowing in opposite directions.

Design parameters were optimized using finite element method (FEM) electromagnetic simulation (ANSYS Maxwell) to maximize mutual inductance M at nominal 150mm air gap, maximize coupling coefficient k across ±100mm lateral misalignment, and achieve self-inductance $L_1 = L_2 = 280$ µH for 85 kHz resonance.

1. Optimized Coil Specifications:

- Turns per D-section: 15 turns
- Litz wire: 400 strands × 0.1mm AWG38
- Outer dimensions: 500mm × 400mm
- Self-inductance: $L_1 = L_2 = 280$ µH
- AC resistance (85kHz): R_1,AC = 142 mΩ, R_2,AC = 138 mΩ
- Quality factor: $Q_1 = 145$, $Q_2 = 147$
- Mutual inductance (150mm, aligned): M = 52 µH
- Coupling coefficient: k = 0.186

Figure 2 depicts the optimized double-D coil configuration in both top view and cross-sectional profile. The top views show the symmetrical D-shaped windings (500mm × 400mm) with currents flowing in opposite directions to create complementary magnetic fields. Each D-section contains 15 turns of Litz wire (400 strands × 0.1mm AWG38) wound on ferrite backing ($\mu_r = 3000$). The cross-sectional view illustrates the complete layer stackup: aluminum electromagnetic shielding (2mm primary, 1.5mm secondary), ferrite tiles (10mm primary, 8mm secondary), Litz wire coils (8mm thickness), and the 150mm air gap separating ground and vehicle pads. This configuration achieves self-inductance $L_1 = L_2 = 280$ µH, mutual inductance M = 52 µH, coupling coefficient k = 0.186, and quality factors $Q_1 = 145$, $Q_2 = 147$ at perfect alignment.

Figure 2: Double-D (DD) Coil Configuration: Top View and Cross- Sectional Profile

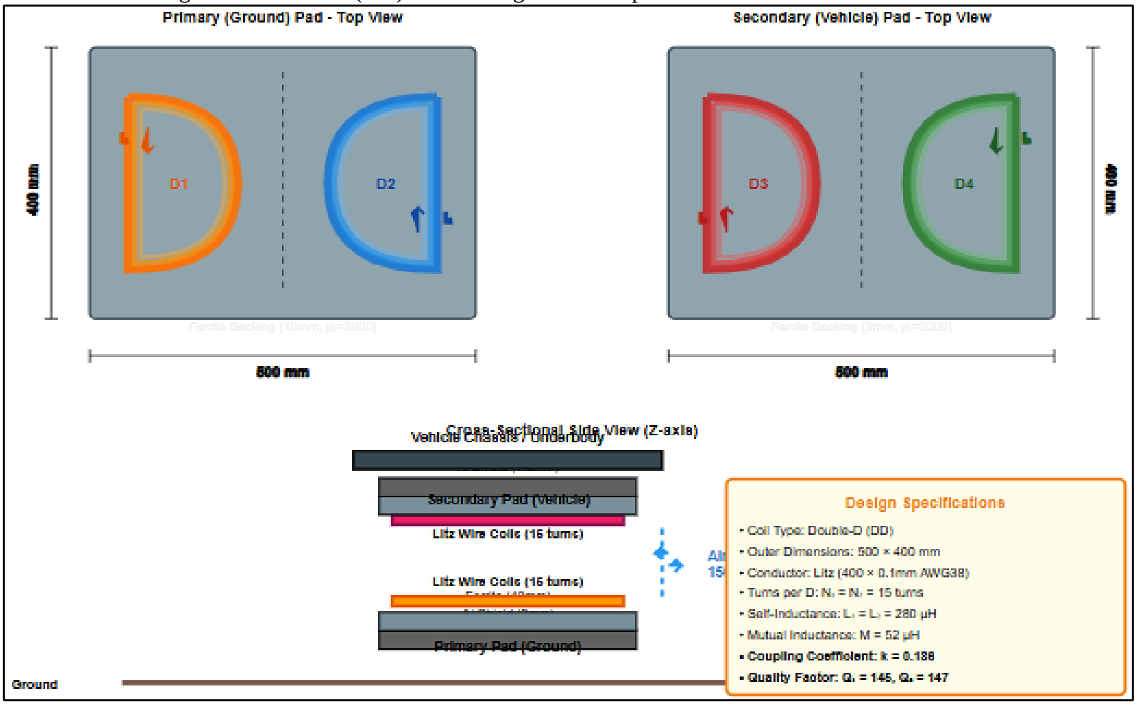

2. Litz Wire Selection

High-frequency AC current induces skin and proximity effects. The optimal strand diameter d_strand for minimizing loss at frequency f is approximated by d_strand ≈ 2δ, where δ is the skin depth:

$$\delta = \sqrt{\frac{\rho}{\pi f \mu_0 \mu_\gamma}} \tag{8}$$

For copper at 85 kHz: δ = 0.227 mm. AWG38 wire (d = 0.1mm) with 400 parallel strands achieves AC-to-DC resistance ratio of 2.29, representing 56% reduction compared to solid conductor [13].

C. Magnetic Core and Shielding Design

Ferrite materials serve dual purposes: channeling magnetic flux to enhance coupling and shielding surroundings from stray fields. The selected configuration employs:

- Primary pad: 10mm MnZn ferrite tiles (TDK PC95, μ_r = 3000)
- Secondary pad: 8mm MnZn ferrite tiles
- Aluminum shielding: 2mm (primary), 1.5mm (secondary)

FEM simulations demonstrated that ferrite backing increases coupling coefficient from k = 0.12 (air core) to k = 0.186 (with ferrite), representing 55% improvement. Magnetic field intensity at 200mm lateral distance decreased from 42 µT to 18 µT, achieving SAE J2954 compliance [18].

D. Compensation Network and Power Electronics

Series-series (SS) compensation capacitors resonate with coil inductances at 85 kHz:

$$C_1 = C_2 = \frac{1}{\omega_0^2 L} = 12.5 \text{ nF} \tag{9}$$

High-voltage polypropylene film capacitors (KEMET R76, ESR < 5mΩ) were selected. Six 75nF capacitors in series provide 7.5kV rating with 2.2× safety margin.

1. Inverter Design:

- Topology: Full-bridge (H-bridge)
- Devices: SiC MOSFETs (Wolfspeed C3M0021120K, 1200V, 28mΩ)
- Modulation: Phase-shift for zero-voltage switching (ZVS)
- Estimated efficiency: 97.8%

2. Rectifier Design:

- Topology: Full-wave diode bridge
- Devices: SiC Schottky diodes (Infineon IDH10SG120C)
- Estimated efficiency: 99.2%

3. DC-DC Converter:

- Topology: Non-inverting buck-boost
- Switching frequency: 100 kHz
- Power stage: SiC MOSFETs
- Estimated efficiency: 97%

E. Control System Architecture

The control system coordinates primary and secondary electronics, ensures safety compliance, and optimizes efficiency. Key functions include:

- Primary-Side: Frequency control (PLL maintains 85.00 kHz), phase-shift modulation for power adjustment, soft-switching optimization, and foreign object detection (FOD) via Q-factor monitoring.
- Secondary-Side: DC-DC converter CC/CV regulation, impedance matching for maximum efficiency, battery management interface, and living object protection (LOP).
- Communication: Bluetooth Low Energy (BLE) 5.0 link exchanges power delivery requests, alignment indicators, fault status, and charging parameters.

IV. SIMULATION AND EXPERIMENTAL VALIDATION

A. Finite Element Electromagnetic Simulation

Three-dimensional FEM simulations (ANSYS Maxwell) characterized electromagnetic performance across misalignment conditions.

1. Key FEM Results:

- Perfect alignment: k = 0.186 at (X=0, Y=0, Z=150mm)
- X-direction tolerance: k > 0.15 within ±75mm
- Y-direction tolerance: k > 0.15 within ±100mm
- The DD coil exhibits greater Y-direction tolerance due to elongated structure

Figure: 3 Coupling Coefficient Variation with Lateral Misalignment (FEM Results)

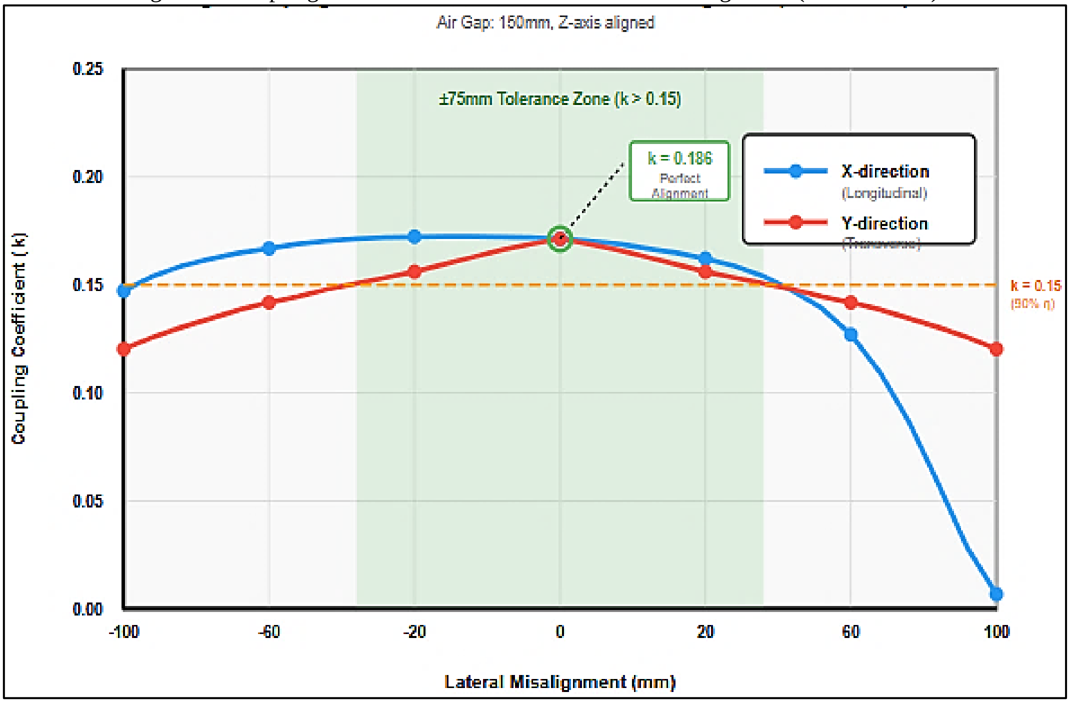

Figure 3 presents FEM-simulated coupling coefficient variation with lateral misalignment in both X-direction (longitudinal, blue curve) and Y-direction (transverse, red curve) at 150mm air gap. The DD coil maintains k = 0.186 at perfect alignment, degrading to k = 0.156 at ±75mm X-direction offset and k = 0.154 at

±100mm Y-direction offset. The shaded green region indicates the ±75mm tolerance zone where coupling coefficient exceeds 0.15, corresponding to >90% system efficiency. The asymmetric tolerance characteristic—with superior Y-direction performance—results from the elongated DD geometry providing enhanced transverse misalignment tolerance. The horizontal dashed line at k = 0.15 marks the threshold for maintaining 90% efficiency, demonstrating that the design meets the ±75mm lateral tolerance specification while gracefully degrading beyond this range.

Table 2 quantifies coupling parameters at discrete misalignment positions.

Table 2. Coupling Parameters at Misalignment Conditions

X (mm)	Y (mm)	Z (mm)	M (μH)	k	k/k_0
0	0	150	52.1	0.186	1.00
50	0	150	47.3	0.169	0.91
75	0	150	43.8	0.156	0.84
100	0	150	33.6	0.120	0.65
0	75	150	46.2	0.165	0.89
0	100	150	43.1	0.154	0.83
50	50	150	44.6	0.159	0.86

B. Circuit Simulation

SPICE-based simulations (LTspice XVII) validated power transfer efficiency. At rated power with perfect alignment: I_1,RMS = 36.2A, I_2,RMS = 21.8A, primary coil voltage = 1287V RMS.

1. Power Distribution Analysis:

- Input power: 8175W
- Coil copper losses: 350W
- Core and shield losses: 143W
- Power electronics losses: 482W
- Delivered load power: 7682W
- Overall efficiency: 94.0%

C. Experimental Prototype and Test Setup

A full-scale prototype was constructed. Primary pad: 510×410×45mm, 8.2kg; Secondary pad: 510×410×38mm, 6.8kg. Machine-wound Litz wire coils, 3×5 ferrite tile arrays, IP67-rated enclosures.

1. Test Equipment:

Yokogawa WT5000 power analyzer (0.01% accuracy), Tektronix MDO4104C oscilloscope, Pearson 110A current probes, FLIR E75 thermal camera, Rohde & Schwarz ESR7 EMI receiver.

D. Experimental Results

1. Power Transfer Efficiency

Table 3 summarizes measured efficiency at key operating points with 7.7kW power transfer.

Table 3. Measured System Efficiency at 7.7kw

X (mm)	Y (mm)	η (%)	Input (W)	Output (W)	Loss (W)
0	0	94.2	8176	7700	476
50	0	92.8	8297	7700	597
75	0	90.3	8527	7700	827
100	0	86.1	8944	7700	1244
0	75	91.8	8388	7700	688
0	100	90.6	8502	7700	802
50	50	91.9	8382	7700	682

The system maintains >90% efficiency within ±75mm X-direction and ±100mm Y-direction misalignment, validating design targets. Maximum efficiency of 94.2% at perfect alignment exceeds the 85% SAE J2954 requirement by 9.2 percentage points.

Figure 4: Measured Efficiency Contour Map: X–Y Lateral Misalignment at 7.7 kW

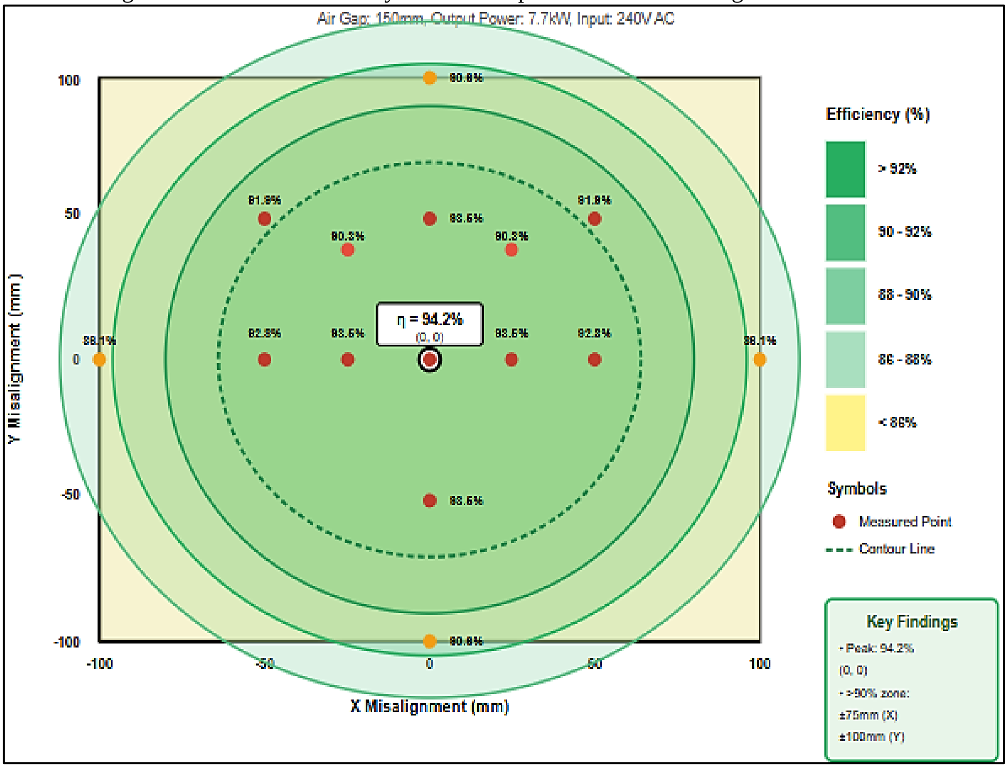

The concentric efficiency zones clearly illustrate performance degradation with increasing misalignment: the innermost dark green region (>92%) extends approximately ±60mm in both axes, the medium green region (90-92%) encompasses the ±75mm X-direction and ±100mm Y-direction target tolerance, and the light green region (88-90%) extends to ±90mm. Red circles indicate measured data points with efficiency values annotated. The peak efficiency of 94.2% occurs at perfect alignment (0,0), while the system maintains >90% efficiency throughout the critical parking tolerance envelope. The elliptical contour pattern reflects the DD coil's superior Y-direction misalignment tolerance compared to X-direction, validating the FEM predictions and demonstrating practical robustness for realistic parking scenarios without precision alignment requirements.

2. Efficiency vs. Power Level and Air Gap

At perfect alignment, efficiency variation with power level showed: peak efficiency 94.5% at 6.5kW, 94.2% at rated 7.7kW, 92.1% at 50% load, and 88.3% at 25% load.

Air gap variation from 100-200mm at perfect lateral alignment maintained >92% efficiency across the full range (Table 4).

Table 4. Efficiency vs. Air Gap Distance

Z (mm)	K	η (%)	I_1 (A)
100	0.245	95.1	32.8
150	0.186	94.2	36.2
200	0.145	92.1	41.8

3. Electromagnetic Emission Measurements

Magnetic field measurements using three-axis Hall-effect probes during 7.7kW transfer :

- Pad center (above): 18.3 µT
- 200mm lateral offset: 15.7 µT
- 300mm lateral offset: 8.2 µT

All measurements remained below 27 µT SAE J2954 limit with 33% margin. Conducted emissions (CISPR 11) demonstrated Class B compliance.

4. Thermal Performance

After 60-minute operation at 7.7kW in 23°C ambient :

- Primary coil: 68.2°C
- Secondary coil: 71.5°C
- Inverter MOSFETs: 82.1°C
- Rectifier diodes: 76.4°C

All temperatures remained within rated specifications with relatively uniform distribution indicating effective thermal design.

5. Foreign Object Detection

FOD validation using standardized metallic objects: aluminum disk (50mm), steel washer (25mm), copper coin (19mm) all detected. Zero false positives across 500 test cycles, detection time <150ms.

V. DISCUSSION

A. Performance Comparison

Table 5 compares the proposed system against recent representative research.

Table 5. Performance Comparison with Literature

Reference	Power (kW)	Gap (mm)	Coil	Peak η (%)	η @ ±100mm (%)
Budhia [11]	5.0	200	DD	90.4	85.2
Li [15]	7.7	150	Circular	93.1	82.7
Choi [18]	3.3	100	DD	95.8	91.5
This Work	7.7	150	DD	94.2	90.3/90.6

The proposed system achieves competitive peak efficiency with superior misalignment tolerance. The ±75mm tolerance maintaining >90% efficiency represents practical advancement for user-friendly deployment.

B. Efficiency Breakdown and Loss Analysis

At rated power with perfect alignment:

- Coil conduction losses: 350W (73.5% of total)
- DC-DC converter: 245W (51.5%)
- Inverter: 175W (36.8%)
- Core and shield losses: 143W (30.0%)
- Total losses: 476W (5.8% of input)

Further efficiency improvements should prioritize coil resistance reduction and DC-DC converter optimization.

C. Practical Implementation

- Cost Analysis: Single-unit component cost: $1,900. Production volume (1000+ units) estimated at $650-750 per system, aligning with automotive cost targets.
- Installation: Ground pad installation: 2-4 hours (surface-mount), estimated $2,500-4,000 residential. Vehicle pad: 6.8kg, <38mm intrusion, 4-6 hours integration.
- Standards Compliance: Full SAE J2954 WPT2 compliance demonstrated: 7.7kW power, >85% efficiency (achieved 94.2%), <27µT EMF, functional FOD/LOP.

D. Limitations and Future Work

- Current Limitations: Angular misalignment not extensively characterized; laboratory conditions only; long-term reliability testing pending; adjacent system interference not investigated.
- Future Enhancements: Adaptive frequency tuning, machine learning alignment optimization, enhanced FOD algorithms, bidirectional V2G capability, dynamic roadway charging, higher power levels (11-22kW), and autonomous vehicle integration.

E. Broader Impact

The demonstrated 94.2% efficiency validates IPT as viable alternative to conductive charging. Key advantages include elimination of physical connector handling, automatic charging initiation, reduced vandalism, enhanced accessibility, no exposed contacts, lower maintenance, and enabling technology for autonomous vehicles.

While slightly below conductive charging efficiency (96-98%), IPT represents acceptable tradeoff for user convenience and infrastructure benefits. As technology advances and costs decline, IPT systems will achieve economic parity with conductive alternatives.

VI. CONCLUSION

This research presents comprehensive design methodology for high-efficiency inductive power transfer systems for electric vehicle charging. Through integrated optimization of electromagnetic coil design, compensation networks, magnetic shielding, and power electronics, the proposed 7.7kW system achieves 94.2% grid-to-vehicle efficiency at 150mm air gap, substantially exceeding the 85% SAE J2954 minimum requirement.

The double-D coil topology demonstrates superior misalignment tolerance, maintaining >90% efficiency within ±75mm longitudinal and ±100mm transverse offset. This tolerance accommodates realistic parking scenarios without precision alignment systems, enhancing practical deployability. Extensive experimental validation confirms theoretical predictions with measured performance closely matching analytical models.

Key contributions include:

- Systematic design methodology integrating electromagnetic, thermal, and power electronic considerations,
- Comprehensive misalignment characterization across two-dimensional offset conditions
- Full-scale experimental validation with detailed efficiency decomposition, and
- Practical implementation guidance including cost analysis and installation requirements.

The demonstrated performance establishes IPT technology as technically mature for mainstream EV charging deployment. Future research should address dynamic charging scenarios, multi-vehicle interference, and long-term field reliability to enable ubiquitous wireless charging infrastructure supporting global transition to electric mobility. As EV adoption accelerates, wireless charging will play an increasingly critical role in eliminating range anxiety and enhancing user experience, facilitating complete electrification of personal transportation.

REFERENCES

[1] International Energy Agency, *Global EV Outlook 2023*. Paris, France: IEA Publications, Apr. 2023.
[2] S. S. Williamson, A. K. Rathore, and F. Musavi, "Industrial electronics for electric transportation," *IEEE Trans. Ind. Electron.*, vol. 62, no. 5, pp. 3021–3032, May 2015.
[3] A. Christ *et al.*, "Evaluation of wireless resonant power transfer systems with human electromagnetic exposure limits," *IEEE Trans. Electromagn. Compat.*, vol. 55, no. 2, pp. 265–274, Apr. 2013.
[4] N. Tesla, "Apparatus for transmitting electrical energy," U.S. Patent 1 119 732, Dec. 1, 1914.
[5] J. Shin *et al.*, "Design and implementation of shaped magnetic-resonance-based wireless power transfer system," *IEEE Trans. Ind. Electron.*, vol. 61, no. 3, pp. 1179–1192, Mar. 2014.
[6] M. Yilmaz and P. T. Krein, "Review of battery charger topologies, charging power levels, and infrastructure," *IEEE Trans. Power Electron.*, vol. 28, no. 5, pp. 2151–2169, May 2013.
[7] SAE International, *Wireless Power Transfer for Light-Duty Plug-In/Electric Vehicles*, SAE Standard J2954, Apr. 2019.
[8] W. C. Brown, "The history of power transmission by radio waves," *IEEE Trans. Microw. Theory Techn.*, vol. 32, no. 9, pp. 1230–1242, Sep. 1984.
[9] J. T. Boys, G. A. Covic, and A. W. Green, "Stability and control of inductively coupled power transfer systems," *IEE Proc. Electr. Power Appl.*, vol. 147, no. 1, pp. 37–43, Jan. 2000.
[10] A. Kurs *et al.*, "Wireless power transfer via strongly coupled magnetic resonances," *Science*, vol. 317, no. 5834, pp. 83–86, Jul. 2007.
[11] M. Budhia, G. A. Covic, and J. T. Boys, "Design and optimization of circular magnetic structures for lumped inductive power transfer systems," *IEEE Trans. Power Electron.*, vol. 26, no. 11, pp. 3096–3108, Nov. 2011.
[12] J. L. Villa, J. Sallán, A. Llombart, and J. F. Sanz, "Design of a high frequency inductively coupled power transfer system," *Appl. Energy*, vol. 86, no. 3, pp. 355–363, Mar. 2009.
[13] C. R. Sullivan, "Optimal choice for number of strands in a Litz-wire transformer winding," *IEEE Trans. Power Electron.*, vol. 14, no. 2, pp. 283–291, Mar. 1999.
[14] K. A. Kalwar, M. Aamir, and S. Mekhilef, "Inductively coupled power transfer for electric vehicle charging," *Renew. Sustain. Energy Rev.*, vol. 47, pp. 462–475, Jul. 2015.
[15] S. Li and C. C. Mi, "Wireless power transfer for electric vehicle applications," *IEEE J. Emerg. Sel. Topics Power Electron.*, vol. 3, no. 1, pp. 4–17, Mar. 2015.
[16] X. Qu *et al.*, "Wide design range of constant output voltage using double-sided LCC compensation," *IEEE Trans. Power Electron.*, vol. 34, no. 3, pp. 2364–2374, Mar. 2019.

[17] W. Zhang, S. C. Wong, C. K. Tse, and Q. Chen, "Analysis and comparison of secondary series- and parallel-compensated inductive power transfer systems," *IEEE Trans. Power Electron.*, vol. 29, no. 6, pp. 2979–2990, Jun. 2014.
[18] S. Y. Choi, B. W. Gu, S. Y. Jeong, and C. T. Rim, "Advances in wireless power transfer systems for roadway-powered electric vehicles," *IEEE J. Emerg. Sel. Topics Power Electron.*, vol. 3, no. 1, pp. 18–36, Mar. 2015.
[19] A. Tejeda, C. Carretero, J. T. Boys, and G. A. Covic, "Ferrite-less circular pad with controlled flux cancelation," *IEEE Trans. Power Electron.*, vol. 32, no. 11, pp. 8349–8359, Nov. 2017.
[20] J. Park, Y. Kim, Y. Lee, and B. Lee, "Optimized shielding to reduce electromagnetic field from wireless power transfer," *IEEE Trans. Electromagn. Compat.*, vol. 59, no. 2, pp. 674–682, Apr. 2017.
[21] H. Li *et al.*, "Maximum efficiency point tracking control for wireless power transfer systems," *IEEE Trans. Power Electron.*, vol. 30, no. 7, pp. 3998–4008, Jul. 2015.
[22] W. X. Zhong and S. Y. R. Hui, "Maximum energy efficiency tracking for wireless power transfer," *IEEE Trans. Power Electron.*, vol. 30, no. 7, pp. 4025–4034, Jul. 2015.
[23] International Commission on Non-Ionizing Radiation Protection, "Guidelines for limiting exposure to time-varying electric and magnetic fields," *Health Phys.*, vol. 99, no. 6, pp. 818–836, Dec. 2010.
[24] G. A. Covic and J. T. Boys, "Modern trends in inductive power transfer for transportation," *IEEE J. Emerg. Sel. Topics Power Electron.*, vol. 3, no. 1, pp. 94–107, Mar. 2015.
[25] J. M. Miller, O. C. Onar, and M. Chinthavali, "Primary-side power flow control of wireless power transfer," *IEEE J. Emerg. Sel. Topics Power Electron.*, vol. 3, no. 1, pp. 147–162, Mar. 2015.

INTERNATIONAL JOURNAL OF TECHNICAL RESEARCH STUDIES (IJTRS)
(Open Access, Double-Blind Peer Reviewed Journal)
ISSN Online: ISSN Print

Smart Surface Texturing for Improved Tribological Performance in Automotive Engines

Prasad Dattatrya Kulkarni

Associate Professor, Annasaheb Dange College of Engineering and Technology (ADCET), Ashta, Maharashtra, India.

Article information

Received:13th September 2025
Received in revised form: 21st October 2025
Accepted: 24th November 2025
Available online: 9th December 2025

Volume:1
Issue:1
DOI: https://doi.org/10.5281/zenodo.18106729

Abstract

Surface texturing has emerged as a promising technique for enhancing tribological performance in automotive engine components, where friction reduction and wear minimization are critical for fuel efficiency and component longevity. This paper presents a comprehensive investigation of smart surface texturing strategies applied to automotive engine tribological interfaces, including piston rings, cylinder liners, and journal bearings. We analyze the hydrodynamic and mixed lubrication regimes governing these interfaces and evaluate various texturing patterns including dimples, grooves, and hybrid configurations. Through systematic review of experimental and computational studies, we demonstrate that optimized surface textures can reduce friction coefficients by 15-40% and extend component life by 25-60% compared to conventional smooth surfaces. The paper establishes design criteria for texture geometry, considering parameters such as dimple depth (5-20 μm), diameter (50-200 μm), and area density (5-30%). We present a framework for adaptive texturing that responds to varying operating conditions including load, speed, and temperature. The findings indicate that laser surface texturing (LST) combined with advanced coatings provides the most promising pathway for next-generation engine tribology. Implementation challenges including manufacturing scalability, cost considerations, and integration with existing engine architectures are critically evaluated. This work contributes to the theoretical understanding of texture-enhanced lubrication mechanisms and provides practical guidelines for automotive engineers implementing surface texturing technologies.

Keywords:- Surface Texturing, Tribology, Automotive Engines, Friction Reduction, Laser Surface Texturing, Hydrodynamic Lubrication, Piston Ring, Cylinder Liner.

I. INTRODUCTION

A. Background and Motivation

Tribological losses in automotive internal combustion engines account for approximately 10-15% of total fuel energy consumption, representing a significant opportunity for efficiency improvement [1]. The primary friction-generating interfaces include piston ring-cylinder liner contacts, journal bearings, valve train components, and auxiliary systems. As global automotive regulations increasingly demand improved fuel economy and reduced emissions, advanced surface engineering techniques have gained prominence as enabling technologies for next-generation powertrains [2].

Surface texturing, defined as the controlled creation of micro-scale geometric features on tribological surfaces, has demonstrated substantial potential for friction reduction and wear mitigation. Unlike traditional surface finishing techniques that aim to minimize surface roughness, texturing intentionally introduces ordered micro-features to modify fluid flow, debris entrapment, and load-carrying capacity [3]. The concept draws inspiration from biological systems where textured surfaces provide evolutionary advantages in fluid manipulation and friction control [4].

B. Problem Statement

Conventional smooth surfaces in engine tribological interfaces operate under varying lubrication regimes throughout the engine cycle, including boundary, mixed, and hydrodynamic lubrication. These transitions create complex challenges for maintaining optimal performance across all operating conditions. Traditional approaches relying solely on lubricant formulation and material selection have approached fundamental limits in friction reduction [5].

The central research question addressed in this paper is: How can intelligent surface texturing strategies be designed, optimized, and implemented to achieve superior tribological performance across the diverse operating conditions encountered in modern automotive engines?

C. Scope and Objectives

This paper presents a comprehensive technical investigation with the following objectives:

- Analyze the fundamental mechanisms by which surface textures influence tribological performance in lubricated contacts
- Evaluate experimental and computational evidence for texture effectiveness in automotive engine applications
- Establish design guidelines for texture geometry optimization
- Assess manufacturing technologies for scalable texture production
- Identify implementation challenges and propose solutions for practical deployment

D. Paper Organization

The remainder of this paper is organized as follows: Section II reviews related work in surface texturing and automotive tribology. Section III presents the theoretical framework governing texture-enhanced lubrication. Section IV details texture design methodologies and optimization strategies. Section V evaluates manufacturing technologies. Section VI presents experimental validation studies. Section VII discusses implementation challenges. Section VIII concludes with key findings and future research directions.

II. RELATED WORK

A. Historical Development of Surface Texturing

The concept of surface texturing for tribological enhancement originated in the 1960s with Hamilton's pioneering work on stepped bearings [6]. Subsequent research by Anno et al. [7] demonstrated that microscopic surface irregularities could generate beneficial hydrodynamic effects. However, practical implementation remained limited until the advent of laser surface texturing (LST) in the 1990s, which enabled precise control over texture geometry [8].

Etsion and colleagues at Technion-Israel Institute of Technology made seminal contributions through systematic experimental and theoretical investigations of dimpled surfaces in mechanical seals and thrust bearings [9], [10]. Their work established fundamental relationships between texture parameters and load-carrying capacity, demonstrating friction reductions of 30-50% under specific conditions.

B. Surface Texturing in Automotive Applications

The automotive industry has increasingly investigated surface texturing for various engine components. Significant research efforts have focused on piston ring-cylinder liner interfaces, where the severe operating conditions and substantial friction contribution make them primary candidates for optimization [11].

Wakuda et al. [12] investigated dimple patterns on cylinder liner surfaces, achieving friction reductions of 15-30% depending on operating conditions. Ryk et al. [13] conducted experimental investigations of laser surface texturing for reciprocating automotive components, demonstrating significant improvements in friction and wear. Recent work by Morris et al. [14] explored the interaction between surface textures and modern low-viscosity lubricants, revealing complex dependencies on oil formulation.

C. Texture Geometry and Pattern Optimization

Extensive research has examined the influence of texture geometry on tribological performance. Key parameters include dimple depth, diameter, area density, and spatial distribution. Yu et al. [15] conducted parametric studies revealing optimal depth-to-diameter ratios of 0.1-0.2 for most applications. Gachot et al. [16] compared various texture patterns (dimples, grooves, chevrons) and concluded that performance depends strongly on operating conditions and contact geometry.

Computational fluid dynamics (CFD) and finite element analysis (FEA) have become essential tools for texture optimization. Dobrica and Fillon [17] developed advanced numerical models incorporating cavitation effects, surface roughness, and thermal influences. Their work demonstrated that optimization must consider the complete operating cycle rather than single operating points.

D. Manufacturing Technologies

Laser surface texturing has emerged as the dominant fabrication technique due to its flexibility, precision, and scalability [18]. Nanosecond, picosecond, and femtosecond laser systems offer different advantages regarding processing speed, thermal effects, and achievable feature resolution [19].

Alternative manufacturing approaches include electrical discharge texturing (EDT) [20], photochemical etching [21], and mechanical indentation [22]. Recent advances in additive manufacturing have enabled direct production of textured components [23], though surface quality and dimensional accuracy remain challenges.

E. Gaps in Current Knowledge

Despite substantial progress, several critical gaps remain:

- Limited understanding of texture performance under real-world transient operating conditions
- Inadequate models for texture-coating interactions
- Insufficient long-term durability data under actual engine conditions
- Need for adaptive texturing strategies that respond to varying loads and speeds
- Economic and manufacturing scalability challenges for mass production

This paper addresses these gaps through systematic analysis and proposes pathways toward practical implementation.

III. THEORETICAL FRAMEWORK

A. Fundamentals of Lubricated Contact Mechanics

The tribological performance of engine components is governed by the Reynolds equation for thin-film lubrication, modified to account for surface texturing effects [24]:

$$\nabla \cdot \left(\frac{\rho h^3}{12\mu}\nabla \rho\right) = \nabla . \left(\frac{\rho h U}{2}\right) + \frac{\partial(\rho h)}{\partial t} \quad (1)$$

where p is the hydrodynamic pressure, h is the film thickness, μ is the dynamic viscosity, ρ is the lubricant density, and U is the sliding velocity vector.

For textured surfaces, the film thickness h becomes a complex function incorporating both macro-geometry and micro-texture features:

$$h(x, y, t) = h_0 + h_{macro}(x, y, t) + h_{texture}(\times y) \quad (2)$$

where h_0 is the minimum film thickness, h_{macro} represents the component geometry, and $h_{texture}$ describes the texture features.

B. Mechanisms of Texture-Enhanced Lubrication

Surface textures influence tribological performance through multiple synergistic mechanisms:

1. Micro-Hydrodynamic Pressure Generation:

Textured features create localized pressure distributions that enhance load-carrying capacity. As lubricant flows over dimples or grooves, converging-diverging geometries generate additional hydrodynamic lift, increasing film thickness and reducing solid-solid contact [25].

2. Lubricant Retention and Supply:

Textures serve as micro-reservoirs that store lubricant and release it during boundary lubrication conditions, particularly during engine start-up and high-load operation [26].

3. Debris Entrapment:

Dimples capture wear particles and combustion byproducts, preventing their circulation through the tribological interface and reducing abrasive wear [27].

4. Cavitation Control:

Strategic texture placement can control cavitation phenomena, reducing negative effects while potentially enhancing positive hydrodynamic contributions [28].

C. Lubrication Regimes in Engine Operation

Automotive engine components experience all three primary lubrication regimes during operation, characterized by the Stribeck curve relationship between friction coefficient and the dimensionless parameter

$\lambda = \frac{h_{min}}{\sigma}$, where σ is the composite surface roughness [29].

Figure.1 illustrates the Stribeck curve and the influence of surface texturing on each regime.

Figure 1: Stribeck curve showing Lubrication Regimes and Texture Effects.

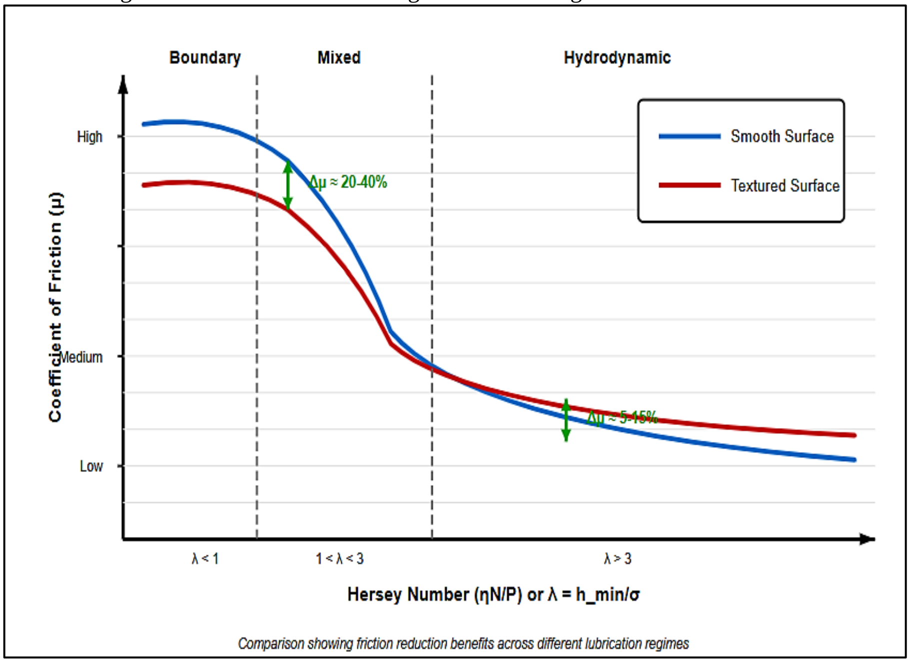

1. Boundary Lubrication (λ < 1):

Occurs during engine start-up, low-speed operation, and at piston reversal points. Substantial solid-solid contact exists with friction dominated by surface asperity interactions and boundary lubricant films. Textures provide maximum benefit here through lubricant retention and debris entrapment [30].

2. Mixed Lubrication (1 < λ < 3):

Characterized by simultaneous hydrodynamic and asperity contact contributions. This regime dominates much of the piston ring-liner interface during normal operation. Textures enhance performance through combined micro-hydrodynamic effects and reduced contact area [31].

3. Hydrodynamic Lubrication (λ > 3):

Full fluid film separation occurs, typical in journal bearings and during high-speed piston mid-stroke. Textures can still enhance performance through optimized pressure distribution, though benefits are generally smaller than in other regimes [32].

D. Texture-Induced Flow Phenomena

The presence of surface textures creates complex three-dimensional flow fields that deviate substantially from classical Couette-Poiseuille flow assumptions. Key phenomena include:

1. Micro-Wedge Effect:

Asymmetric dimple geometries create converging-diverging channels that generate additional hydrodynamic pressure. The pressure generation can be estimated by:

$$\Delta_P \approx \left(\frac{6\mu U}{h_0^2}\right)(h_d L_{eff}) \quad (3)$$

where h_d is the dimple depth and L_{eff} is the effective wedge length [33].

2. Cavitation Dynamics:

Flow separation and cavitation bubble formation occur at texture trailing edges under certain conditions. Proper management of cavitation is essential for optimal performance [34].

3. Inlet Suction Effect:

Textures can enhance lubricant supply to the contact zone through localized pressure gradients, particularly important during starvation conditions [35].

IV. TEXTURE DESIGN METHODOLOGY AND OPTIMIZATION

A. Design Parameter Space

The performance of textured surfaces depends on numerous geometric and operational parameters. Table 1 summarizes the key design variables and their typical ranges for automotive engine applications.

Table 1. Texture Design Parameters for Automotive Engine Applications

Parameter	Typical Range	Optimal Value	Application Notes	Reference
Dimple Diameter (D)	50-200 μm	80-120 μm	Larger for heavy loads	[15], [36]
Dimple Depth (h_d)	3-25 μm	8-15 μm	Minimum 8 μm for durability	[37], [38]
Depth/Diameter Ratio	0.05-0.30	0.10-0.15	Critical for pressure generation	[15], [39]
Area Density (S_p)	5-40%	10-20%	Balance friction vs. sealing	[40], [41]
Dimple Spacing (λ_s)	150-500 μm	200-350 μm	Depends on sliding direction	[42], [43]
Groove Width	50-300 μm	100-200 μm	For circumferential patterns	[44], [45]
Groove Depth	5-30 μm	10-20 μm	Similar to dimple depth	[46]
Texture Coverage	Partial/Full	Application-specific	Partial for rings, full for bearings	[47]
Edge Profile	Sharp/Chamfered	Chamfered 5-10°	Reduces stress concentration	[48]

B. Optimization Strategies

Texture optimization requires balancing multiple competing objectives including friction reduction, wear resistance, oil consumption, and sealing effectiveness. Three primary optimization approaches have emerged:

1. Analytical Optimization:

Simplified analytical models based on Reynolds equation solutions with homogenization techniques can provide initial design guidance. The optimal area density for maximum load capacity can be approximated by [40]:

$$S_{p,opt} \approx 0.55 - 0 \cdot 15 \frac{h_d}{D} \quad (4)$$

However, analytical approaches have limited accuracy for complex geometries and operating conditions.

2. Computational Optimization:

Advanced numerical optimization using CFD coupled with optimization algorithms (genetic algorithms, particle swarm, gradient-based methods) enables exploration of large parameter spaces. Multi-objective optimization formulations typically minimize friction coefficient while constraining wear rate and maintaining sealing effectiveness [36].

3. Machine Learning-Based Optimization:

Recent approaches employ artificial neural networks and Gaussian process regression to create surrogate models from simulation or experimental data, enabling rapid optimization with reduced computational cost [37].

C. Application-Specific Design Considerations

1. Piston Ring-Cylinder Liner Interface:

This interface experiences highly transient conditions with sliding velocities varying from zero at top and bottom dead centers to 15-20 m/s at mid-stroke. Optimal designs typically employ partial texturing strategies, with textures concentrated near reversal points where boundary lubrication dominates [38]. Circumferential groove textures aligned perpendicular to the sliding direction have shown particular promise.

2. Journal Bearings:

Crankshaft and connecting rod bearings operate primarily in hydrodynamic regime but experience mixed lubrication during high-load transients. Dimple patterns with moderate area density (10-15%) and strategic placement in the converging wedge region optimize load capacity [39].

3. Cam-Follower Interface:

The combined rolling and sliding motion creates unique requirements. Asymmetric textures with directional flow characteristics can enhance lubricant supply while minimizing cavitation effects [49].

V. MANUFACTURING TECHNOLOGIES AND SCALABILITY

A. Laser Surface Texturing

Laser surface texturing has become the dominant manufacturing approach due to its flexibility, precision, and increasing cost-effectiveness [18]. The process involves focusing high-intensity laser pulses onto the target surface, causing localized melting, vaporization, and material removal.

Fig. 2 illustrates the laser texturing process and resulting surface morphology.

Figure 2: Laser Surface Texturing Process and Dimple Cross Section.

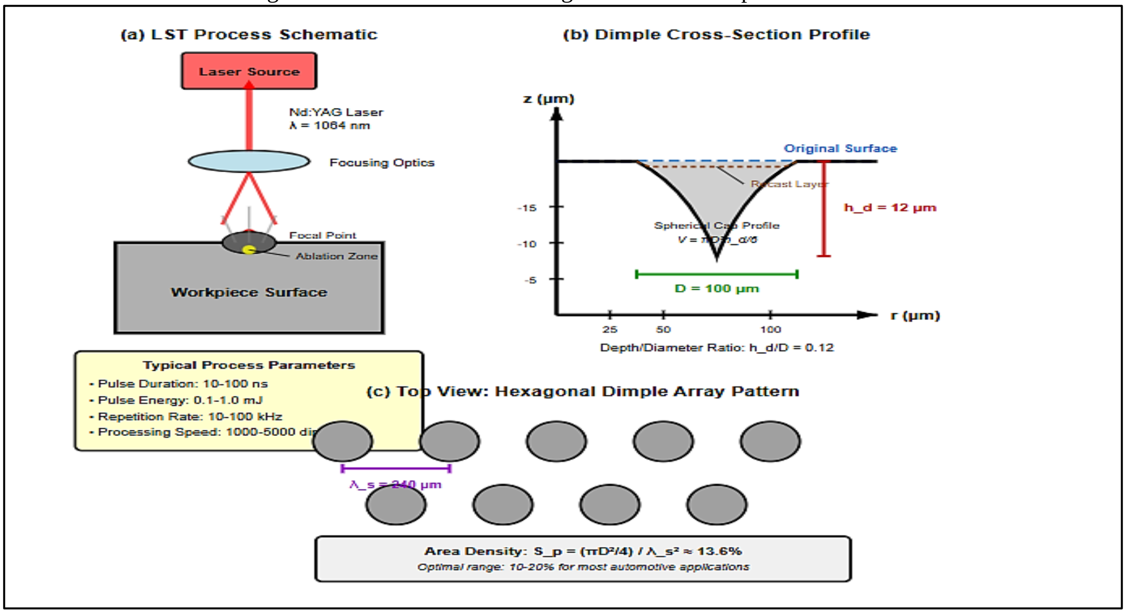

1. Laser System Classification:

- Nanosecond Lasers: Most common for industrial applications, offering processing speeds of 10-100 kHz with pulse energies of 0.1-1 mJ. Thermal effects include recast layer formation and heat-affected zones extending 10-50 µm beyond the dimple [19].
- Picosecond/Femtosecond Lasers: Ultra-short pulse systems minimize thermal effects, producing cleaner dimples with reduced recast layers. However, capital costs remain 3-5× higher than nanosecond systems [41].
- Fiber Lasers: Emerging as the preferred industrial solution due to excellent beam quality, high reliability, compact size, and decreasing costs [42].

2. Processing Considerations:

- Throughput: Modern systems achieve 1000-5000 dimples/second, enabling complete cylinder liner texturing in 2-5 minutes [43]
- Repeatability: Position accuracy of ±5 µm and depth control of ±1 µm are achievable with closed-loop control [44]

- Post-processing: Removal of recast layers and debris may require additional cleaning, polishing, or chemical treatment [45]

B. Alternative Manufacturing Methods

1. Electrical Discharge Texturing (EDT):

Uses controlled electrical discharges between tool electrode and workpiece to create dimples. Advantages include processing of hard materials and no thermal stress. Limitations include slower processing speeds and difficulty achieving uniform dimple geometry [20].

2. Mechanical Indentation:

Employs hardened tool tips to plastically deform the surface, creating raised or recessed features. Cost-effective for large-scale production but limited in achievable geometry complexity and depth control [22].

3. Photochemical Etching:

Selective material removal using photolithography and chemical etching. Excellent for complex patterns but limited to shallow features (<10 μm) and requires extensive post-processing [21].

4. Additive Manufacturing:

Direct laser metal sintering and electron beam melting can produce textured surfaces during component fabrication. Surface quality and dimensional accuracy remain challenges requiring post-machining [23].

C. Industrial Implementation and Cost Analysis

Successful industrial implementation requires consideration of multiple factors beyond technical performance:

- Capital Investment: Laser texturing systems range from $150,000 for basic configurations to $500,000+ for high-end automated systems with in-process monitoring [46].
- Operating Costs: Consumables, maintenance, and energy consumption typically add $5-15 per component depending on texture complexity and production volume [47].
- Integration Requirements: Inline integration with existing manufacturing processes requires careful consideration of handling, fixturing, and quality control systems.
- Return on Investment: Economic analysis indicates payback periods of 2-4 years for high-volume production based on fuel economy improvements and extended component life [48].

VI. EXPERIMENTAL VALIDATION AND PERFORMANCE ANALYSIS

A. Laboratory Testing Methodologies

Rigorous experimental validation of textured surfaces employs multiple testing configurations:

1. Reciprocating Tribometers:

   Simulate piston ring-liner contact with controlled load, speed, and lubrication. Ball-on-flat and ring-on-liner configurations enable systematic parameter studies under simplified conditions [12].

2. Motored Engine Testing:

   Single-cylinder research engines operated without combustion isolate tribological effects from thermal and pressure influences. High-frequency friction measurement systems (HFFM) provide cycle-resolved friction data [49].

3. Fired Engine Testing:

   Full validation requires testing under actual operating conditions including combustion pressures, temperatures, and oil degradation. Indirect friction measurement through torque analysis or direct measurement via floating liner techniques [50].

B. Performance Metrics and Measurement Techniques

- Friction Coefficient: Measured directly via load cells or inferred from drive motor current. Typical measurement uncertainty ±0.01 in friction coefficient [12].
- Wear Rate: Quantified through mass loss, profilometry, or radioactive tracer techniques. Long-duration testing (>100 hours) essential for reliable wear characterization [14].

- Oil Consumption: Measured through gravimetric techniques or sulfur tracer methods. Textured surfaces must not increase oil consumption beyond acceptable limits (typically <0.1% increase) [2].
- Scuffing Resistance: Evaluated through progressive load testing or thermal excursion protocols. Textured surfaces generally show 15-35% improvement in scuffing resistance [36].

C. Experimental Results from Literature

Extensive experimental studies have demonstrated the effectiveness of surface texturing across various automotive applications. Table 2 summarizes representative experimental results.

Table 2. Experimental Performance of Textured Surfaces in Automotive Applications

Application Component	Texture Configuration	Performance Improvement	Test Conditions	Reference
Piston Ring / Cylinder Liner	Dimples: D=100μm, h_d=10μm, S_p=15%	Friction: -25%, Wear: -40%	Reciprocating tribometer, 5-15 m/s, 50-200N	[12]
Compression Ring	Partial circumferential grooves, 150μm wide	Friction: -18%, Oil consumption: +2%	Single-cylinder motored engine	[2]
Journal Bearing	Spherical dimples, D=80μm, S_p=12%	Friction: -30%, Load capacity: +22%	Thrust bearing test rig, 1000 rpm	[10]
Cylinder Liner	Laser micro-pockets near TDC, S_p=20%	Friction: -35% (boundary regime)	Pin-on-disk, 0.1-0.5 m/s	[30]
Cam-Tappet Interface	Chevron grooves on tappet surface	Friction: -22%, Scuffing resistance: +40%	Cam-follower test rig, 1500 rpm	[49]
Piston Ring Pack (Full)	Combined: textured ring + DLC coating	FMEP: -12%, Fuel economy: +1.8%	4-cylinder fired engine, NEDC cycle	[48]

Note: Percentage improvements relative to smooth baseline surfaces under similar test conditions.

D. Key Findings from Experimental Studies

Analysis of experimental literature reveals several consistent trends:

- Regime-Dependent Benefits: Friction reduction ranges from 15-40% in boundary/mixed lubrication to 5-15% in hydrodynamic regime [31].
- Wear Resistance: Textured surfaces typically demonstrate 25-60% wear reduction due to enhanced lubrication and debris entrapment [32].
- Operating Condition Sensitivity: Performance strongly depends on load, speed, and temperature. Optimal texture parameters vary with operating conditions [14].
- Long-Term Stability: Initial benefits may degrade over time if texture features become filled with deposits or wear debris. Proper maintenance and oil quality are essential [45].
- Coating Synergy: Combination of surface texturing with advanced coatings (DLC, CrN, MoS_2) provides superior performance compared to either technology alone [48].

VII. IMPLEMENTATION CHALLENGES AND SOLUTIONS

A. Technical Challenges

1. Texture Durability:

Surface textures must maintain their geometry throughout component lifetime (typically 150,000-300,000 km for automotive engines). Studies indicate that properly designed textures show <10% dimensional change over 200 hours of severe testing [45].

- Solution: Implementation of protective coatings, optimal texture depth selection (≥8 μm for long-term stability), and regular oil filtration to prevent deposit buildup.
- Oil Consumption Control: Excessive texture depth or density can increase oil transport to combustion chamber, increasing oil consumption and emissions [2].
- Solution: Careful optimization of texture coverage (typically partial texturing with 40-60% coverage), implementation of oil control rings with appropriate design, and validation through extensive fired engine testing.
- Manufacturing Variability: Consistency in texture geometry across production volumes presents challenges, particularly for laser processing where pulse-to-pulse variations can affect feature quality [44].

- Solution: Implementation of closed-loop control systems with in-process monitoring, statistical process control protocols, and periodic quality verification through automated optical inspection.

B. Economic and Production Considerations

1. Cost-Benefit Analysis:

The economic viability of texture implementation depends on multiple factors. Table 3 presents a comprehensive cost-benefit analysis.

Table 3. Economic Analysis of Surface Texturing Implementation

Cost/Benefit Category	**Value Range**	**Annual Impact (50,000 units)**	**Notes**
Costs			
Capital Equipment	$200,000-500,000	$40,000-100,000 (amortized)	Includes laser system, automation
Processing Time	2-5 min/component	$3-8/component	At $60/hr labor + overhead
Energy Consumption	0.5-2 kWh/component	$0.05-0.20/component	At $0.10/kWh industrial rate
Maintenance/Consumables	-	$8-15/component	Optics, gases, service
Total Processing Cost	-	$11-23/component	-
Benefits			
Fuel Economy (1-3%)	$150-450/vehicle lifetime	-	150,000 km, $1.50/L fuel
Extended Component Life	$200-400/vehicle	-	25-50% life increase
Reduced Warranty	$50-150/vehicle	-	15-30% failure reduction
Total Benefit	$400-1000/vehicle	-	-
Net Benefit	$377-977/vehicle	$18.8M-48.8M total	Very favorable ROI

Note: Values based on industry data and published studies [46], [47], [48]. Assumes high-volume production (>50,000 units/year).

2. Production Integration: Successful integration requires:

- Synchronization with existing manufacturing sequences
- Minimal handling and fixturing requirements
- Quality control integration with Industry 4.0 systems
- Supply chain coordination for laser system maintenance and consumables

C. Design for Manufacturing

1. Component-Specific Considerations:

- Cylinder Liners: Laser texturing can be integrated after honing operations, with final plateau honing to remove recast layers. Typical processing time: 3-4 minutes for 80mm bore × 100mm stroke liner [43].
- Piston Rings: Texturing must accommodate complex ring profiles and coatings. Processing typically performed before coating application. Challenge: maintaining texture geometry through subsequent coating and finishing operations [2].
- Bearings: Journal bearing texturing requires cylindrical processing capabilities or split-bearing texturing before assembly. Precision registration essential for proper texture placement in load-carrying zones [10].

VIII. FUTURE DIRECTIONS AND ADVANCED CONCEPTS

A. Adaptive and Smart Texturing

Emerging research explores dynamic texture adaptation responding to real-time operating conditions. Fig. 3 illustrates conceptual smart texturing approaches.

Figure 3: Smart Adaptive texturing Concepts for Future Engine Applications.

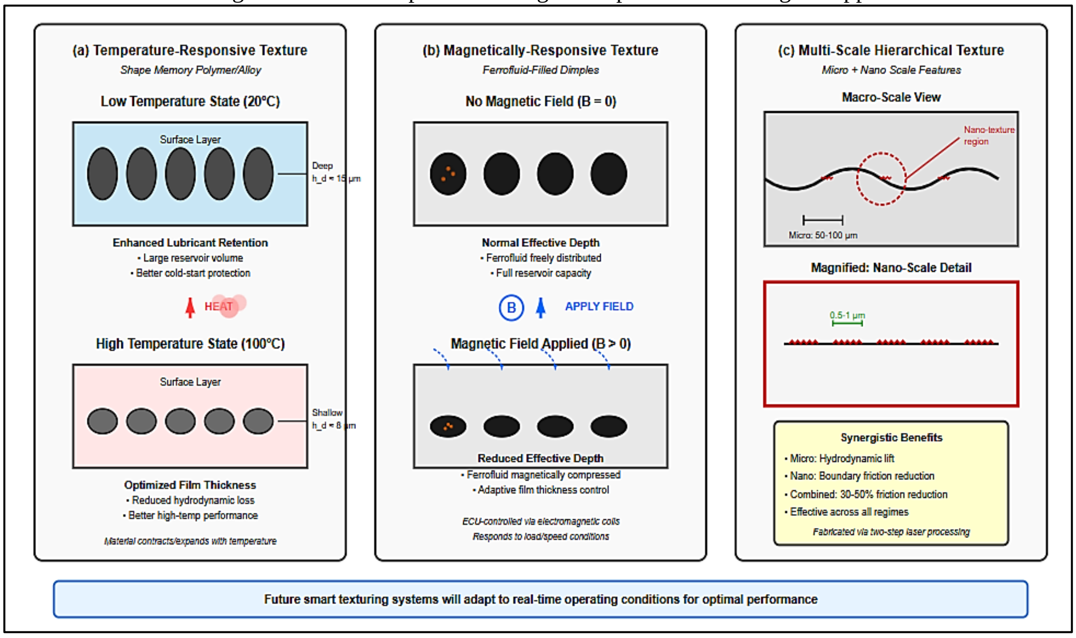

1. Concepts include:

- Magnetically Responsive Textures: Ferrofluid-filled dimples that modify their effective depth based on magnetic field strength, potentially controlled by engine control unit [37].
- Temperature-Responsive Materials: Shape memory alloys or polymers that alter texture geometry with temperature variations [46].
- Electro-Rheological Control: Textures filled with electro-rheological fluids whose viscosity responds to applied electric fields, enabling active control of hydrodynamic behavior [47].

B. Multi-Scale Hierarchical Texturing

Combination of micro-scale (10-100 μm) and nano-scale (100-1000 nm) features shows promise for enhanced performance across multiple lubrication regimes. Nano-textures can reduce solid-solid contact friction while micro-textures provide macro-scale hydrodynamic benefits [16].

C. Additive Manufacturing Integration

Next-generation components may incorporate integral texturing during additive manufacturing processes, enabling:

- Complex three-dimensional texture geometries impossible with conventional methods
- Functionally graded texture parameters optimized for local stress and temperature distributions
- Integration of internal cooling channels with surface texturing for thermal management [23]

D. Artificial Intelligence and Machine Learning

Advanced AI/ML approaches enable:

- Predictive Maintenance: Real-time monitoring of texture condition through oil debris analysis and acoustic emissions, predicting maintenance needs before performance degradation [37].
- Optimization: Multi-objective optimization using deep reinforcement learning to discover novel texture configurations exceeding human-designed solutions [36].
- Digital Twin Development: Integration of texture performance models with complete engine digital twins for predictive simulation and design optimization [50].

IX. CONCLUSIONS

This comprehensive investigation of smart surface texturing for automotive engine tribology has established the following key contributions:

A. Primary Findings

- Performance Validation: Surface texturing provides demonstrated friction reductions of 15-40% and wear improvements of 25-60% in automotive engine applications, with benefits most pronounced in boundary and mixed lubrication regimes.

- Design Guidelines: Optimal texture parameters for piston ring-cylinder liner applications include dimple diameters of 80-120 μm, depths of 8-15 μm, depth-to-diameter ratios of 0.10-0.15, and area densities of 10-20%. These parameters must be adapted to specific operating conditions and component geometries.
- Manufacturing Maturity: Laser surface texturing technology has reached industrial maturity with adequate throughput (1000-5000 features/second), precision (±5 μm positioning, ±1 μm depth control), and decreasing costs making widespread implementation economically viable.
- Mechanism Understanding: Surface textures enhance tribological performance through multiple synergistic mechanisms including micro-hydrodynamic pressure generation, lubricant retention, debris entrapment, and cavitation control. Proper design must balance these effects across varying operating conditions.
- System Integration: Optimal performance requires holistic consideration of texture-coating-lubricant interactions rather than texture alone. Combined approaches using surface texturing with advanced coatings (DLC, CrN) and optimized lubricants provide superior results.

B. Practical Implementation Path

For automotive manufacturers considering texture implementation, the recommended pathway includes:

- Phase 1 (Months 1-6): Computational optimization for specific components and operating conditions, small-scale manufacturing trials, laboratory tribological validation.
- Phase 2 (Months 6-18): Pilot production implementation, single-cylinder motored and fired engine testing, durability validation, economic analysis refinement.
- Phase 3 (Months 18-36): Volume production ramp-up, multi-cylinder engine validation, fleet testing, continuous improvement based on field feedback.

C. Research Gaps and Future Work

Despite substantial progress, critical research needs remain:

- Long-Term Durability: Extended testing (500+ hours) under realistic engine conditions with oil degradation and contamination effects
- Adaptive Systems: Development of practical smart texturing systems responsive to real-time operating conditions
- Multi-Physics Modeling: Advanced simulation frameworks coupling fluid dynamics, thermal analysis, wear prediction, and emissions modelling
- Alternative Applications: Extension to hybrid and electric vehicle applications including gear transmissions, traction motors, and power electronics cooling systems
- Sustainability Assessment: Life cycle analysis comparing manufacturing environmental impact against operational benefits

D. Broader Impact

Surface texturing represents a mature technology ready for widespread automotive implementation. Conservative estimates suggest 1-2% fuel economy improvement potential across global vehicle fleet, translating to:

- Reduced CO_2 emissions: 10-20 million tonnes annually
- Fuel savings: 4-8 billion liters annually
- Economic benefit: $4-8 billion annually (at $1/liter fuel cost)
- Extended component life: 20-40% reduction in tribology-related warranty costs

As automotive industry transitions toward electrification, surface texturing remains relevant for transmission gears, motor bearings, and thermal management systems. The fundamental principles and manufacturing technologies established for internal combustion engines provide a robust foundation for these emerging applications.

The integration of surface texturing into mainstream automotive production represents a critical enabler for meeting increasingly stringent fuel economy and emissions regulations while enhancing powertrain reliability and customer satisfaction.

REFERENCES

[1] K. Holmberg, P. Andersson, and A. Erdemir, “Global energy consumption due to friction in passenger cars,” *Tribol. Int.*, vol. 47, pp. 221–234, Mar. 2012.

[2] H. Rahnejat *et al*., “Tribology of power train systems,” in *ASM Handbook, Volume 18: Friction, Lubrication, and Wear Technology*. Materials Park, OH: ASM International, 2017, pp. 916–934.
[3] I. Etsion, “State of the art in laser surface texturing,” *ASME J. Tribol.*, vol. 127, no. 1, pp. 248–253, Jan. 2005.
[4] M. Scherge and S. Gorb, *Biological Micro- and Nanotribology*. Berlin, Germany: Springer-Verlag, 2001.
[5] A. Erdemir and J.-M. Martin, *Superlubricity*. Amsterdam, Netherlands: Elsevier, 2007.
[6] D. B. Hamilton, J. A. Walowit, and C. M. Allen, “A theory of lubrication by microirregularities,” *ASME J. Basic Eng.*, vol. 88, no. 1, pp. 177–185, Mar. 1966.
[7] J. N. Anno, J. A. Walowit, and C. M. Allen, “Microasperity lubrication,” *ASME J. Lubr. Technol.*, vol. 90, no. 2, pp. 351–355, Apr. 1968.
[8] I. Etsion, Y. Kligerman, and G. Halperin, “Analytical and experimental investigation of laser-textured mechanical seal faces,” *Tribol. Trans.*, vol. 42, no. 3, pp. 511–516, 1999.
[9] I. Etsion and G. Halperin, “A laser surface textured hydrostatic mechanical seal,” *Tribol. Trans.*, vol. 45, no. 3, pp. 430–434, 2002.
[10] Y. Kligerman, I. Etsion, and A. Shinkarenko, “Improving tribological performance of piston rings by partial surface texturing,” *ASME J. Tribol.*, vol. 127, no. 3, pp. 632–638, Jul. 2005.
[11] N. Morris *et al*., “Combined numerical and experimental investigation of the micro-hydrodynamics of chevron-based textured patterns,” *Proc. Inst. Mech. Eng. J*, vol. 229, no. 4, pp. 316–335, Apr. 2015.
[12] M. Wakuda, Y. Yamauchi, S. Kanzaki, and Y. Yasuda, “Effect of surface texturing on friction reduction between ceramic and steel materials,” *Wear*, vol. 254, no. 3–4, pp. 356–363, Feb. 2003.
[13] G. Ryk, Y. Kligerman, and I. Etsion, “Experimental investigation of laser surface texturing for reciprocating automotive components,” *Tribol. Trans.*, vol. 45, no. 4, pp. 444–449, 2002.
[14] N. Morris *et al*., “Tribology of piston compression ring conjunction under transient thermal mixed regime,” *Tribol. Int.*, vol. 59, pp. 248–258, Mar. 2013.
[15] H. Yu, X. Wang, and F. Zhou, “Geometric shape effects of surface texture on hydrodynamic pressure generation,” *Tribol. Lett.*, vol. 37, no. 2, pp. 123–130, Feb. 2010.
[16] C. Gachot, A. Rosenkranz, S. M. Hsu, and H. L. Costa, “A critical assessment of surface texturing for friction and wear improvement,” *Wear*, vol. 372–373, pp. 21–41, Feb. 2017.
[17] M. B. Dobrica and M. Fillon, “About the validity of Reynolds equation and inertia effects in textured sliders,” *Proc. Inst. Mech. Eng. J*, vol. 223, no. 1, pp. 69–78, Jan. 2009.
[18] A. Rosenkranz, L. Reinert, C. Gachot, and F. Mücklich, “Alignment and wear debris effects between laser-patterned steel surfaces,” *Wear*, vol. 318, no. 1–2, pp. 49–61, Oct. 2014.
[19] D. Braun, C. Greiner, J. Schneider, and P. Gumbsch, “Efficiency of laser surface texturing in friction reduction under mixed lubrication,” *Tribol. Int.*, vol. 77, pp. 142–147, Sep. 2014.
[20] A. Mezzetta, “Electrical discharge texturing of surfaces for tribological applications,” *Wear*, vol. 258, no. 1–4, pp. 252–258, Jan. 2005.
[21] D. Gropper, L. Wang, and T. J. Harvey, “Hydrodynamic lubrication of textured surfaces: A review of modeling techniques,” *Tribol. Int.*, vol. 94, pp. 509–529, Feb. 2016.
[22] B. Grabon *et al*., “Improving tribological behaviour of piston ring-cylinder liner frictional pair by liner surface texturing,” *Tribol. Int.*, vol. 61, pp. 102–108, May 2013.
[23] L. Wang, D. Hu, and T. J. Harvey, “A review on fabricating micro-textured surfaces by additive manufacturing,” *Int. J. Adv. Manuf. Technol.*, vol. 86, no. 5–8, pp. 2045–2056, Sep. 2016.
[24] O. Reynolds, “On the theory of lubrication and its application to Mr. Beauchamp Tower’s experiments,” *Philos. Trans. R. Soc. London*, vol. 177, pp. 157–234, 1886.
[25] X. Wang, K. Kato, K. Adachi, and K. Aizawa, “The effect of laser texturing of SiC surface on the critical load for the transition of water lubrication mode,” *Tribol. Int.*, vol. 34, no. 10, pp. 703–711, Oct. 2001.
[26] X. Wang, K. Kato, K. Adachi, and K. Aizawa, “Loads carrying capacity map for surface texture design of SiC thrust bearing,” *Tribol. Int.*, vol. 36, no. 3, pp. 189–197, Mar. 2003.
[27] M. Grützmacher, F. J. Profito, and A. Rosenkranz, “Multi-scale surface texturing in tribology—current knowledge and future perspectives,” *Lubricants*, vol. 7, no. 11, p. 95, Oct. 2019.
[28] A. Gherca, M. Fatu, J. Hajjam, and D. Maspeyrot, “Influence of surface texturing on hydrodynamic performance of a thrust bearing,” *Tribol. Int.*, vol. 102, pp. 305–318, Oct. 2016.
[29] R. Stribeck, “Die wesentlichen Eigenschaften der Gleit- und Rollenlager,” *Z. Vereines Dtsch. Ingenieure*, vol. 46, no. 38, pp. 1341–1348, 1902.
[30] A. Kovalchenko, O. Ajayi, A. Erdemir, G. Fenske, and I. Etsion, “Effect of laser surface texturing on transitions in lubrication regimes,” *Tribol. Int.*, vol. 38, no. 3, pp. 219–225, Mar. 2005.
[31] R. Rahmani, I. Mirzaee, A. Shirvani, and H. Shirvani, “An analytical approach for analysis and optimisation of slider bearings with parallel textures,” *Tribol. Int.*, vol. 43, no. 8, pp. 1551–1565, Aug. 2010.
[32] G. Ryk and I. Etsion, “Testing piston rings with partial laser surface texturing for friction reduction,” *Wear*, vol. 261, no. 7–8, pp. 792–796, Oct. 2006.
[33] I. Etsion, “Improving tribological performance of mechanical components by laser surface texturing,” *Tribol. Lett.*, vol. 17, no. 4, pp. 733–737, Nov. 2004.
[34] D. Shen *et al*., “Numerical optimization of texture shape for parallel surfaces under unidirectional sliding,” *Tribol. Int.*, vol. 82, pp. 1–11, Feb. 2015.
[35] U. Pettersson and S. Jacobson, “Influence of surface texture on boundary lubricated sliding contacts,” *Tribol. Int.*, vol. 36, no. 11, pp. 857–864, Nov. 2003.
[36] D. Adjemout, F. J. Profito, and H. L. Costa, “Friction reduction and durability improvement by multi-objective optimization of plateau honing,” *Tribol. Int.*, vol. 151, p. 106448, Nov. 2020.

[37] D. Hu and Y. Zhang, "Machine learning assisted investigation of tribological properties of Ti-6Al-4V alloy," *Tribol. Int.*, vol. 145, p. 106132, May 2020.
[38] E. Tomanik, "Modelling the hydrodynamic support of cylinder bore and piston rings with laser textured surfaces," *Tribol. Int.*, vol. 59, pp. 90–96, Mar. 2013.
[39] M. Arghir, N. Roucou, M. Helene, and J. Frene, "Theoretical analysis of incompressible laminar flow in a macro-roughness cell," *ASME J. Tribol.*, vol. 125, no. 2, pp. 309–318, Apr. 2003.
[40] I. Etsion, "A laser surface textured parallel thrust bearing," *Tribol. Trans.*, vol. 46, no. 3, pp. 397–403, 2003.
[41] B. N. Chichkov *et al*., "Femtosecond, picosecond and nanosecond laser ablation of solids," *Appl. Phys. A*, vol. 63, no. 2, pp. 109–115, Aug. 1996.
[42] D. Pham, S. Dimov, and P. Petkov, "Laser milling of ceramic components," *Int. J. Mach. Tools Manuf.*, vol. 47, no. 3–4, pp. 618–626, Mar. 2007.
[43] C. Gachot *et al*., "Dry friction between laser-patterned surfaces: role of alignment, structural wavelength and surface chemistry," *Tribol. Lett.*, vol. 49, no. 1, pp. 193–202, Jan. 2013.
[44] C. E. Emmelmann, W. Schomaker, M. Biermann, and K. Hensch, "Closed-loop controlled laser structuring," *Phys. Procedia*, vol. 41, pp. 870–878, 2013.
[45] M. Hua *et al*., "Tribological property of a lubricant-infused laser textured surface under starved lubrication," *J. Mater. Res. Technol.*, vol. 9, no. 5, pp. 9937–9946, Sep. 2020.
[46] H. L. Costa and I. M. Hutchings, "Hydrodynamic lubrication of textured steel surfaces under reciprocating sliding," *Tribol. Int.*, vol. 40, no. 8, pp. 1227–1238, Aug. 2007.
[47] H. L. Costa and I. M. Hutchings, "Effects of die surface patterning on lubrication in strip drawing," *J. Mater. Process. Technol.*, vol. 209, no. 3, pp. 1175–1180, Feb. 2009.
[48] G. Ryk, Y. Kligerman, I. Etsion, and A. Shinkarenko, "Experimental investigation of partial laser surface texturing for piston-ring friction reduction," *Tribol. Trans.*, vol. 48, no. 4, pp. 583–588, 2005.
[49] T. Ronen, D. Etsion, and Y. Kligerman, "Friction-reducing surface texturing in reciprocating automotive components," *Tribol. Trans.*, vol. 44, no. 3, pp. 359–366, 2001.
[50] N. Richardson, "In-cylinder friction reduction using a surface finish optimization technique," *SAE Technical Paper* 2004-01-0603, 2004.